High-resolution X-ray imaging of catalytic reactions by using X-ray Absorption Spectroscopy

Dissertation
zur Erlangung des Doktorgrades
an der Fakultät für Mathematik, Informatik und Naturwissenschaften
Fachbereich Physik
der Universität Hamburg

Vorgelegt von

Saba Alizadehfanaloo

Hamburg

2024

Gutachter der Dissertation: Prof. Dr. Christian G. Schroer
Dr. habil. Thomas Sheppard

Zusammensetzung der Prüfungskommission:
1. Prof. Dr. Daniela Pfannkuche
2. Prof. Dr. Dorota Koziej
3. Dr. habil. Thomas Keller
4. Dr. habil. Thomas Sheppard
5. Prof. Dr. Christian G. Schroer

Vorsitzende der Prüfungskommission: Prof. Dr. Daniela Pfannkuche

Datum der Disputation: 24.06.2024

Vorsitzender des Fach-Promotionsausschusses Physik: Prof. Dr. Markus Drescher
Leiter des Fachbereichs Physik: Prof. Dr. Wolfgang J.Parak

Dekan der Fakultät MIN: Prof. Dr.-Ing. Norbert Ritter

To my dearest daughter, Niki Behrooz,

who has been a constant companion to me
throughout the journey of completing my Ph.D. thesis.

With all my love,

Abstract

Heterogeneous catalysis plays an important role in many areas of the chemical industry such as oxidation reactions, and dehydrogenation reactions. In heterogeneous catalytic processes, the materials experience changes in their structure depending on variations in their chemical environment and in the course of their application, which can lead to a reduced function of the catalyst. A precise understanding of the processes taking place and the structural changes occurring on various length scales - from the atomic scale of catalytically active sites to the macroscopic scale - is therefore of great importance for industrial applications. In order to characterize these structural and chemical changes different techniques can be employed. Conventional spectroscopic characterization tools such as Raman spectroscopy allow real-time measurements, quantitative analysis and identification of reaction mechanisms.

X-ray microscopy can make an important contribution here, as it allows for the extraction of structural information from within samples in three dimensions, due to the relative weak interaction of hard X-rays with matter. Also, this technique can easily be combined with spectroscopy, allowing for the investigation of both the local density and the chemical state of a material. In this way, dynamic processes can be analyzed under operando conditions with high temporal and spatial resolution. In this work, methods were developed to combine X-ray full-field microscopy with X-ray absorption spectroscopy. The methodology was demonstrated on well-known chemical reactions as test systems at beamline P64 (PETRA III). This allowed for the investigation structural changes in the chemical oxidation state of a platinum catalyst during the catalytic partial oxidation of methane under operando conditions.

This initial 2D demonstration of the method was further extended to 3D using X-ray tomography, and the oxidative dehydrogenation of ethane to ethylene was investigated using this method. This enabled us to investigate the local chemical oxidation state of Molybdenum as catalytic material during operation. Overall, the results demonstrate the great potential of the method for visualizing chemical catalysis processes with high spatial resolution in 3D. These methods can be easily implemented at beamlines equipped with high X-ray flux, fast-scanning X-ray monochromators, and a suitable gas-phase analysis environment.

Zusammenfassung

Heterogene Katalyse spielt in vielen Bereichen der chemischen Industrie eine wichtige Rolle, z. B. bei Oxidationsreaktionen, und Dehydrierungsreaktionen. Bei heterogenen katalytischen Prozessen verändern die Materialien ihre Struktur in Abhängigkeit von Variationen in ihrer chemischen Umgebung und im Laufe ihrer Anwendung, was zu einer reduzierten Funktion des Katalysators führen kann. Ein genaues Verständnis der ablaufenden Prozesse und der strukturellen Veränderungen auf verschiedensten Längenskalen - von der atomaren Skala der katalytisch aktiven Zentren bis hin zur makroskopischen Skala - ist daher von großer Bedeutung für die industrielle Anwendung. Um diese strukturellen und chemischen Veränderungen zu charakterisieren, können verschiedene Techniken verwendet werden. Konventionelle spektroskopische Charakterisierungstools wie z. B. Raman-Spektroskopie erlauben Echtzeitmessungen, eine quantitative Analyse und die Identifizierung der Reaktionsmechanismen.

Röntgenmikroskopie kann hier einen wichtigen Beitrag leisten, da aufgrund der relativ schwachen Wechselwirkung von harter Röntgenstrahlung mit Materie strukturelle Information auch aus dem Inneren von Proben in 3D erhalten werden kann. Auch lässt sich die Technik leicht mit Spektroskopie kombinieren, so dass zusätzlich zur lokalen Dichte auch der chemische Zustand eines Materials untersucht werden kann. Auf diese Weise kann man daher dynamische Prozesse unter operando Bedingungen mit hoher zeitlicher und räumlicher Auflösung untersuchen. In dieser Arbeit wurden Methoden weiterentwickelt, Röntgenvollfeldmikroskopie mit Röntgenabsorptionsspektroskopie zu kombinieren. Die Methodik wurde an bekannten chemischen Reaktionen als Testsysteme an Beamline P64 (PETRA III) demonstriert. Dies erlaubte zum Beispiel die Untersuchung von strukturellen Veränderungen des chemischen Oxidationszustandes eines Platin-Katalysators während der katalytisch partiellen Oxidation von Ethan unter operando Bedingungen.

Diese erste 2D Demonstration der Methode wurde außerdem auf 3D mit Hilfe der Röntgentomographie erweitert und am Beispiel der Oxidativen Dehydrierung von Ethan zu Ethylen demonstriert. Dies erlaubte den lokalen chemischen Oxidationszustand des Molybdän-Katalysematerials während des Betriebs zu untersuchen. Insgesamt zeigen die Ergebnisse das große Potenzial der Methode für die Visualisierung von chemischen Katalyseprozessen mit hoher räumlicher Auflösung in 3D. Die Methode lässt sich leicht an Beamlines implementieren, die mit einem hohen

Röntgenfluss, einem schnell scannenden Röntgenmonochromator und einer geeigneten Gasphasen-Analyseumgebung ausgestattet ist.

Contents

List of Abbreviations

aRCTIC	Rotating Capillary for Tomographic In situ/ Operando Catalysis
ART	Algebraic Reconstruction Technique
BMs	Bending Magnets
CCM	Channel-Cut Monochromator
CCR	Catalytic Combustion and Reforming
CG	Conjugate Gradient
CPO	Catalytic Partial Oxidation
CT	Computed Tomography
CXDI	Coherent X-ray Diffraction Imaging
DCM	Double-Crystal fixed-exit Monochromator
DESY	Deutsches Elektronen-Synchrotron
DPO	Direct Partial Oxidation
EM	Effective Magnification
ESRF	European Synchrotron Radiation Facility
EXAFS	Extended X-ray Absorption Fine Structure
FBP	Filtered Back Projection
FOV	Field Of View
FPS	Frames Per Second
FRC	Fourier Ring Correlation
FT	Fourier Transform
GC	Gas Chromatography
GRAD	Gradient descent method with a constant step size
GRIDREC	fourier Grid Reconstruction algorithm
ID's	Insertion Devices
KB	Kirkpatrick Baez
KIT	Karlsruhe Institute of Technology
LCA	Linear Combination Analysis
MCR-ALS	Multivariate Curve Resolution-Alternating Least Squares
ML	Machine Learning
MLEM	Maximum-Likelihood Expectation Maximization
MS	Mass Spectrometry
NA	Numerical Aperture
NEXAFS	Near Extended X-ray Absorption Fine Structure
ODH	Oxidative Dehydrogenation
PCA	Principal Component Analysis

PETRA	Positronen-Elektronen-Tandem-Ring-Anlage
PI	Principal Investigator
PLOT	Porous Layer Open Tubular
PSI	Paul Scherrer Institut
Pt	Platinum
QEXAFS	quick-EXAFS
QM	Quantum Mechanics
QW	Quartz Wool
ROI	Regions Of Interest
SART	Simultaneous Algebraic Reconstruction Technique
sCMOS	scientific Complementary Metal-Oxide-Semiconductor
SIRT	Simultaneous Iterative Reconstruction Technique
SLS	Swiss Light Source
SR	Synchrotron Radiation
SRM	Steam Reforming of Methane
SXRM	Scanning X-ray Microscopy
TUHH	Technische Universität Hamburg
UHH	Universität Hamburg
XANES	X-ray Absorption Near Edge Structure
XAS	X-ray Absorption Spectroscopy
XRM	X-ray Microscopy
WD	Working Distance

1 Introduction

Synchrotron radiation (SR) sources provide a wide range of analytical methods and techniques for studying a variety of scientific and industrial fields, including materials science, structural biology, chemistry, and medical imaging [1, 2]. X-ray microscopy (XRM) is a powerful imaging technique to provide detailed information about the structure of the samples. Since X-rays have a short wavelength and a large penetration depth, they are ideal for imaging samples at high spatial resolution.

Catalysts are widely used to produce a significant amount of chemical products in the chemical industry. In heterogeneous catalysis, catalysts and reactants exist in different phases, and materials undergo dynamic structural changes based on their chemical environment [3]. As the structure and function of catalysts are closely related and the structural response of a catalyst system is not necessarily uniform in many cases under working conditions, spatially and temporally resolved catalyst characterization is critical to provide a comprehensive insight into the functioning of a catalyst system [4–6].

The combination of spectroscopy and microscopy methods based on hard X-rays has attracted attention for its ability to provide spatially resolved structural information [7, 8]. Among the different in situ spectroscopic techniques [9], X-ray absorption spectroscopy (XAS) is a powerful technique in catalysis research that can provide structural information on the oxidation state of elements within the material [10, 11]. However, conducting both spatial and time-resolved studies simultaneously with conventional spectroscopic characterization tools under operando conditions is challenging due to the technical complexity of experimental setups, the requirement for data synchronization, and the stability of samples.

The first part of this thesis expands the above idea by developing the experimental method for the rapid operando 2D X-ray absorption near edge spectroscopy (XANES) imaging with spatial and temporal resolution simultaneously at the beamline P64, PETRA III. By recording sequences of 2D transmission images of the catalytic bed at different energies around an absorption edge of an element of interest, a detailed description of the chemical state of this type of atom can be obtained for each pixel in the images. This X-ray spectro-microscopy can be used to provide information about dynamic processes in catalysts and other functional materials under working conditions [12].

In the second part of this thesis, the previous 2D XANES imaging technique is extended to 3D. By acquiring complete tomographic data sets at different energies around an absorption edge of some element, detailed information about the chemical state of this type of atom can be obtained for each voxel of the volume. The method, also known as spectro-tomography, can be used to visualize the chemical state of a catalytic reactor in 3D under operando conditions as a function of time.

This thesis is organized as follows:

In Chapter 2, an overview of SR, XAS, and XRM is given. In Chapter 3, a description of the beamline P64 at PETRA III as well as the experimental setups implemented for rapid 2D and 3D XANES imaging are presented.

Due to the large volume of data that was collected during the study of chemical reactions by 2D and 3D XANES imaging methods, an optimized data evaluation pipeline has been developed in Python. A description of the measurement methods and analysis of each of them are provided in Chapter 4.

In Chapter 5, a rapid 2D XANES imaging technique with temporal and spatial resolution is developed using a quick-extended X-ray absorption fine structure (QEXAFS) monochromator and a high-resolution X-ray camera. This method is tested by 2D imaging around the Pt L_3 absorption edge of a model Pt/Al_2O_3 catalyst inside of the quartz capillary during catalytic partial oxidation of methane [12] and the results of this study are presented in this chapter.

In Chapter 6, rapid tomography XANES imaging measurement with spatial, temporal, and energy resolution under operando conditions is performed by utilizing the Rotating Capillary for Tomographic In situ/ Operando Catalysis (aRCTIC) sample environment [13]. This method is tested by 3D imaging of a model Mo/Al_2O_3 catalyst inside a sample environment during oxidative dehydrogenation of ethane and results are presented in this chapter.

2 Theoretical Background

The main mathematical and physical concepts related to X-ray imaging with absorption contrast are presented in this chapter. Due to the photon-hungry nature of this technique at high spatial resolution, the experiments are carried out at SR sources that provide the required X-ray flux (see Sec. 2.1). Since the focus of this study is X-ray imaging using absorption contrast, Sec. 2.2 provides a detailed explanation of this principle. The basic principle of XAS is given in Sec. 2.3 with a description of various regimes of the XAS spectrum.

The imaging techniques used in this research, full-field 2D and 3D XANES imaging, with the mathematical formulation are described in the XRM Section (Sec. 2.4). Finally, in order to determine the application of these imaging techniques, the heterogeneous catalysts were selected as a case study and are introduced briefly in Sec. 2.5.

2.1 Synchrotron Radiation

SR is electromagnetic radiation with high energy and desirable spectral characteristics. In the initial step, electrons are accelerated in the linear accelerator. Afterwards, in the booster, electrons reach their final speed and are then injected into the storage ring, in which the electrons are stored over extended times. As electrons are lost, the storage ring is refilled in certain intervals with electrons to maintain a constant number of electrons in the ring. Bending magnets (BMs) are used to deflect the electrons from their straight path and store them in a closed loop, alternating between round and straight sections.

In the straight sections of the storage ring, additional magnetic structures, known as Insertion Devices (ID's) such as 'wigglers' and 'undulators,' are installed. Today, the 'wigglers' and 'undulators' are used as the main sources of SR. In the following paragraphs, some details related to the characteristics of the radiation emitted by wigglers and undulators will be introduced.

Charged particles circulate with a high velocity near the speed of light in these storage rings. The relation between particle speed and energy is given by the relativistic formulas as shown below:

$$E_e = \gamma m_e c^2 \tag{2.1}$$

$$\gamma = \frac{1}{\sqrt{(1-\beta^2)}} \tag{2.2}$$

$$\beta = \frac{v}{c} \approx 1 - \frac{1}{2\gamma^2}, \tag{2.3}$$

where E is the energy, m_e is the mass of the electron, c is the speed of light and v is the particle speed.

Emitted radiation has the typical dipole distribution in the reference frame of a moving electron (see Fig. 2.1(a)). In the laboratory frame, however, the radiation is emitted into a small cone in the forward direction with an angle of $\theta \approx \gamma^{-1}$ due to relativistic aberration effects (see Fig. 2.1(b)) [14].

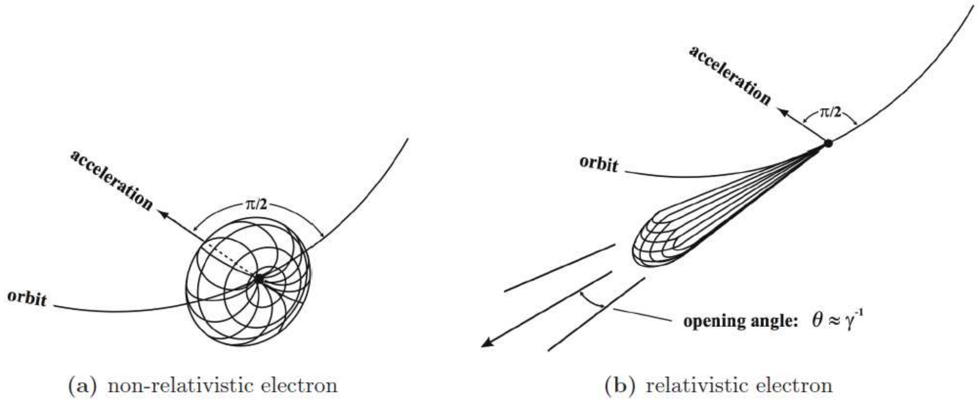

(a) non-relativistic electron

(b) relativistic electron

Figure 2.1: The spatial distribution of emitted radiation for different electron energies; Reprinted from Ref. [15].

Fig. 2.2 illustrates an alternating magnetic structure change in these ID's in the direction of the particle's propagation, causing the particle to perform an almost sinusoidal motion. In this figure, λ_u, $N_{\mathrm{ID's}}$, and $\alpha_{\max}$ represent the ID's period, the number of magnetic periods, and the maximum deflection angle. The distance h between poles can be adjusted, thereby changing the magnetic field strength in the ID. The undulator and wiggler can be distinguished from each other by a certain value of a factor κ. This factor is a multiple of the opening angle of the emission cone, γ, with maximum deflection angle α_m, where $\kappa = \alpha_\mathrm{m}{\cdot}\gamma$.

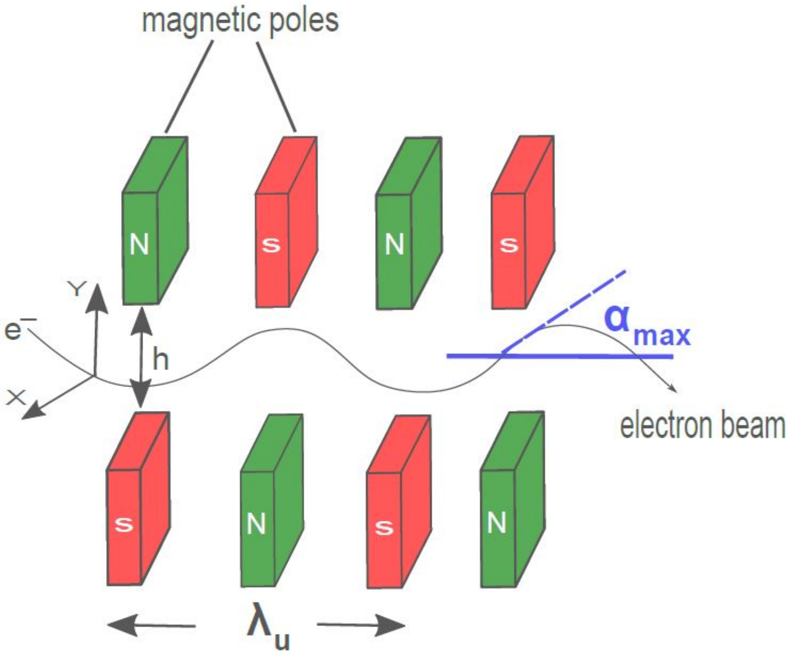

Figure 2.2: A beam of electrons passing through the ID's.

The wiggler is the ID with a strong magnetic field. In the wiggler, the opening angle of the emission cone is much smaller than the maximum deflection angle:

$$\frac{1}{\gamma} \ll \alpha_m \leftrightarrow \kappa \gg 1 \tag{2.4}$$

Since the wiggler emits light from different angles, the light emitted from different points does not interfere with one another and the overlap will be minimal. Therefore, source points can be considered independent and intensified by increasing the number of magnetic poles. The emission intensities of each magnetic pole in the wiggler add up to each other to obtain the whole emission intensity of the wiggler. This means that the probability of the emission of a photon in the wiggler is calculated as the sum over the squared probability amplitudes of emitting a photon at each magnet. Consequently, a wiggler emits X-ray radiation with a spectrum similar to a BMs, but intensified by the number of poles $2N$ [16].

In comparison, the undulator is built and designed such that the maximum deflection angle is similar to the emission cone of single electrons (see Eq. 2.5).

$$\frac{1}{\gamma} \geq \alpha_{max} \leftrightarrow \kappa \leq 1 \tag{2.5}$$

Therefore, interference effects related to photon emission events originating from the different undulator poles become relevant. Thus, a strong intensity increase is observed at certain harmonic frequencies due to constructive interference of emission amplitudes. In this case, the emitted intensity scales as N^2 at these wavelengths. In consequence, at undulator strongly enhanced radiation emission in narrow energy bands with an intensity that is now scaling to the number of poles squared N^2.

The wavelength of the j-th harmonic can be described as follows [16]:

$$\lambda_j = \frac{\lambda_u}{2\gamma^2 \cdot j}(1 + (\frac{\kappa^2}{2}) + \gamma^2\theta^2) \qquad j = 1, 2, 3, ... \tag{2.6}$$

where j is the number of given harmonics, λ_u is the undulator periods, and θ is the angle between the direction of observation and the undulator axis. As κ depends on the magnetic field, changing the magnetic field by changing the gap of the undulator and the maximum deflection angle allows us to tune the line spectrum and adjust the wavelength and κ factor for the measurements.

In the undulator, the interference effects lead to smaller angular divergence of the X-ray light in comparison to light produced by the wiggler or the BMs and it causes the beam to be even more collimated. X-ray light produced with the undulator is linearly polarized in the plane of undulation (horizontally). With the following formula, the divergence of light, where the emitted intensity falls to zero, can be determined [16]:

$$\sigma = \frac{1}{\gamma}\sqrt{\frac{3}{4\pi}} \cdot \frac{1 + \frac{\kappa^2}{2}}{jN_u} \tag{2.7}$$

Specific features of light produced with the undulator cause the undulator considered as the most powerful source of SR. Therefore, wigglers and BMs are replaced by undulators in most SR sources.

In addition to producing synchrotron radiation, the X-ray sources are specially designed to produce a beam with high brightness, a small angular divergence, and a small size. This combination of parameters is used to measure the quality of an X-ray source and is referred to as spectral brightness. The photon source's brightness is determined by a photon flux per phase space. In this way, the spectral brightness,

B_{sp}, is described in the following manner [17]:

$$B_{sp} = \frac{F}{\Omega \cdot A \cdot \Delta E/E} \tag{2.8}$$

This parameter is a ratio between the photon flux ($\frac{photons}{s}$), the solid angle Ω [mrad^2] into which radiation is emitted, source area A [mm^2] and the energy bandwidth $\frac{\Delta E}{E}$ $\approx 0.1\,\%$ bandwidth.

Higher spectral brightness is ultimately associated with higher available photon flux at the experiment and therefore enables experiments with higher temporal or spatial resolution. As the coherent portion is the total X-ray flux and is directly proportional to the brilliance of the source, a high degree of coherence light allows us to get a nice and sharp phase contrast image.

2.2 Photoelectric Absorption

Today atoms are understood in terms of quantum mechanics (QM) and have different energy levels. The electron configuration of an atom is a representation of the way electrons are distributed among its atomic orbitals and it follows certain principles based on QM, see reference [18] for more details.

Photoelectric absorption is a process in which the X-ray photon interacts with the atom, getting absorbed in the process. The excess energy is then transferred to an electron located at a lower energy level (for example, n=1, K shell). Consequently, an electron is ejected from the atom, termed a photoelectron, resulting in the ionization of the atom [17]. This process is illustrated in Fig. 2.3.

In this way, the atom becomes ionized by ejecting an electron from an inner shell and a hole is created within that shell. As an atom with a core electron removed is unstable, it has a preference for having the inner energy level filled. To fill this hole by an electron from an outer shell, one of the following reverse processes may be used: fluorescent X-ray emission or Auger electron emission, see references [19, 20] for more details.

The fluorescent X-ray emission (see Fig. 2.4 (a)) occurs when one of the electrons in the outer shells of the atom (L or M shell) undergoes a transition into the inner shell (K shell) and fills its hole. If the electron ejects from L to K shell, it emits a photon with an energy equal to the energy differences between the binding energies

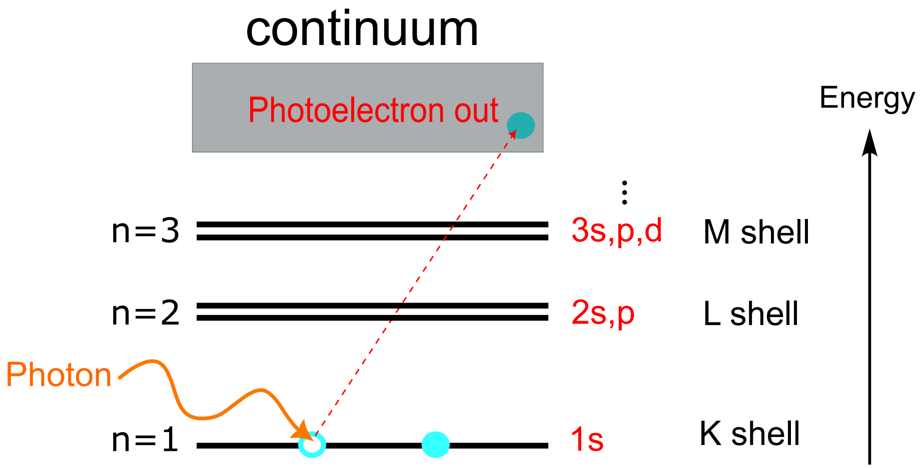

Figure 2.3: Schematic diagram of photoelectric absorption. An electron residing in the lower energy level of the atom is excited to the upper level of the atom by absorbing the X-ray photon energy and leaving an empty state in the lower energy level. The transitions between energy levels follow the selection rules (see Eq. 2.14).

of the K and L shell and the radiation emitted is referred to as fluorescent radiation K_α line. When the transition happens from M to K shell, the K_β line is formed. As the energy of fluorescent radiation is element-specific, this method can be used to determine the elemental composition of a sample.

In the Auger electron emission process, a hole in the inner shell (K shell) is filled by an internal process when an electron from the outer energy level transitions into the hole [21]. This process is shown in Fig. 2.4 (b). The energy of an Auger electron, E_A can be derived from below formula:

$$E_A = E_M + E_L - E_K \tag{2.9}$$

where E_A is the energy of an Auger electron, E_M is the energy of an electron in M shell, E_L is the energy of an electron in L shell, and E_K is the energy of an electron in K shell. As each element has specific energy associated, Auger electron spectroscopy enables us to detect all chemical elements except hydrogen and helium by detecting the Auger transition intensities.

As described the incident X-ray beam interacts and absorbs within atoms of the sample, thereby reducing the X-ray intensity while propagating through the sample volume, see Fig. 2.5. The amount of the sample absorption can be determined with the absorption coefficient μ. For a constant linear attenuation coefficient, the

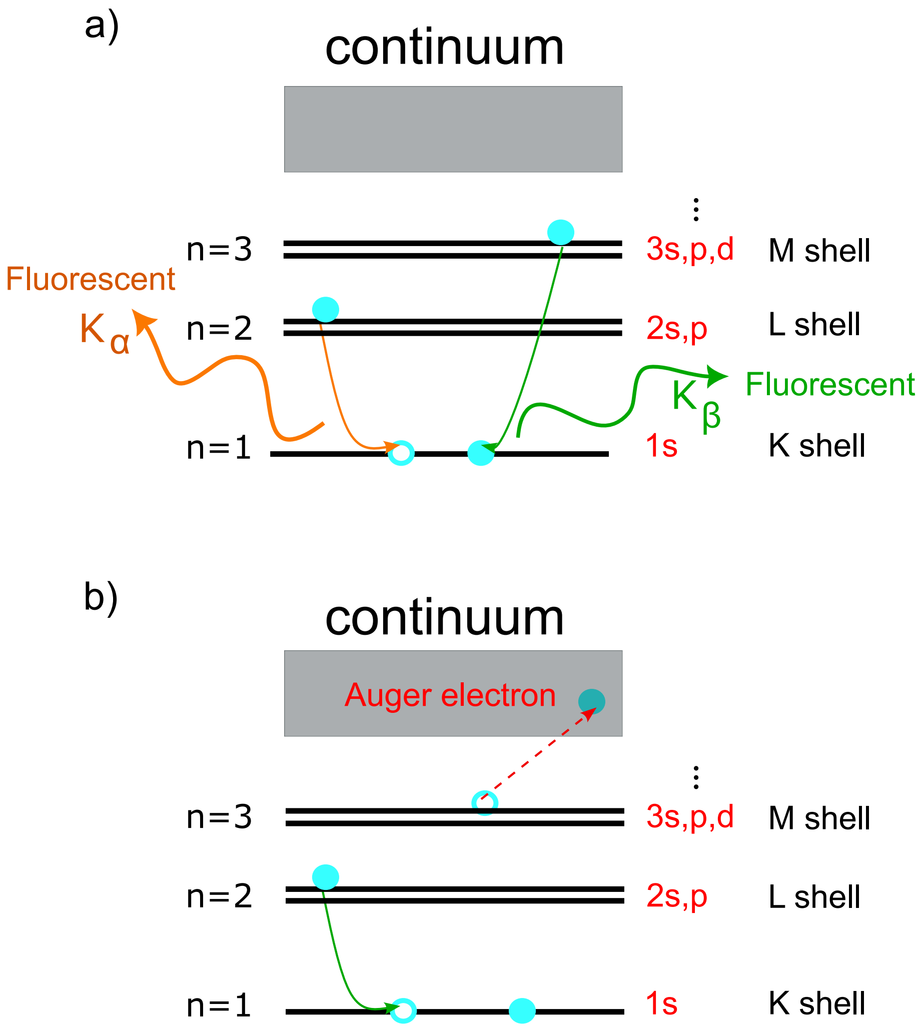

Figure 2.4: (a) Schematic diagram of fluorescent X-ray emission. An upper electron in the L or M shell drops to fill the vacancy in the K shell by emitting photons. This photon is known as fluorescent radiation and is labeled by K_α or K_β; (b) Schematic diagram of Auger electron emission. The transitions between energy levels follow the selection rules (see Eq. 2.14). Not all electrons in each shell are depicted here. As an example, only one of the electrons in each shell that contributes to the transition is shown.

attenuation effect is well described by the Lambert-Beer law (see Eq. 2.10) and detailed descriptions about it can be found in the [17].

$$I(z) = I_0\, e^{-\mu z} \tag{2.10}$$

In this equation, the I_0 is described as the incoming X-ray intensity, μ is the linear attenuation coefficient, z is the thickness of the material, and I is the transmission X-ray intensity.

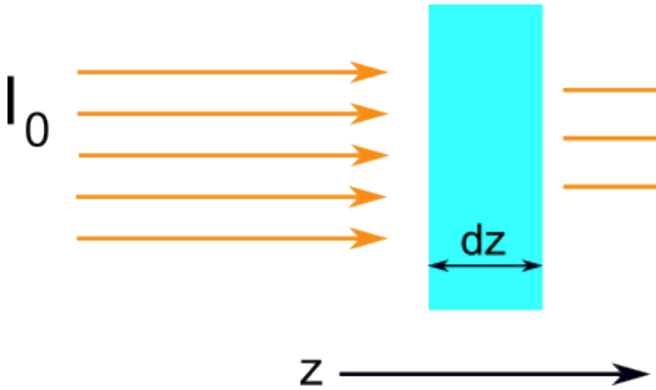

Figure 2.5: The X-ray beam intensity decays exponentially while propagating through the sample.

According to the Lambert-Beer-Law equation (see Eq. 2.10), the attenuation of the beam inside of the sample can be obtained by measuring the incoming and out-coming X-ray beam intensity in the experimental measurements. Also, an X-ray absorption spectrum can be determined by the ratio between the intensity of the beam in front of the absorber (I) and in behind it (I_0), while the photon energy is altered which can provide information regarding the chemical state of materials.
The absorption coefficient can be calculated based on the sample's absorption cross-section σ_a too. Actually, an absorption cross-section measures the probability of electromagnetic radiation being absorbed by a particle. It is defined as the ratio between the amount of radiation absorbed by the sample and the amount of incident radiation per unit of cross-sectional area and is commonly expressed in square centimeters. Based on it, the absorption coefficient can be defined as follows [17]:

$$\mu = \rho_a \, \sigma_a = \frac{\rho_m N_A}{A} \sigma_a \tag{2.11}$$

where ρ_a, N_A, ρ_m and A are the atomic number density, the Avogadro's number, the mass density, and the atomic mass number respectively.

As the absorption cross section is approximately proportional to the energy $E^{\text{-}3}$ and the atomic number of the absorber Z^4, it causes the attenuation coefficient decreases with increasing photon energy as follows [22]:

$$\mu \approx \frac{\rho Z^4}{A E^3} \tag{2.12}$$

As the atomic mass number is proportional to the Z, the attenuation coefficient has a strong dependence on X-ray energy $E^{\text{-}2.78}$ and the atomic number $Z^{2.7}$ for the complicated structure of the atoms. If the sample consists of different elements, the mass attenuation coefficients can be calculated by adding up each component's contribution (Eq. 2.13):

$$\frac{\mu}{\rho} = \sum_i \frac{\mu_i}{\rho_i} \cdot c_i \tag{2.13}$$

where c_i is the weight concentration of each component [22].

Briefly, the absorption coefficient refers to the measure of a material's ability to absorb a particular type of electromagnetic radiation, such as X-ray light. This parameter is used to determine the concentration of absorbing species in a sample as well as to study the interaction of light with matter in XRM [17].

The following section focuses on the X-ray absorption process in more detail.

2.3 X-ray Absorption Spectroscopy

XAS is a powerful analytical technique used to investigate the chemical and electronic properties of materials. This technique involves shining X-ray radiation with diverse energies at a sample and measuring how much radiation is absorbed by the sample as a function of energy (see Eq. 2.10). There is a brief description of this technique here and more details are available in [20].

Fig. 2.6 represents the atomic structure of the molybdenum. An X-ray beam with sufficient energy shines on it. When the photon energy reaches the binding energy of the certain shell, the photoelectron can be excited from a strongly bound core level (K-shell) to a high-energy unoccupied state. The resulting spectrum is known as the XAS spectrum and provides information about the element-specific electronic and atomic environment of the material.

However, a series of selection rules for the excitation of electrons as well as which transitions are allowed or prohibited between different states describe the transition conditions as follows [23]:

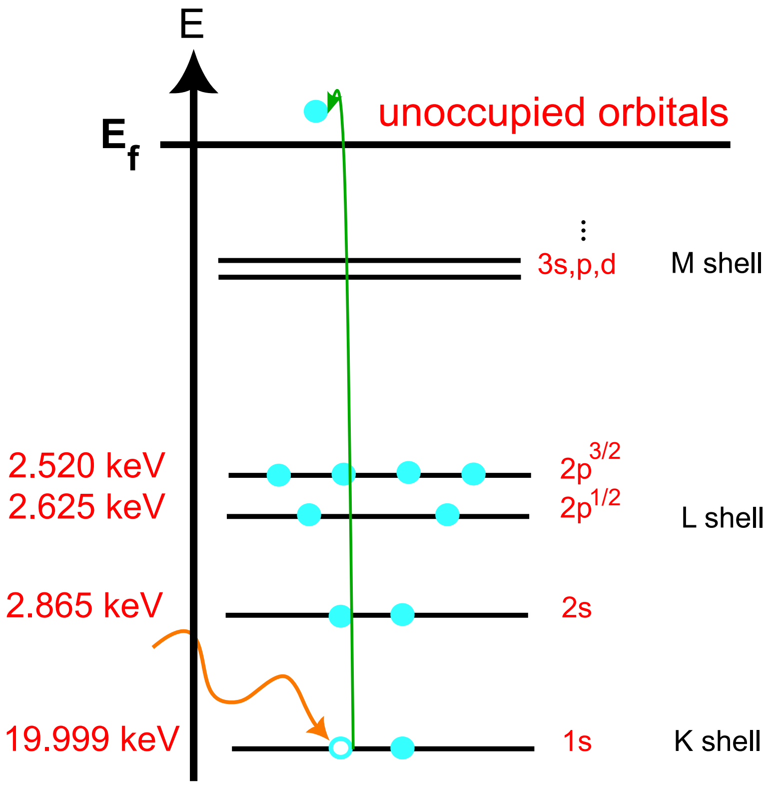

Figure 2.6: The atomic structure of molybdenum with different shells. The set of selection rules (Eq. 2.14) describes the transition of electrons between shells.

$$\begin{array}{rr}
 & \triangle n \neq 0 \\
\triangle l = \pm 1 & \triangle L = 0, \pm 1 \\
\triangle m_l = 0, \pm 1 & \triangle S = 0 \\
\triangle m_s = 0 & \triangle J = 0, \pm 1 \\
\triangle m_j = 0, \pm 1 & \leftrightarrow \quad \textit{not} \quad \textit{allowed}
\end{array} \tag{2.14}$$

where the n, L, S, and J are the principal quantum number, orbital angular momentum, spin angular momentum and total angular momentum, respectively. During the electron's transition, one must also consider the Pauli exclusion principle, which states that within an atom, no two electrons in an atom can occupy the same quantum state that means have the same quantum number such as angular momentum, magnetic moment, and spin [23].

The probability of transitioning from one quantum state to another (from an initial state $\mid i\rangle$ to a final state $\mid f\rangle$) per unit of time can be calculated with Fermi's Golden

Rule. According to this rule, the transition rate depends on the matrix element of the dipole Hamiltonian between the initial and final state. Fermi's Golden Rule describes with:

$$\Gamma = \frac{2\pi}{\hbar} | \sum_{f} \langle f \mid H \mid i \rangle |^2 \delta(E_f - E_i - \hbar\omega) \tag{2.15}$$

where H is the dipole Hamiltonian and refers to the interaction between the electric dipole moment of a system and the external electric field and the Dirac delta function δ describes the energy conservation of the process. E_{f} and E_{i} describe the final and initial energy levels of the transition [20]. Besides providing important information about the energy levels and transitions of the system, this equation enables to make predictions about how the system will behave under different conditions.

As every element in the sample has a characteristic X-ray absorption spectrum, the shape and intensity of the X-ray absorption spectrum can provide information about the local environment and coordination of atoms, elemental identity, the oxidation state of the element, electronic configuration, and the chemical bonding. Thus, XAS is used to study the composition, structure, and properties of materials in a wide range of fields including materials science, chemistry, biology, and environmental science. Each XAS spectrum includes different regions: the pre-edge region, the absorption edge, and the post-edge which includes the XANES regime and the extended X-ray absorption fine structure (EXAFS) regime. These regions are shown in the Fig. 2.7.

The absorption edge in the X-ray absorption spectrum refers to the sharp increase in X-ray absorption that occurs when the binding energy of the core electrons in the sample matches with the energy of the incident X-rays. In this case, the X-ray beam is absorbed by the electron in the core-shell of atoms and the electron is promoted to higher energy levels [25]. It's important to note that the energy of the absorption edge is specific to the type of atom absorbing the X-rays and it is determined by the energy required to remove an electron from the inner shell.

The pre-edge designates the region of the spectrum that occurs just before the absorption edge, while the post-edge refers to the region after the absorption edge in the X-ray absorption spectrum. Within the post-edge region, the X-ray absorption coefficient progressively rises with increasing X-ray energy and includes multiple peaks or oscillations. The post-edge analysis can provide information regarding the coordination and local symmetry of the absorbing atom as well as the nature of

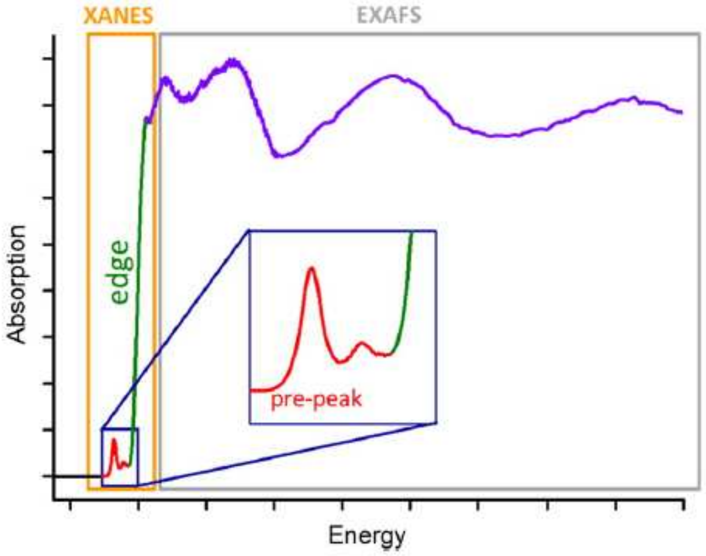

Figure 2.7: Here is a general schematic representation of the X-ray absorption spectrum, which consists of different regions within its spectrum; Reprinted from Ref. [24].

the unoccupied electronic states. Also, it is possible to determine the valence state, oxidation state, and local bonding environment of an atom by observing the intensity and shape of post-edge features. The XANES and EXAFS techniques are commonly utilized for post-edge analysis [26]. These techniques are discussed in more detail in the following:

2.3.1 X-ray Absorption Near Edge Structure

The term XANES refers to X-ray Absorption Near-Edge Structure and it is used for the high-energy X-ray range. This region typically begins 10 eV below the absorption edge and extends 50–100 eV above it. The XANES is a fingerprinting technique that can identify and characterize elements in a material based on spectral features such as oxidation state, local coordination environment, and electronic configuration [25]. As a powerful spectroscopic technique, it can be used to determine the local unoccupied projected density of electronic states.

In this technique, X-ray energy is tuned to be near the absorption edge of an interest element in the sample and illuminate on a sample. Afterwards, the transmitted X-ray intensity is measured typically as a function of the incoming X-ray energy yielding an X-ray absorption spectrum. The physical processes behind the absorption of X-ray photons in matter are related to the transition of core electrons to unoccupied states right below the continuum of free electron states [17]. The shape of the spectrum is defined by the density of states in the vicinity of the absorption edge. Due to the likelihood of a higher density of bound states near the edge compared to unbound states, the absorption spectrum displays a peak [17]. Thus, the XANES region exhibits distinct characteristics such as sharp peaks, shoulders, or features in proximity to the absorption edge.

Here is an overview of the types of information extractable from XANES [20]:

- Electronic structure: As the shape and intensity of XANES spectra are related to the density of states of the unoccupied electronic states of the material, XANES can give insight into the electronic structure of a material. Furthermore, this technique enables the measurement of all unoccupied states surrounding the atom, which are accessible for electron transitions.
- Coordination environment: XANES is capable of revealing whether an atom is surrounded by other atoms or molecules as well as providing information about an atom's local coordination environment and the distances between atoms.
- Oxidation state of atoms: XANES technique is capable of revealing an atom's oxidation state. Due to that the absorption energy of an X-ray relies on the electronic configuration of the absorbing atom, this configuration is influenced by the atom's oxidation state.
- Chemical bonding: As an atom's electronic structure influences the X-ray absorption energy, XANES can provide information about its chemical bonds with its neighboring atoms.
- Local structural disorder: XANES can also provide information regarding the local structural disorder such as distortions or defects in a material's crystal structure.

When the photoelectron is ejected into a partially occupied molecule, valence orbital, or another atom, fewer electrons remain more tightly within its inner shell in an atom. Consequently, the oxidation state shifts the absorption edge's energy several eV. For instance, the XANES spectra corresponding to various oxidation states of molybdenum are shown in Fig. 2.8 [27]. As expected absorption edge of molybdenum shifts to higher energies with an increasing oxidation state indicating that the inner 1s electrons are more strongly bound to the atomic nucleus.

Overall, XANES is an invaluable tool in a wide variety of scientific fields including materials science, chemistry, physics, and geology, enabling the exploration of

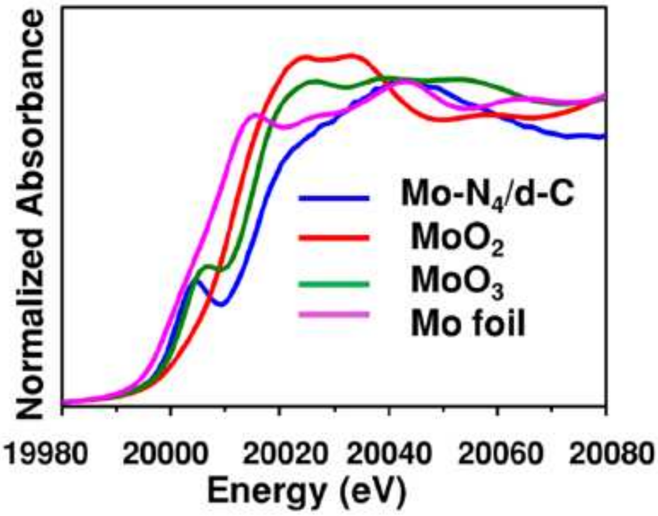

Figure 2.8: The K-edge XANES spectrum for different oxidation states of molybdenum and Mo-N_4/d-C sample. The edge position of the MoO_2 (red line) has a shift around a few eV in comparison with the edge position of the MoO_3 (green line) and Mo as the foil; Reprinted with permission from Ref. [27]. Copyright 2022 American Chemical Society.

material properties in catalysts, semiconductors, batteries, and providing enhanced comprehension of materials' local structure [25].

2.3.2 Extended X-ray Absorption Fine Structure

The term EXAFS stands for Extended X-ray Absorption Fine Structure. The EXAFS's region usually starts in the range from 100 eV to keV range above the absorption edge of the element [17]. Depending on the element to be studied and the edge to be probed, this energy range may vary [22].

In the EXAFS energy range, the photon energy is far above the ionization threshold and the photoelectron is liberated which propagates as a spherical wave (Fig. 2.9) [22, 28, 29]. When the spherical wave of the absorber atom is emitted, it is scattered off the atom in the surroundings, leading to the interference pattern. In this way, the EXAFS structure results from the backscattering of the photoelectron by the surrounding atoms.

Based on the interference between outgoing photoelectron waves and the backscattered waves from neighboring atoms (constructive or destructive), the final state is determined. In the EXAFS spectra, maximum oscillations represent construc-

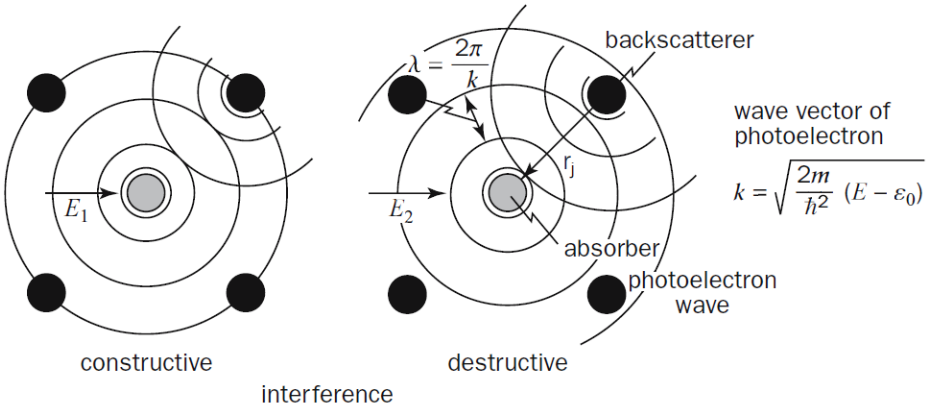

Figure 2.9: The photoelectron emitted in the absorption process propagates as the spherical wave from the absorber atom. If other atoms are located, the photoelectron is scattered by neighbors, and the incoming and scattered waves may interfere. The EXAFS oscillation is the result of the constructive and destructive interference between these waves; Reprinted from Ref. [28].

tive interference between waves while minimum oscillations represent destructive interference. In the EXAFS region, the oscillations appear as a series of oscillatory modulations beyond the absorption edge.

As the incident photon has energy E above the absorption edge energy, the removal of a core-level electron from an atom occurs and the excess energy goes into the kinetic energy of photoelectron E_{kin} as the following [28]:

$$E_{kin} = E - \varepsilon_0 = \frac{p^2}{2m_e} \tag{2.16}$$

where ε_0 is the absorption edge energy, p is the momentum of the electron and m_{e} is the electron's mass.

As the wave number of a photoelectron k is connected to its momentum by $p = \hbar k$, the relationship between the wave number of a photoelectron and its energy can be expressed as follows [28]:

$$k = \sqrt{\frac{2m}{\hbar}(E - \varepsilon_0)} \tag{2.17}$$

From an EXAFS spectrum, various crucial atomic structural details can be derived. These include determining the coordination number, establishing the distance between the absorbing atom and its neighboring atoms, identifying neighboring atoms' chemical composition, and even discerning local structural alterations, for more details see [29].

A variety of software packages are available for analyzing XAS spectra. Demeter (Data Extraction, Modeling, and Estimation Toolbox for EXAFS and XANES) software package is one of the most popular and powerful tools used for this purpose with three components: Athena (analysis of XAS data), Artemis (include EXAFS and XANES) data), and Hephaestus (consists of tables about the X-ray absorption coefficients and elemental data). Demeter allows for the processing and analysis of XAS data, including tasks such as background removal, normalization, Fourier transform (FT), curve-fitting, and data simulation. Further information regarding this software is available in the [30].

As the combination of X-ray absorption spectroscopy and X-ray microscopy imaging is well-suited to providing local structural information on materials, this thesis emphasizes the utilization of the XANES technique in imaging applications. In this way, a brief introduction to X-ray microscopy is given in the following. Further details about X-ray microscopy can be found in [20].

2.4 X-Ray Microscopy

X-ray microscopy is an imaging technique that produces high-resolution images of objects on a microscopic or nanoscopic scale and allows the examination of the internal structure of the material. Three types of microscopic studies utilizing both soft and hard X-rays are as follows:

- Full-field X-ray Microscopy.
- Scanning X-ray Microscopy.
- Coherent X-ray Diffraction Imaging.

The following is a brief description of these techniques and more details can be found in [20].

2.4.1 Full-field X-ray Microscopy

Before interacting the X-ray beam with the object, it can be focused using different X-ray optics like refractive X-ray lenses, mirrors, and Fresnel zone plates. Subsequently, the highly sensitive detector records two-dimensional images of the internal structures of the object. In this technique, image contrast is primarily determined by differences in X-ray absorption, attenuation, and refraction properties of materials contained within the sample. Since different materials absorb and scatter X-rays differently, the intensity of the X-rays reaching the detector fluctuates based on the material type. Based on the complex refractive index n, it is possible to determine the coefficients of X-ray absorption and attenuation of an object as the following:

$$n(x, y, z) = 1 - \delta(x, y, z) + i\beta(x, y, z) \tag{2.18}$$

where δ corresponds to the real part of the complex refractive index and is the refractive index decrement. The phase shift of the X-ray wavefield after passing through a material can be determined from the $\int -k\, \delta(x, y, z)\, dz$. β represents the imaginary part of this index and describes the exponential attenuation of the X-ray intensity due to absorption within the object. By this method, the complex index of refraction of the object can be determined.

Full-field imaging involves a variety of geometries based on the sample's specific characteristics and the desired imaging outcome. It includes:

- Parallel beam geometry: the X-ray beam emitted from the synchrotron radiation source is collimated and the object is illuminated with a parallel X-ray beam. This geometry allows the capture of high-resolution and high-quality images. Through the examination of recorded images, detailed analysis and characterization of the sample's structure, composition, and properties become feasible. The schematic of this geometry is depicted in Fig. 2.10.
- Point projection imaging: it is also known as the magnified imaging technique. This technique aims to magnify and enhance specific regions or features of an object by focusing the X-ray beam in front of the object. This is achieved by placing focusing X-ray optics, such as Kirkpatrick-Baez (KB) mirror, the Fresnel zone plate, and the refractive lens. Afterwards, from this secondary source, the magnified projection can be recorded by the detector. Based on the distance between the focus (secondary source) and detector L_2 and the distance between the sample and focus (secondary source) L_1, the magnification M can

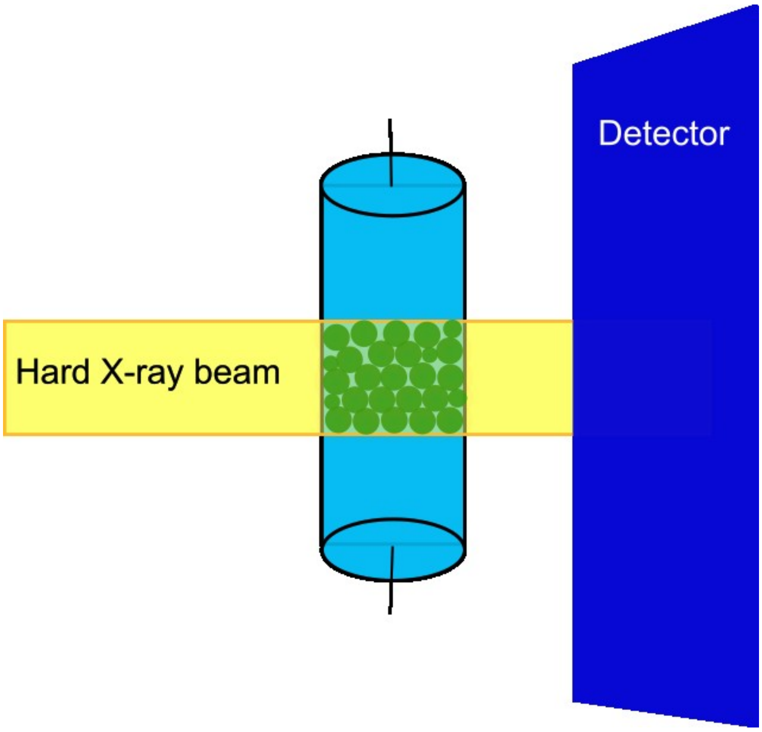

Figure 2.10: The parallel beam geometry.

be determined as follows:

$$M = \frac{L_2}{L_1} \tag{2.19}$$

- Magnified imaging with an objective lens: it involves combining X-ray imaging with an optical objective lens to obtain high-resolution and magnified images of an object. In this technique, the collimated or focused X-ray beam passes through the object. The magnified X-ray images on the detector are produced by placing the optical objective lens downstream of the sample [31].

Full-field imaging in combination with tomography is commonly known as full-field tomography, blending the respective advantages of both techniques. Through the use of the parallel beam and rotation of the object in this technique, a series of 2D projections of the object under different angles are recorded by the detector. From this angular projection series the 3D structure of the sample can be determined by using tomographic reconstruction algorithms [10]. A detailed description of the tomography is provided in the following (see Sec. 2.4.4).

2.4.2 Scanning X-ray Microscopy

Scanning X-ray Microscopy (SXRM) allows us to study the internal structures of the sample at the nano-scale level. This technique uses a variety of X-ray optics, including KB mirrors, multilayer Laue lenses, refractive X-ray lenses, and Fresnel zone plates, to focus the X-ray beam onto an object. This focused micro- or nanobeam is used to scan the sample and the transmitted or scattered X-ray beams are recorded on the detector.

SXRM includes several types such as scanning transmission X-ray microscopy (STXM), scanning X-ray fluorescence microscopy (SXRFM), X-ray diffraction (XRD) in the wide and small angle regimes (WAXS and SAXS), and absorption spectroscopy with various contrasts. Depending on which technique is used, information can be obtained regarding the composition and distribution of elements (using the SXRFM technique), the local structural information (through the STXM technique), as well as the chemical properties of a given species (through the XAS microscopy) [8]. The spatial resolution of the recorded images in the STXM technique is limited by the focus size.

2.4.3 Coherent X-ray Diffraction Imaging

The coherent X-ray diffraction imaging (CXDI) technique is based on using coherent X-ray light without relying on X-ray optics for scanning the object. As X-ray optics are not used in this technique, the spatial resolution is not limited by the numerical aperture and lies on the nano-scale [32]. In this geometry, the coherent X-ray beam is shined onto the object and scattered in various directions. Interfering the scattered X-ray beams with each other produces diffraction patterns in a far-field on a detector. In this diffraction pattern, the amplitude (intensity) of the scattered waves is displayed and the phase information can be extracted with additional knowledge using mathematical algorithms known as phase retrieval methods [33]. Using the phase information retrieved, an image of the object is reconstructed, depicting its internal structure.

For selecting the type of microscopic geometry for studying the sample, factors such as sample characteristics, resolution needs, imaging depth, contrast sensitivity, and sample stability should be taken into account. As tomography has the capability to generate a cross-sectional view of an object without the need for physical dissection, it was employed in this research for sample characterization. Therefore, a comprehensive explanation of the tomography method is presented in the subsequent section.

2.4.4 Tomography

X-ray computed tomography (CT) is a well-established technique for discovering the inner structure of an object without physically cutting it. Detailed descriptions of computed tomography can be found in Kak [34]. In the following sections, a brief overview of the mathematical concept behind CT as well as tomographical principles and its requirements in three dimensions discussed.

2.4.4.1 Basic Principle

The X-ray shines on the sample, traversing through it, and interacts with the electrons of the sample. During this interaction, X-ray acquires a small phase shift, which can be represented by δ, as well as some attenuation, which can be represented by β. These parameters are defined in the complex refractive index of refraction, see Eq. 2.18 and the relation between the attenuation coefficient μ and attenuation β is given by:

$$\mu(x,y,z) = \frac{4\pi}{\lambda} \cdot \quad \beta(x,y,z) \tag{2.20}$$

The transmission function, depicting the correlation between the properties of incoming X-rays and the outcoming light after passing through an object, is derived by combining phase shift and attenuation parameters as follows:

$$T(x,y,z) = e^{ik\triangle x} \cdot \exp\left\{-ik \int_{l(y,z)} \delta(x,y,z)\, dx\right\} \cdot \exp\left\{-\frac{1}{2} \int_{l(y,z)} \mu(x,y,z)\, dx\right\} \tag{2.21}$$

In this equation, the $e^{ik\triangle x}$ is the phase factor and independent of the object, $\exp\left\{-ik \int_{l(y,z)} \delta(x,y,z)\, dx\right\}$ describes the phase shift of the X-rays due to refraction and $\exp\left\{-\frac{1}{2} \int_{l(y,z)} \mu(x,y,z) dx\right\}$ represents attenuation. Assuming the object is thin, multiplying the incoming wave field by this transmission function allows us to determine the exit wave field directly after the object.

For modeling tomographic data evaluation, the coordinate systems in the object frame and the laboratory frame are considered as (x,y,z) and (s,r,z'), respectively.

The s-direction in the laboratory frame is aligned along the X-ray beam direction, the z-direction is aligned along the rotation axis in both frame systems, and the detector pixels' coordinates are r and z directions. By utilizing the coordinate transformation between the laboratory and object frame, the rotation can be described as follows:

$$\begin{pmatrix} x \\ y \\ z \end{pmatrix} = \begin{pmatrix} \cos\phi & -\sin\phi & 0 \\ \sin\phi & \cos\phi & 0 \\ 0 & 0 & 1 \end{pmatrix} \begin{pmatrix} s \\ r \\ z^{'} \end{pmatrix} \tag{2.22}$$

where ϕ represents the rotation angle of the sample relative to the laboratory system (see Fig. 2.11).

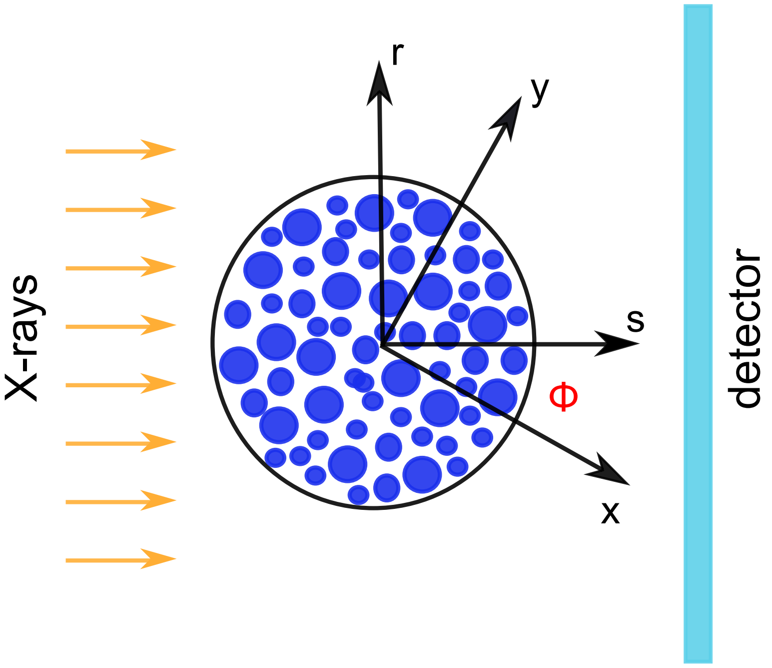

Figure 2.11: A representation of the object's (x, y, z) and beam's (s, r, z') coordinate systems.

As the rotation is along the z-direction, the $z^{'}$ is going to the z-direction and the coordinate transformation between the object frame and laboratory can be reduced for fixed z by considering only (x, y) or (s, r) plane as follows:

$$\begin{pmatrix} x \\ y \end{pmatrix} = \begin{pmatrix} \cos\phi & -\sin\phi \\ \sin\phi & \cos\phi \end{pmatrix} \begin{pmatrix} s \\ r \end{pmatrix} \tag{2.23}$$

In this way, the transformation can be reduced to a slice or section of the sample with fixed z values. By considering all slices, the 3D volume can be constructed. Based on this, the transmission T_ϕ at a given rotation angle corresponds to the following:

$$T_\phi(r) = \int p(x, y)\, ds \tag{2.24}$$

where $p(x, y, z)$ is the physical property of the sample and is equal to the attenuation in absorption tomography. For the special case of the absorption tomography with the detector positioned immediately after the object, $T_\phi(r)$ corresponds to the absolute square value of the complex transmission function in Eq. 2.21. By replacing the sample coordinates (x, y) with the beam coordinates (s, r) in the above equation, the Radon transformation is formed:

$$T_\phi(r) = \int p(x, y)\, ds = \int p(s\cos\phi - r\sin\phi, s\sin\phi + r\cos\phi)\, ds \tag{2.25}$$

The Radon transformation represents the mathematical relationship between the properties of the object being imaged and the measurements acquired by the imaging system from different angles. It is dependent on two variables (ϕ, r) and can be used to map the physical properties of objects into the projected line integral at various rotation angles. As each feature of the sample is projected on the sinusoidal curve, the measured data is called a sinogram. The sinogram is the initial data set for tomographic reconstruction and interpretation of the object.

Since the Radon transforms are linear integrals, this integral (Eq. 2.25) is transformed into a large sum because of the number of pixels of the detector, the number of voxels of the sample, and the number of rotations (given by ϕ and r).

Several methods can be used to solve this set of linear equations:

- An approach that considers the specific structure of the problem: Fourier method and filtered back projection (FBP). Both techniques are based on a direct mathematical inversion of the measured projection. Through the utilization of problem symmetry, these algorithms streamline calculations, leading to swift object evaluations.

- A variety of algebraic techniques such as Simultaneous Iterative Reconstruction Technique (SIRT), Simultaneous Algebraic Reconstruction Technique (SART), Algebraic Reconstruction Technique (ART), Conjugate Gradient (CG). They are iterative algorithms that start with an object estimate, refining it iteratively by simulating measurements, comparing these simulations with actual measurements, and updating the estimation based on the differences observed. These techniques are relatively flexible, operating without the need for symmetry, and generate objects efficiently from a few projections or missing data with fewer artifacts. However, they are slow for calculation in comparison to the Fourier method and FBP.

- Deep learning: A neural network can learn complex relationships between projection data and image features. It enables the generation of high-quality images, particularly in the case of noisy or limited data sets. It's an advanced technique to solve linear equations.

The following are detailed descriptions of the first and second reconstruction methods:

2.4.4.2 Filtered Backprojection

The FT of a projection $\tilde{T}_\phi$ for a fixed ϕ with respect to the r coordinate can be written as:

$$\tilde{T}_\phi(k_r) = \int e^{-ik_r r} \cdot T_\phi(r)\, dr \tag{2.26}$$

by considering the Eq. 2.24 and $r = -x \sin\phi + y \cos\phi$,

$$\begin{aligned}
\tilde{T}_\phi(k_r) &= \iint e^{-ik_r r} \cdot p(x,y)\, ds\, dr \\
\tilde{T}_\phi(k_r) &= \iint e^{-ik_r r} \cdot p(x,y)\, dx\, dy \\
\tilde{T}_\phi(k_r) &= \iint e^{-ik_r(-x\sin\phi + y\cos\phi)} \cdot p(x,y)\, dx\, dy \\
\tilde{T}_\phi(k_r) &= \iint e^{-i(k_r \sin\phi \cdot x + k_r \cos\phi \cdot y)} \cdot p(x,y)\, dx\, dy \\
\tilde{T}_\phi(k_r) &= \tilde{p}(-k_r \sin\phi, k_r \cos\phi)
\end{aligned} \tag{2.27}$$

This formula indicates that the FT of a single projection at a given angle of ϕ. In fact, the 1D FT of projection gives the FT of the object on a line defined by ($\mathrm{k_x}$, $\mathrm{k_y}$) = (-$\mathrm{k_r}$ $\sin\phi$, $\mathrm{k_r}$ $\cos\phi$) in the 2D Fourier space of the object, also described by the Fourier Slice Theorem. Fig. 2.12 (a) illustrates how the set of projections fills up the

Fourier space of the object on a radial array of lines.

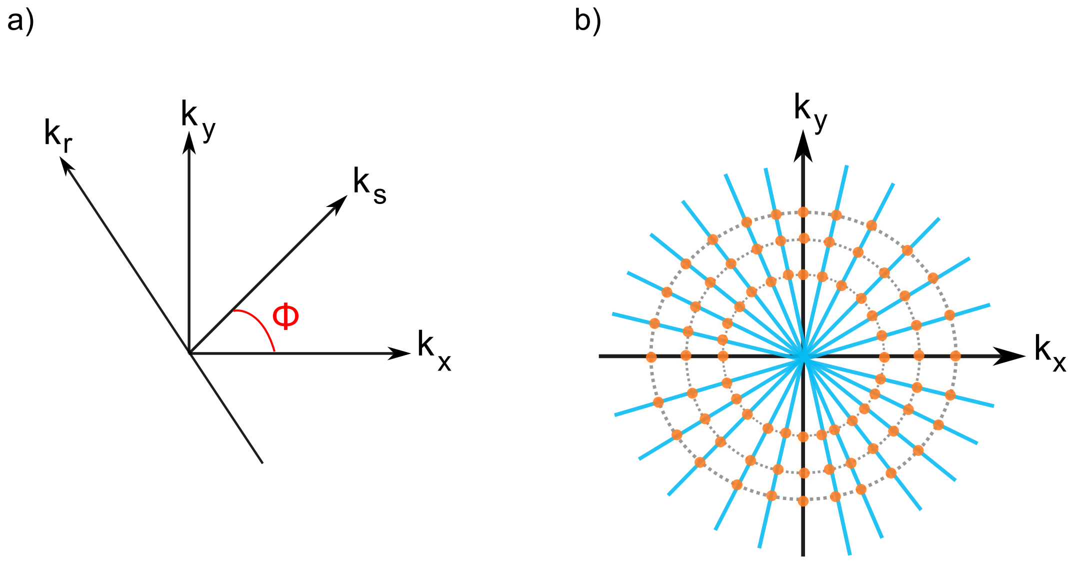

Figure 2.12: (a) Fourier space of an object (k_x, k_y) during measurement; (b) The number of measurements of multiple projections at different angles is represented by discrete orange points in Fourier space.

In the case of a few projections, the density of measured points in the Fourier space may not be sufficient to sufficiently scan the object. Hence, the optimal number of projections is required to obtain the full information about the object as follows [35]:

$$M = \frac{\pi}{2} \approx 1.5N, \tag{2.28}$$

where N is the number of pixels or the number of effective resolution elements and M is the number of rotations required. In this way, the set of the projections defined FT of the object on a radial array of lines.

Since the data is measured in polar coordinates as a function of distance k_r and angle ϕ, reconstruction of the object using the inverse FT in polar coordinates is easier and more stable in comparison to interpolation in Fourier space, which has interpolating errors. The inverse FT algorithm is known as a FBP and is a widely-used technique for image reconstruction. It reconstructs the image by utilizing the problem's symmetry.

To reconstruct the object, the object must be recalculated from its projections using inverse FT:

$$p(x,y) = \frac{1}{4\pi^2} \iint e^{i\vec{k}\vec{x}} \cdot \tilde{p}(k_x, k_y) dk_x dk_y \tag{2.29}$$

is represented in in polar coordinates, $r = -x \sin\phi + y \cos\phi$, it forms as:

$$p(x,y) = \frac{1}{4\pi^2} \int_0^{2\pi} \int_0^{\infty} e^{i\vec{k}\vec{x}} \cdot \tilde{p}(-k_r \sin\phi, k_r \cos\phi) \cdot k_r \; dk_r d\phi \tag{2.30}$$

Consideration of Eq. 2.28 allows us to rewrite the above Equation into:

$$\begin{aligned} p(x,y) &= \frac{1}{4\pi^2} \int_0^{2\pi} \int_0^{\infty} e^{i\vec{k}\vec{x}} \cdot \tilde{T}_\phi(k_r) \cdot k_r \; dk_r d\phi \\ p(x,y) &= \frac{1}{4\pi^2} \int_0^{\pi} \int_{-\infty}^{\infty} e^{ik_r r} \cdot \tilde{p}_\phi(k_r) \cdot |k_r| \; dk_r d\phi \end{aligned} \tag{2.31}$$

where $\tilde{T}_\phi$ represents the FT of projection.

Back propagation in the FBP algorithm can be performed in two steps. In the first step, the FT of each projection is filtered by multiplying with $|k|$ in the Fourier space:

$$\begin{aligned} Q_\phi(r) &= \frac{1}{4\pi^2} \int_{-\infty}^{\infty} e^{ik_r r} \cdot \tilde{T}_\phi(k) \cdot |k| dk \\ Q_\phi(r) &= \frac{1}{4\pi^2} \int_{-\infty}^{\infty} e^{ik_r r} |k| \cdot \int_{-\infty}^{\infty} e^{-ik_r r} \; \tilde{T}_\phi(r) \cdot dr dk \end{aligned} \tag{2.32}$$

In the second step, the filtered sinograms are back-projected, and the individual contributions from each projection are added:

$$\begin{aligned} p(x,y) &= \frac{1}{4\pi^2} \int_0^{\pi} e^{ik_r r} \cdot \tilde{T}_\phi(k_r). \; |k_r| dk_r d\phi \\ p(x,y) &= \int_0^{\pi} Q_\phi(r) \; d\phi \end{aligned} \tag{2.33}$$

In this way, all projections from all angles are placed at this point to assemble the whole object. Similarly, back-projected filtering is referred to as this algorithm.

2.4.4.3 Simultaneous Iterative Reconstruction Technique Algorithm

SIRT is one of the iterative algorithms. This algorithm starts by estimating the sample and then the image estimate is improved iteratively based on the differences between the measured and calculated projection data. Based on the current estimate, the algorithm simulates how the object would be imaged for each recorded projection. This algorithm consists of calculating the difference between the measured projection and the calculated projection (residual). The residual should be back-projected to all pixels that contributed to the original projection, and the estimated image can be updated by adding the back-projected residual. Each of these steps is repeated for a predetermined number of times to obtain the final estimate of the image.

In contrast to other reconstruction algorithms, SIRT updates all pixels along the line of sight of each projection simultaneously. It is important to note that although this process is time-consuming, it contributes to the maintenance of stability as well as the reduction of noise amplification in images.

SART is another iterative algorithm that updates the image estimate using a system of linear equations derived from all available projections simultaneously at each iteration [36]. The image estimate is updated by combining back projected residuals with a weighted combination. Since all projections are considered in each iteration, this algorithm is faster than SIRT.

Several open-source software packages are available for processing and analyzing tomographic data. These packages provide a variety of tools and algorithms for reconstructing 3D images from 2D projection data as well as correcting artifacts. Tomopy and Astra Toolbox are two popular packages for the reconstruction of tomographic images which are described in detail in Chapter 4.

2.5 Characterization of Heterogeneous Catalysts

Catalysts are everywhere and play a pivotal and multifaceted role in numerous aspects of science, industry, and the natural world. They are substances that enable chemical reactions to occur at faster rates by providing an alternative reaction pathway with lower activation energy. They often exhibit high selectivity, directing reactions to produce specific desired products while minimizing undesired by-products. These

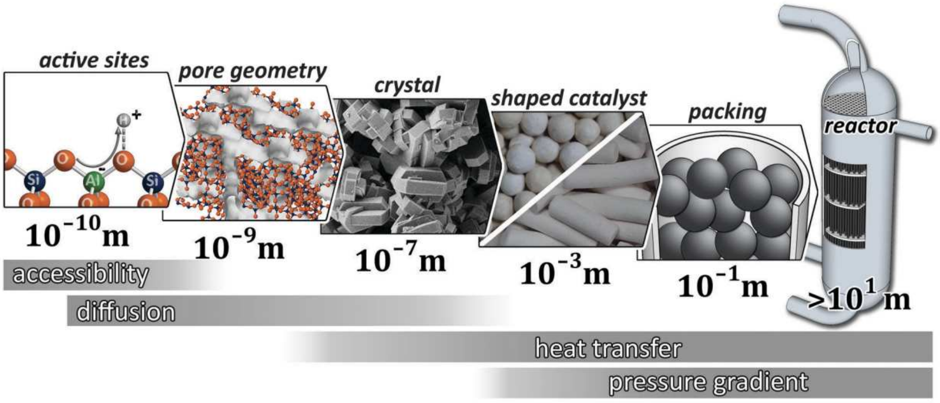

Figure 2.13: Hierarchical situation in a catalytic reactor with its different length scales.; Reprinted from Ref. [37].

properties are particularly valuable in industrial processes, where efficiency and productivity are important. They lead to cost savings in industrial processes by reducing the amount of energy required, increasing reaction efficiency, and minimizing waste.

In biological systems, enzymes serve as catalysts, accelerating biochemical reactions crucial for life. Outside the laboratories and manufacturing plants, also catalysts influence the environment by contributing to natural processes such as photosynthesis. Given the crucial role of catalysts across diverse fields, particularly in chemical reactions, the characterization of them becomes an essential tool for enhancing their performance. Due to the distinct role that catalysts play in facilitating sustainable and cost-effective chemical transformations during reactions, this thesis concentrates on studying their characterization.

Examining catalysts under ambient conditions or ex-situ conditions can provide valuable information about the structure of the active material. Therefore, it is crucial to conduct catalyst characterization under realistic conditions to identify their active sites [8]. Considering the close relationship between catalyst structure and function, in situ and operando characterization is becoming a key tool to determine the changes in the catalyst under reaction conditions during the ignition or extinction, as well as the activation or deactivation of reactions over time. This approach allows for obtaining information about the activity of the chemical reaction, including conversion and selectivity [38].

As a result of the importance of understanding the meso- and macroscopic structures of catalysts during a catalytic reaction, as well as the function of a catalyst, the study of heterogeneous catalysts requires an examination of all length scales from millimeters to atoms. Electron microscopy plays a pivotal role in the characterization of catalysts by offering high-resolution imaging down to Å and detailed structural information. Due to its restricted electron penetration depth, electron microscopy is suitable for distinguishing only thin samples, particularly effective for catalysts with nanoscale dimensions. Additionally, it has limitations in conducting in situ and operando studies.

Synchrotron radiation can overcome these challenges of electron microscopy. Hard X-rays have a variety of applications in science and technology due to their exceptional properties. Their key advantage is their high penetration depth into the matter, which allows the beam to probe samples' interiors without destroying them. It can investigate catalytic reactions that occur on the surface of materials or within bulk materials at high temperatures and pressures, in the presence of gases, as well as under various other conditions in a time-resolved manner and provides real-time information on catalytic activity [39]. Hence, it is an extremely useful tool for the spectroscopic analysis of heterogeneous catalysts.

XAS is a powerful technique employed in the examination of catalysts. It provides real-time information on catalyst mechanisms, and structural changes, including alterations in oxidation state, and the involvement of specific elements in the reaction (see Sec. 2.3). Therefore, in this research, XAS is combined with microscopic imaging. As it is possible to extract local spectroscopic information (XAS contrast) from the attenuation of the incoming X-ray by varying the incoming X-ray energy, the dynamic changes of the oxidation state of the platinum (Pt) during the partial oxidation of methane (see Chapter 5) and the oxidation state of molybdenum (Mo) during oxidative dehydrogenation of ethane (see Chapter 6) based on full-field 2D and 3D X-ray absorption microscopy were investigated.

These developed 2D and 3D X-ray imaging methods in this research offer opportunities for observing dynamic processes in catalysts under working conditions with high spatial, temporal, and energy resolution. The experimental configurations utilized in these imaging methods (see Chapter 3), along with the measurement outcomes from studying these two chemical reactions employing these techniques (see Chapters 5 and 6) will be presented in the following chapters.

3 Instrumentation

The high photon flux can enhance the sensitivity of measurements and is a crucial parameter in studying the dynamics of heterogeneous catalysis. The experiments of this research were carried out at the P64 advanced X-ray absorption spectroscopy beamline at the synchrotron radiation light source PETRA III due to its high photon flux [40]. At the beginning of this chapter, the beamline configurations, devices, and types of equipment relevant to the measurements are introduced (see Sec. 3.1). A detailed description of the operando 2D and 3D XANES imaging experimental setups are provided in Sec. 3.2.

3.1 Beamline P64 at PETRA III

PETRA (Positron-Elektron-Tandem-Ring-Anlage, "positron-electron tandem-ring accelerator") was built between 1975 and 1978 as a storage ring for high-energy physics at DESY (Deutsches Elektronen-Synchrotron) [41]. PETRA is the largest synchrotron radiation source in the world with a 2.3 km long storage ring and is operated in top-up mode with a current of 100 mA at 6 GeV. It was remodeled into PETRA III whose operation started in 2009. PETRA III is the most brilliant synchrotron radiation source in the hard X-ray regime of the third generation [42].

In spite of the fact that electron bunches in the storage ring can be refilled without dumping the entire ring and beam current fluctuations are limited to one percent, a strong asymmetry still exists between the horizontal and vertical sizes of the electron bunches which prevents the use of large amounts of the X-ray beam for scanning microscopy. The fourth-generation synchrotron source overcomes this problem by installing a lattice structure utilizing multi-bend achromats to focus the electron bunch more efficiently, thereby increasing the usable fraction of the beam by two orders of magnitude. It is intended that such a lattice structure will be installed in the PETRA storage ring by the end of this decade as the PETRA IV project at DESY [43, 44].

The beamline P64 is located at the high brightness storage ring PETRA III at the experimental hall 'Paul P. Ewald'. This beamline is designed for high photon flux XAS experiments that provides a standard method for the quantitative analysis of materials based on their constituent elements. It has the capability of performing X-ray absorption fine structure spectroscopy for highly diluted systems, quick extended X-ray absorption fine structure spectroscopy (QEXAFS) measurements on a time scale of 10 ms - 10 s, and resonant X-ray emission spectroscopy (RXES) [40]. In the following, the components of the P64 beamline will be introduced briefly and the layout of the beamline is given in Fig. 3.1. More description about the beamline can be found in Caliebe et al., [40].

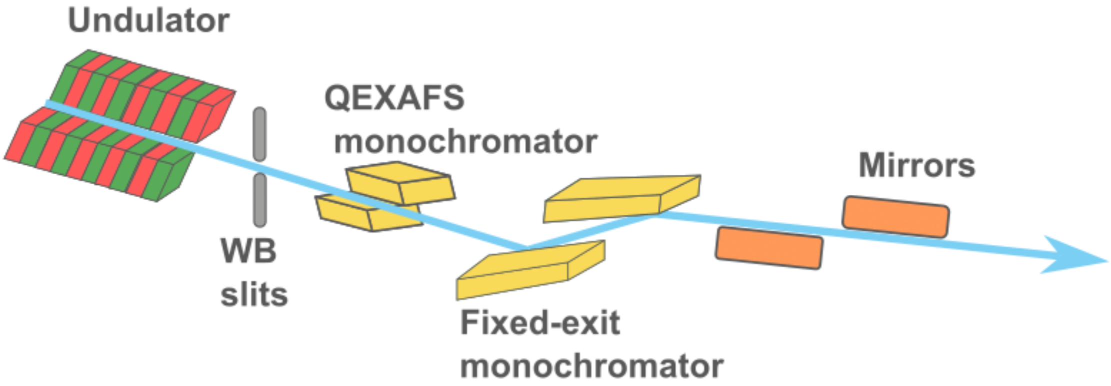

Figure 3.1: Schematic illustrating beamline P64 at PETRA III. Two different monochromators are available in this beamline to permit the performance of different measurements under different time scales with selective wavelengths.

3.1.1 Frontend

The X-ray beam is emitted by the electron beam inside the undulator. This beamline is equipped with a 58-magnetic pole undulator with a 2 m length and magnetic period of 32.8 mm. In order to minimize changes in the harmonic or intensity variations exceeding a factor of five over the range of an EXAFS-scan, the period of the undulator was selected by the overlap between the first and third harmonics.

High-power slits are mounted downstream of the source and define the beam aperture. The opening in the first vertical pair must be at least 1 mm wide, while the remaining pairs can be completely closed [45].

3.1.2 Optics Hutch

The monochromator is the first element in the optics hutch and is a critical component in a wide range of experiments. It precisely selects a narrow range of wavelengths (i.e. energies) from a broad spectrum of electromagnetic radiation. In the optics hutch of this beamline, two independent monochromators are placed for various usages: the Double-Crystal fixed-exit Monochromator (DCM) for typical energy scans in order of minutes with a fixed exit and a Channel-Cut Monochromator (CCM) for fast energy scanning with a millisecond response time and oscillation up to 50 Hz, also known as the quick-EXAFS (QEXAFS) monochromator [46]. Only this beamline in PETRA III is equipped with a QEXAFS monochromator. Further details about these monochromators are provided in the following.

3.1.2.1 Double-Crystal Monochromator

The DCM in beamline P64 is designed by Oxford Ltd and it consists of two parallel and finely polished crystals of silicon to produce a monochromatic X-ray beam [47]. The first crystal of the monochromator absorbs energy from the incoming polychromatic light and diffracts it into its component wavelengths at a specific angle based on the crystal structure and orientation. This diffraction can be described based on Bragg's law as follows:

$$n\lambda = 2d \sin\theta \tag{3.1}$$

where n is the order of diffraction, λ is the wavelength of the incident beam, d is the spacing between the crystal planes, and θ is the angle of incidence of the X-rays relative to the crystal.

The second crystal, known as the analyzer crystal, receives a selected and narrow range of wavelengths from the first crystal and diffracts them again at slightly different angles. By adjusting the angles of the incidence beam for both crystals according to Eq. 3.1, only a narrow and particular range of wavelength or energy from the incident radiation spectrum is allowed to pass through.

To produce a monochromatic beam of X-rays parallel to the incident beam, the two crystals must be positioned very precisely and parallel to each other. As the downstream part of the first crystal of the monochromator will block the beam reflected by the second crystal, a physical movement of the first crystal of the monochromator toward the beam is required to reach low energies [48]. In order to ensure thermal stability, monochromator crystals are cryogenically cooled to the temperature of liquid nitrogen.

The energy range of the monochromator can be selected by rotating both crystals and varying the Bragg angle. In DCM, Si(111) is capable of sustaining energies between 2.4 keV and 54 keV and can provide high photon flux of 10^{13} photon·s^{-1} on the sample with energy resolution of $\frac{\triangle E}{E}= 1.4 \cdot 10^{-4}$. The Si(311) is capable of sustaining energies from 4.6 keV to 103 keV with an energy resolution of $3 \cdot 10^{-5}$ and less photon flux when compared to the Si(111) [40]. This monochromator was used to generate a monochromatic X-ray beam for XANES tomography measurement of this research (see Chapter 6).

3.1.2.2 QEXAFS Monochromator

The QEXAFS monochromator enables high repetition accuracy energy scans in a fast and continuous manner by smoothly oscillating the monochromator's crystals and allowing a single spectrum to be acquired in real-time from tens of minutes to the sub-second regime [49]. Considering it has high element sensitivity, time resolution, and large penetration depth, it is an ideal technique for studying phenomena, particularly the kinetics of chemical reactions within XANES or EXAFS regions by measuring continuous cycles through a small energy region of interest [50].

This monochromator was developed by the group of Prof. Dr. Frahm at the University of Wuppertal. One of these QEXAFS monochromators is located at the Super XAS beamline at the Swiss Light Source (SLS) and the other at beamline P64 at PETRA III. Considering the goal of this thesis is to perform high spatial and temporal measurements of chemical reactions, I have chosen the beamline P64 at PETRA III which is equipped with the QEXAFS monochromator. Fig. 3.2 illustrates the QEXAFS monochromator installed at the optics hutch of this beamline and the following is a brief description of this monochromator [51].

The monochromator is mounted on CAMdrive tilt tables in order to achieve rapid angular oscillations and is housed in a vacuum tank with an 800 mm inner diameter [46]. The oscillating water-cooled direct drive torque motor (Siemens SIMOTICS 1FW6) is installed coaxially inside of the goniometer, as shown in Fig. 3.2, and connected to the crystal stage which is located inside the larger goniometer by a fixed axis.

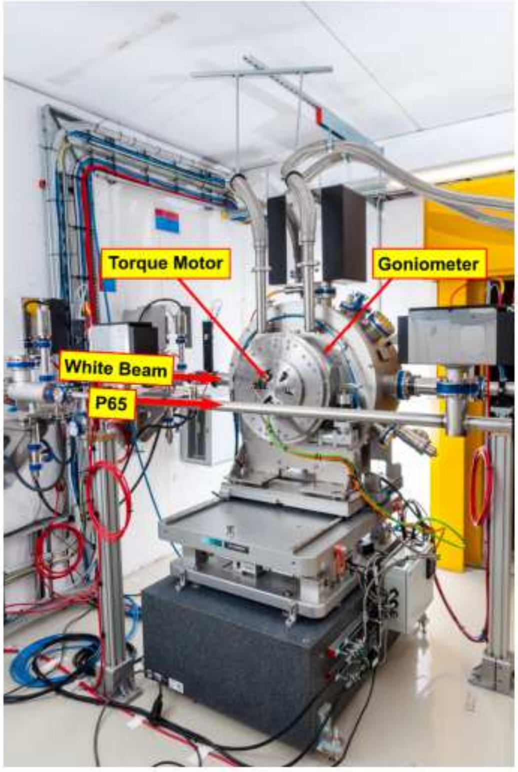

Figure 3.2: QEXAFS monochromators are installed in the optics hutches of beamlines P64 and P65; Reprinted from Ref. [51].

The crystal stage is mounted directly to the axis which is connected to the rotor of the torque motor and is stabilized by ball bearings which are shown in Fig. 3.3.

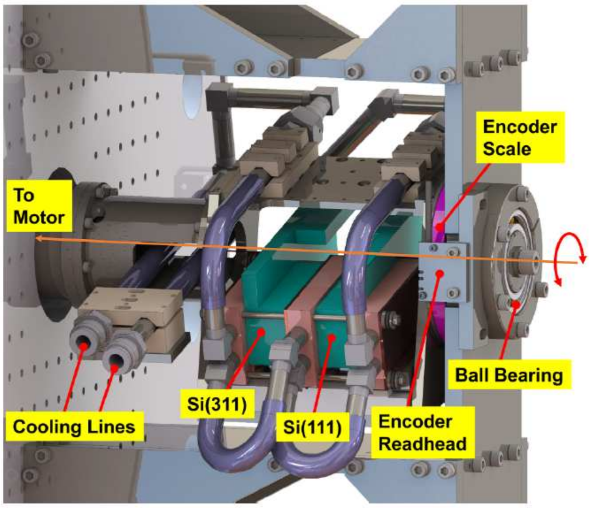

Figure 3.3: Schematic of the crystal stage of the QEXAFS monochromator with two-channel cut crystals; Reprinted from Ref. [49], with the permission of AIP Publishing.

It consists of monochromator crystals, the crystal cooling unit, and the angular encoder scales [49]. To increase the range of energy accessible to X-rays, two different orientations of the channel-cut crystals, Si(111) and Si(311), are mounted side by side on the same Bragg axis at this stage. The Si(111) can provide photon energies between 4.0 keV and 22.7 keV and the Si(311) can cover between 7.6 keV to 43.4 keV with a vertical beam size of 1 mm [49]. A combination of these two crystals in the QEXAFS enabled us to obtain the monochromatic beam with an energy range from 4.0 keV to 32.0 keV [46]. By moving the vacuum chamber horizontally, perpendicular to the incident beam, the crystal can be selected [50]. On the side of the crystal stage, there is a circular scale and a rigid frame, mounted on the side wall of the vacuum chamber and holds the read head.

Torque motors of the monochromator have rotors that can rotate freely, but their stator is constrained by the goniometer's rotational stage. Consequently, the torque motor's reference frame rotates as well with the rotation of the goniometer. Both the goniometer and the torque motor are located on the atmospheric side of the monochromator vacuum chamber and both rotations are fed independently of one another [46]. The rotor drives oscillatory movements of the crystal stage with a given amplitude and frequency and is able to limit the amplitude of the direct-drive motor too. The goniometer facilitates precise alignment of the center angle of the oscillation and is able to adjust the mean Bragg angle (θ_0). Therefore, the movement of the crystal stage (θ_{Bragg}) is determined as follows [51]:

$$\theta_{Bragg} = \theta_0 + \theta_{Osc}(t), \tag{3.2}$$

where $\theta_{\mathrm{Osc}}(t)$ is the time-dependent oscillatory angle and is coupled to the movement of the crystal. As the amplitude and the center position of the crystal oscillation determines the Bragg angle, the range of Bragg angles in the QEXAFS monochromator is between 5° to 30°. In this monochromator, a wide range of oscillation frequencies can be achieved from 0.01 Hz to 100 Hz with a maximum amplitude of 4° that is limited by the torque provided by the motor at high frequencies [51]. Due to the sinusoidal oscillation and the recording of two spectra within an oscillation period (one cycle), one with increasing and one with decreasing energy, the acquisition rate of absorption spectra is double that of mechanical oscillations frequency and the spectra are referred to as "up" or "down" according to the direction of the scan [49].

Since Bragg angles define the energy scale of each spectrum, it is of critical importance in QEXAFS experiments to measure the precise Bragg angles of the crystals in real-time. The optical angular encoder, located within the monochromator near the crystals, is able to determine the total Bragg angle with respect to the vacuum chamber and enhances the accuracy of QEXAFS measurements by measuring mechanical deformation [49]. It is important to note that the mechanical stability of the monochromator (a time frame for each data point), the response times of the detectors, the photon flux available, and the data acquisition system are all factors that limit QEXAFS' capacity for achieving a high temporal resolution. This monochromator was used in the rapid 2D XANES imaging measurement (see Chapter 5).

3.1.2.3 Mirrors

Two Si-mirrors, as shown in Fig. 3.1, were installed downstream of the monochromator at this beamline to provide a low-pass filter for reducing or rejecting higher harmonic frequencies.

Depending on the range of X-ray energy, three different coatings have been designed for these mirrors to reflect only the fundamental wavelength of X-ray energy. Mirror with only silicon coating can be used for lower energy ranges, with rhodium coating for intermediate energy ranges, and platinum coating for higher energy ranges [40].

Additionally, these mirrors have the capability of focusing the beam horizontally and vertically. In order to achieve horizontal focus, two grooves of varying radii are machined into the first mirror. This allows the beam to concentrate in the energy range of 2.4 keV to 22 keV horizontally. For vertical focusing over the entire range of energies, the second mirror can be bent. In this way, a focal beam size down to 50 µm (v) × 150 µm (h) can be achieved [46]. These mirrors are described in more detail in Caliebe et al., [40].

3.1.3 Experimental Hutch

In the experimental hutch, the monochromatic photon flux of the 10^{12} to 10^{13} photons per second is available with the beam size of 1 mm × 1 mm on the sample. Ion chambers are used as standard detectors in this beamline to measure the intensity of the incident and transmitted flux on the sample. In addition to the ion chambers, other detectors available at this beamline provide the ability to study a wide range of samples, including highly diluted, thick, and low-concentration samples [45]. Despite the presence of these detectors on this beamline, I used a high-resolution X-ray detector for my XANES imaging measurements, which will be discussed in more detail in the following.

3.1.3.1 Detector

In order to obtain a high spatial and temporal resolution, the sequences of two-dimensional images as a function of time were recorded during measurements using a high-resolution two-dimensional X-ray imaging instrument. The high-resolution detector shown in Fig. 3.4 consists of the high-resolution X-ray microscope (Optique-Peter microscope) optic coupled to an sCMOS camera (PCO.Edge 4.2 CLHS). It operates by converting the visible light from the X-ray scintillator screen of the microscope into electronic signals on the camera in order to visualize the X-ray light intensity distribution. The following is a more detailed description of these instruments.

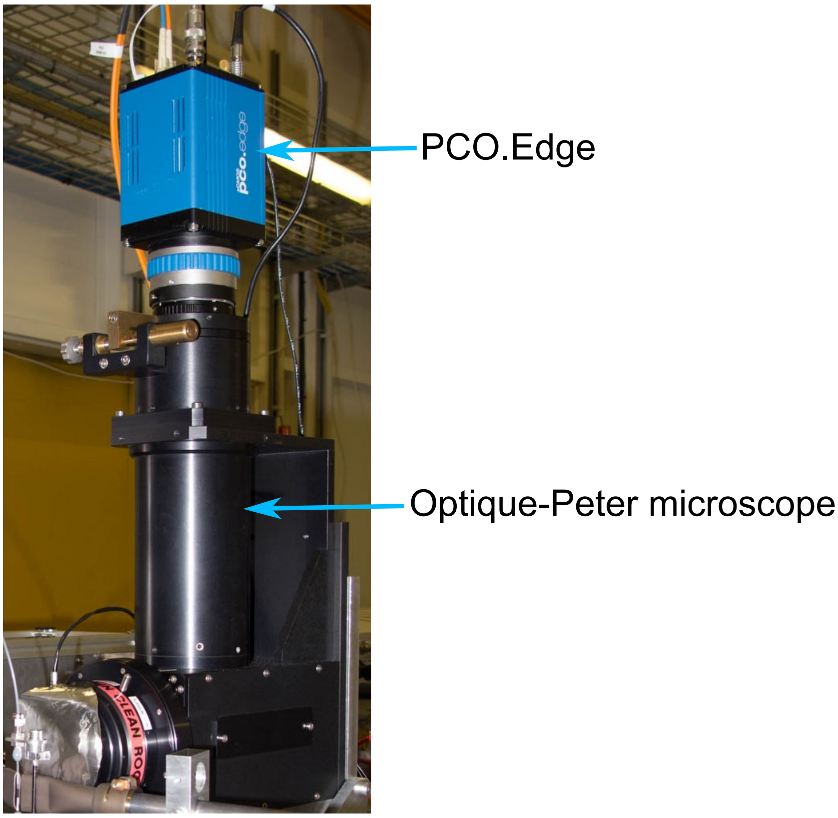

Figure 3.4: The high-resolution X-ray microscope was combined with the PCO.Edge 4.2 CLHS camera as the X-ray detector during measurements.

High Resolution X-ray Microscope

The high-resolution X-ray imaging microscope includes a scintillator, multiple motorized objective lenses, a bending mirror, and a tube lens. To enhance the spatial resolution of recorded images, this microscope is based on a tandem lens configuration. First, the scintillator converts the incoming X-ray intensity into visible light. After that, a divergent beam of light from the scintillator is magnified and converted into a parallel beam by the first lens (objective lens). The bending mirror, which is positioned after the objective lens, reflects light vertically and the second lens, known as a tube lens, focuses a parallel beam upon the image plane (camera). A scintillator and triple objective lenses of the microscope are shown in Fig. 3.5.

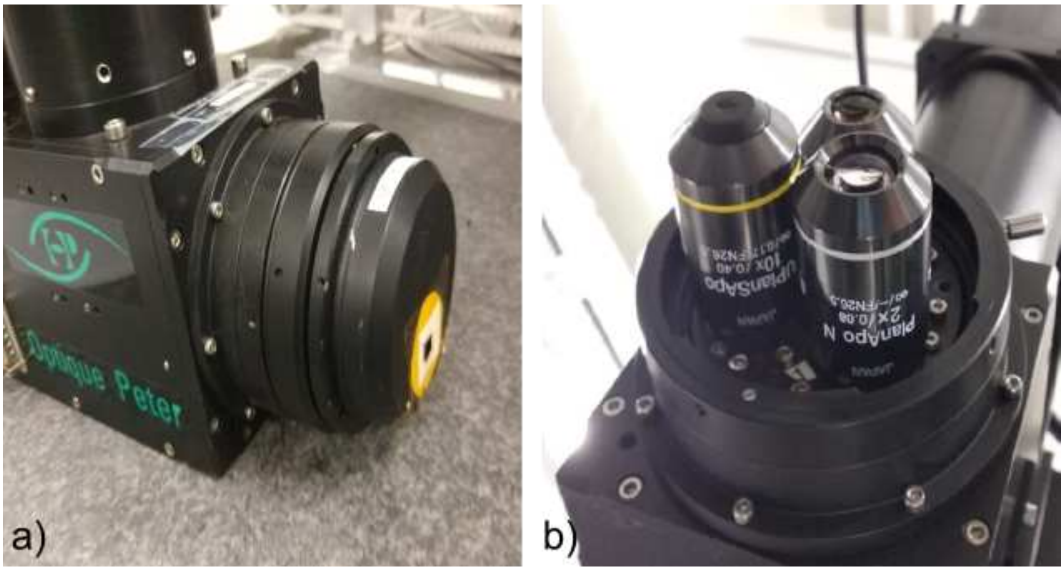

Figure 3.5: (a) The non-tiltable scintillator of a high-resolution X-ray microscope made from LAG crystal with a thickness of 180 µm; (b) Multiple objective lenses with different magnification factors are located on a motorized nosepiece of the microscope.

An objective lens' magnification power is determined by its focal length and the distance from the scintillator. The information regarding these triple-objective lenses such as numerical aperture (NA), working distance (WD), and effective magnification (EM) are available in Table 3.1.

To improve the spatial resolution of the recorded 2D images in the second experiment of this research, a high-resolution X-ray microscope has been refurbished. Consequently, the LAG crystal scintillator has been replaced with triple scintillators and the scintillator mount has been upgraded to a motorized mount to accommodate these triple scintillators. According to Fig. 3.6, these scintillators are tiltable and

Objective lens	**NA**	**WD** (mm)	**Resolution limit** (µm)	**EM**
2×	0.08	6.2	3.44	5×
4×	0.16	13	1.72	10×
10×	0.40	3.1	0.69	25×

Table 3.1: Parameters of triple objective lenses of the high-resolution X-ray microscope.

made from different materials with varying thicknesses.

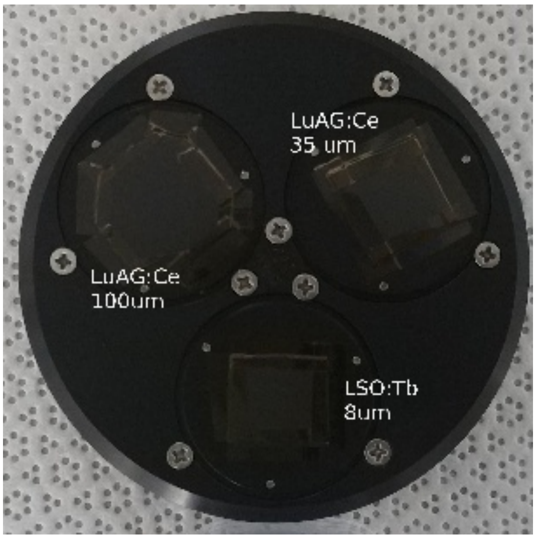

Figure 3.6: Rotatable scintillator mount on the high-resolution X-ray microscope with three slots. Scintillators are covered with 75 µm thick black kapton.

The summary of the materials and thickness of them are provided in Table 3.2.

Material	**Thickness** (µm)	**Dimension** (mm)
LSO:Tb on 170 µm YbSO	8	8 × 8
LuAG:Ce	35	8 × 8
LuAG:Ce	100	15 × 15

Table 3.2: Parameters of triple tiltable scintillators mounted on the high-resolution X-ray microscope.

A scintillator's thickness has a direct impact on the resolution of imaging. Thicker scintillators may capture a higher percentage of incident radiation, which may increase detection efficiency. The spatial resolution of the optical microscope is limited by NA, which determines the depth of focus. As the depth of field must cover the thickness of the scintillator, the resulting NA limits the spatial resolution.

Higher spatial resolution and lower signal-to-noise ratio can be obtained in recorded images by using thinner period scintillators. The thinner scintillator can be imaged sharply by an objective with a higher NA, thus yielding higher resolution. However, this comes at the cost of reduced detection efficiency with a thinner scintillator.

In general, selecting the appropriate scintillator thickness and an objective lens for each measurement requires consideration of a number of factors, including specimen type, magnification level, and field of view, as well as spatial resolution and testing them.

PCO.Edge 4.2 CLHS Camera

PCO.Edge 4.2 CLHS camera is based on scientific Complementary Metal-Oxide-Semiconductor (sCMOS) sensor technology. This camera has the capability of capturing images at very high frame rates between 35 to 100 frames per second (fps), enabling it to record dynamic processes that occur very rapidly. If the X-ray photon statistics are poor, the signal-to-noise ratio is too low (0.8 median electrons), potentially leading to the acquisition of low-quality images. In comparison to other cameras, this camera is able to convert 82 % of incident light into detectable electrons, which indicates a high quantum efficiency.

In order to minimize noise and increase sensitivity, PCO.Edge cameras are equipped with a cooling system that maintains a low temperature during operation. There are several trigger options available for this camera, including external triggers, software triggers, and hardware triggers, making it an ideal tool for time-resolved imaging with low readout noise and high sensitivity. The resolution of the PCO.Edge camera is 2048 × 2048 pixels with a pixel size of 6.5 µm × 6.5 µm and a field of view (FOV) of 13.3 mm × 13.3 mm. The exposure time of the camera is adjustable between 100 µs and 10 s and the camera is capable of capturing images at up to 100 fps at full resolution.

This camera is specifically designed for scientific applications that require high sensitivity, high dynamic range, low noise, fast frame rates, and simultaneous reading of all pixels. Due to these specific characteristics, this camera was combined with the high-resolution X-ray microscope and used in the experiments. Detailed information regarding the features and parameters of the camera for each measurement is provided in Sec. 3.2.

3.1.3.2 Gas Analysis

A gas analysis technique is an important component of catalysis studies that involves identifying and quantifying various reactant and product gases present during the chemical reaction. Several analytical techniques are employed to analyze gas samples, including Gas Chromatography (GC), Mass Spectrometry (MS), Infrared Spectroscopy, Electrochemical Sensors, and Optical Sensors. The feature of the chemical system under consideration plays a key role in selecting the appropriate gas analysis technique. Here, I present a brief overview of two of the most commonly used gas analysis techniques, MS and GC. These techniques have been utilized in the experiments of this research.

Mass Spectrometry

MS is a method of analyzing the composition of gases to determine the molecular mass and structure of samples, especially useful to identify unknown substances or quantify the individual components in complex mixtures. This method identifies and separates the chemical substances based on their mass-to-charge ratio ($\frac{m}{z}$) and abundance. Since this technique delivers faster data acquisition and greater flexibility compared to other gas analysis methods, it is an ideal method for studying time-resolved measurements.

MS, in general, consists of three components: the ionization chamber, the analyzer, and the detector. I briefly describe these components here. In the first step, the incoming gas flow is ionized into charged particles (ions) with a characteristic mass m and charge z by various ionization methods, such as electron ionization or photoionization inside the ionization chamber.

Afterwards, a mass analyzer applies an electric or magnetic field to the ions in order to separate them from the sample stream. The MS with quadrupole analyzers accelerates ions with the electric field and allows them to travel through four parallel rod electrodes that are located at the corners of a square and known as the quadrupole assembly. Since there is a direct voltage potential and a high-frequency alternating voltage between adjacent poles, it is possible to sort the ions according to their mass-to-charge ratio and bring ions of a defined mass to the detector on a stable trajectory by varying the frequency of the poles.

Finally, ions follow different trajectories depending on their mass-to-charge ratio, and ions of a defined mass can strike a detector and generate an electrical signal proportional to the number of ions detected. This signal provides information about the abundance of ions at different mass-to-charge ratios. A data acquisition system processes the electrical signal generated by the detector which is known as a mass spectrum, a plot of ion abundance versus mass-to-charge ratio. In this profile, different peaks correspond to specific ions with a specific mass-to-charge ratio, and their relative intensities indicate the relative abundance of each ion. Comparison of measured mass spectra with known mass spectrum databases (such as NIST's Mass Spectral Library) can facilitate the identification and quantification of compounds within samples.

Since the MS system is unable to separate gaseous ions with the same mass-to-charge ratio, e.g. CO (28) and N_2 (28), numerous techniques and strategies, such as high-resolution MS, may be employed to overcome this limitation and provide more detailed information regarding the compounds to be analyzed.

Gas Chromatography

GC is a sophisticated technique used to separate, identify, and analyze liquids or gases. It is based on partitioning a sample mixture into two phases: a stationary phase and a mobile phase which allows the separation of individual components based on the relative affinity of each component to each phase. GC process can be classified into different categories based on the operating principle, the type and dimensionality of the column, the type of detector used in it, the stationary phase, and the modulation technique. In the GC used in this study, the mobile phase is a gas and the stationary phase is a solid. The following is a brief explanation of the basic aspects associated with this type of GC.

In order to transport analytes through columns in GC, helium or argon gases are used as the mobile phase. Solid materials with high surface areas and specific adsorption properties serve as substrates for the interaction of analyte components and the separation of sample components based on their adsorption properties.

The most common type of column is the capillary column. The capillary column is an open, long tube made from a fused silica. In this type of reactor, the stationary phase is immobilized inside the inner capillary tube walls or supported on solid inert packing. Porous Layer Open Tubular (PLOT) capillary columns used in this research contain a porous layer of solid material (e.g., alumina, molecular sieves, Porapak) attached to their inner wall that serves as an adsorbent. During the passage of the gas sample components through this packed column, different interactions between the components with a stationary phase lead to the actual separation process.

Depending on the chemical properties of the analytical sample, such as molecular size, polarity, and functional group, the affinity for the solid support and each component's retention time on the column will vary. Consequently, components with a stronger affinity for the solid phase will be retained longer in the column, resulting in a longer retention time, while components with weaker affinity will be less retained and eluted sooner. In this way, the light hydrocarbons, CO_2, and H_2O can be distinguished based on their polarity, as well as permanent gases based on their size.

In order to measure the separated components eluted from the column, a detector is used. At a certain retention time, the detector generates a signal (peak area, intensity) proportional to the species's concentration. Several hardware and software components make up the data system and are responsible for capturing and processing the detector signals to generate a chromatogram. From this chromatogram, information regarding the retention time and peak characteristics of the separated components can be derived, and the identification and quantification of reactants and products during the reaction can be done.

3.2 Experimental Setup at Beamline P64

This research consists of two measurements, one involving the rapid full-field 2D-XANES imaging of catalytic partial oxidation (CPO) of methane (see Chapter 5) and the other involving the rapid full-field tomography imaging of oxidative dehydrogenation (ODH) of ethane (see Chapter 6) at the beamline P64, PETRA III.

In both measurements, the XANES technique was combined with full-field X-ray imaging (see Sec. 2.4.1). This configuration enables to measure 2D images of a large section of the catalyst bed, enabling a comprehensive and detailed view of the spatial distribution and performance of the catalyst within the reactor. Also, high-resolution detectors used in these experimental setups provide higher signal-to-noise ratios due to their high photon sensitivity. A description of the experimental setups used in these measurements is provided in the following.

3.2.1 Operando 2D XANES-Imaging Setup[1]

High monochromatic photon flux and the availability of the QEXAFS monochromator at P64 make this beamline especially suitable for studying time-resolved phenomena. A scheme of the experimental operando 2D XANES-imaging measurement is illustrated in Fig. 3.7. This setup involves the quartz capillary, mass flow controller, MS, and high-resolution X-ray camera. The following is a more detailed description of them.

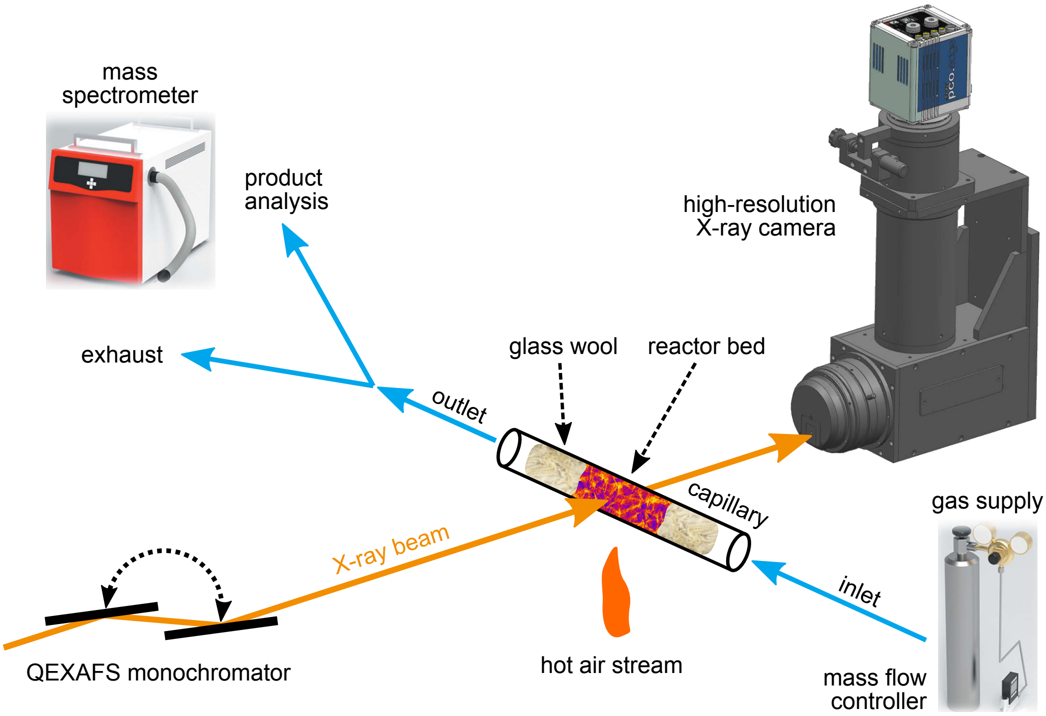

Figure 3.7: An illustration of the operando 2D XANES imaging. The 2.2 wt% Pt/Al_2O_3 embedded in a quartz capillary and a high-resolution X-ray camera imaged the capillary at a fast sequence of different energies around Pt L_3 edge X-ray absorption edge; Reprinted from Ref. [12].

In order to study the dynamic changes of Pt catalyst during the CPO of methane to synthesis gas (see Sec. 5.2), the catalyst material supported on Al_2O_3 was placed in a quartz capillary, a detailed description of the catalytic data is provided in Sec. 5.3.1. To align the capillary vertically and horizontally with the X-ray beam, it was mounted on a stack of motor stages.

A gas mixture of CH_4, O_2 and He was provided as reactants that flowed from the reactor's inlet towards the outlet. Several mass flow controllers (El-Flow, Bronkhorst,

---

[1] Parts of the text and figures in this section were adapted and reprinted from [12].

The Netherlands) were utilized to adjust the appropriate gas flow rate and to deliver the gas mixture into the reactor in order to control the chemical state of the catalyst by adjusting the gas flow through the capillary. Detailed information about the gas composition and flow rate is provided in Sec. 5.3.2.

A pair of hot air blowers (LE Mini, Leister AG, Switzerland) were mounted below the capillary in order to provide heat for this reaction, and the temperature of the capillary was calibrated in advance using a portable thermometer, a type K thermocouple. The thermocouple was positioned very close to the catalyst bed position in order to measure the differences in temperature between the capillary temperature and the temperature from the built-in thermocouples of the gas blowers. In Fig. 3.8, the separate Eurotherm controller for gas blowers and the mass flow controller are illustrated.

Figure 3.8: The mass flow controller, the upper device, regulates the flow rate of gas. The Eurotherm controller, which is located at the bottom of the mass flow controller, can be used to control the temperature of each gas blower.

The reaction products were analyzed online via MS (OmniStar GSD 320 O, Pfeiffer Vacuum, Germany) connected to the outlet of the catalytic reactor. This MS was provided and operated by the group of Prof. Dr. Grunwaldt at the Karlsruher Institut für Technologie (KIT). The setup was checked for leaks before the experiment began in order to ensure the gas tightness of the system.

The high-resolution X-ray camera described in Sec. 3.1.3.1 was used in the operando 2D XANES imaging for recording the 2D images, Fig. 3.9. The three objective lenses of the microscope in combination with the scintillator were tested prior to the measurement. Finally, the 4× objective is used in combination with the 2.5× ocular for recording high-resolution 2D images. In this way, the imaged area was magnified by a factor of 10 and the effective pixel size in recorded images was $p_{\mathrm{eff}} = 0.65\,\mu\mathrm{m}$, based on a camera pixel size of p = 6.5 µm. As the total FOV was 1.33 mm × 1.33 mm, each recorded image contains approximately 4 million resolution elements.

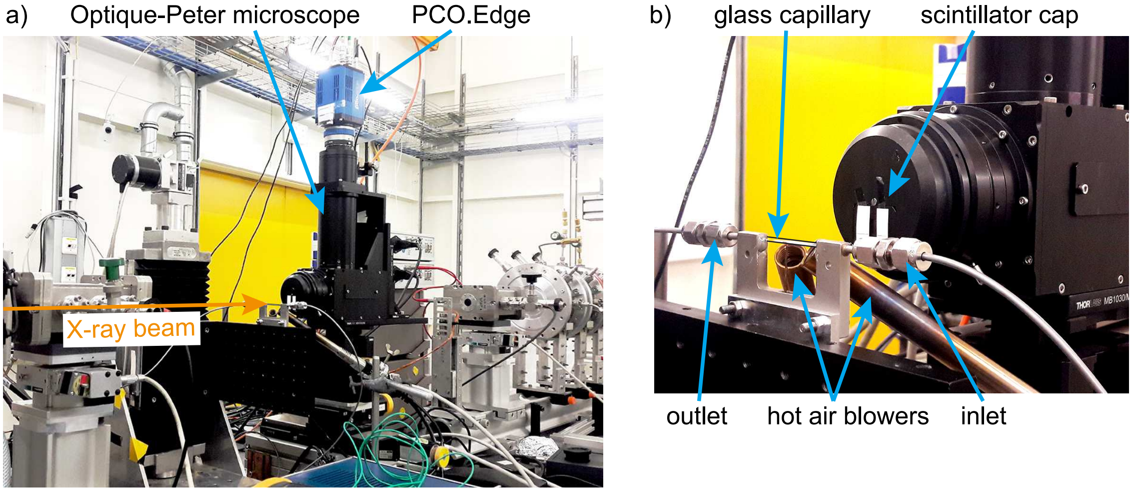

Figure 3.9: Imaging setup installed at beamline P64 for 2D XANES imaging: (a) The high-resolution X-ray microscope in combination with the PCO.Edge 4.2 CLHS camera were recorded the high-resolution 2D images; (b) In this experiment, two hot air blowers were used to heat the reactor bed embedded in the glass capillary. With thermocouple installed on the air blowers' nozzles, the temperature was measured. Reactants flow from the inlet (on the right) towards the outlet (on the left) of the catalytic reactor; Reprinted from Ref. [12].

3.2.2 Operando Tomography XANES-Imaging Setup

I extended the previous technique into a rapid operando XANES tomography with spatial-, energy- and time resolution at P64 beamline. In Fig. 3.10 the main parts of the experimental setup installed at P64 are shown, including the aRCTIC sample environment, mass flow controller, GC, and high-resolution X-ray camera.

To investigate the dynamic changes of the Mo catalyst during the ODH of ethane to ethylene (see Sec. 6.2) in this experiment, the Mo catalyst supported on Al_2O_3 was placed within a quartz capillary. The catalytic data is described in more detail in Sec. 6.3.1.

Tomography imaging was performed using the aRCTIC sample environment which is responsible for the rotation of the reactor. This operating tomography setup was

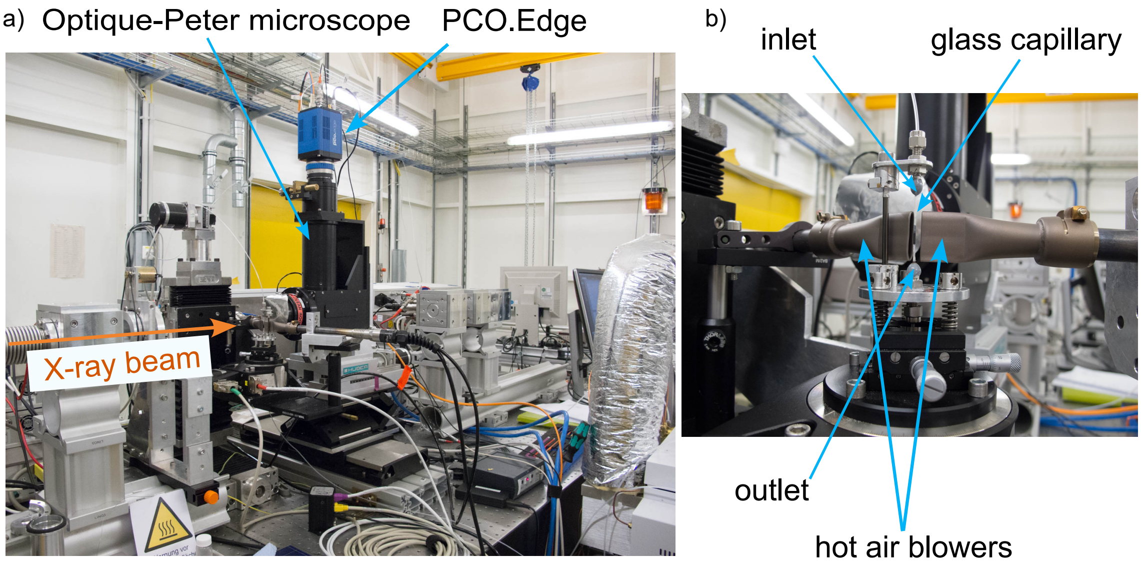

Figure 3.10: Imaging setup installed at beamline P64 for operando tomography XANES imaging: (a) The high-resolution X-ray microscope in combination with the PCO.Edge 4.2 CLHS camera; (b) The reactor bed embedded in the glass capillary was mounted on the sample unit of the aRCTIC setup and was heated by two hot air blowers. Reactants flow from the inlet (on the top) towards the outlet (on the bottom) of the catalytic reactor.

designed and developed by the group of Dr. Sheppard and Prof. Dr. Grunwaldt at KIT and has been tested at the European Synchrotron Radiation Facility (ESRF), Paul Scherrer Institut (PSI), and PETRA III facilities [7, 52].

This aRCTIC setup consists of the sample unit, the alignment stage, and the rotation motor, as shown in Fig. 3.11. A glassy carbon stabilizing rod (5 mm diameter, Alfa Aesar, Germany) is mounted on the alignment stage and connects the bottom and top plate of the sample unit [52]. A full reactor with catalyst particles was glued and fixed on a sample unit and mounted perpendicularly to the X-ray beam direction. It is important to note that the stabilizing rod is responsible for taking on the load from the capillary. Due to the tiltability of the sample unit and its function as a goniometer, the sample can be aligned vertically with respect to the rotation center. The alignment stage which enables the sample to be positioned in the middle of the rotation stage by translating it in the horizontal and vertical direction to the X-ray beam. There is a passage in the middle of the rotation and alignment stages where flexible gas tubing can pass and be connected to the sample unit [13].

A gas mixture of C_2H_6, O_2 and N_2 was provided as reactants and the mass flow controllers used in the previous measurement adjusted the gas flow rate and delivered

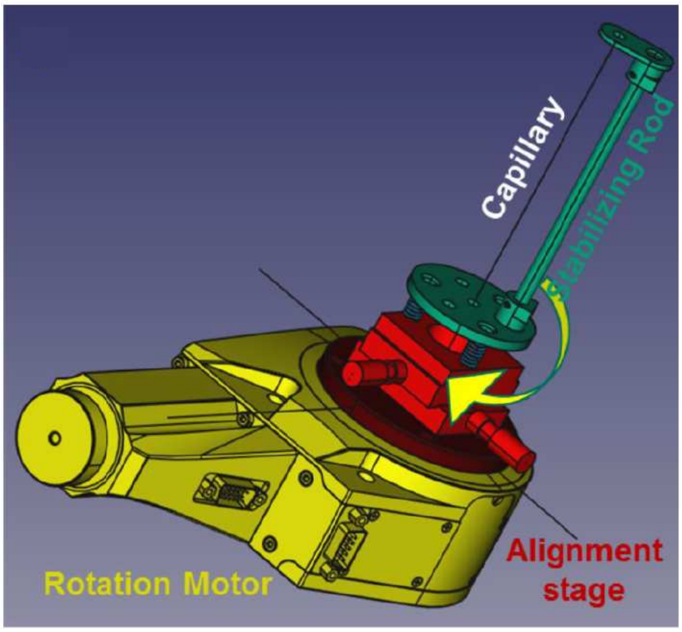

Figure 3.11: CAD drawing of the aRCTIC setup; Reprinted from Ref. [52].

the reactants inside of the reactor. The gas composition and flow rate are discussed in detail in Sec. 6.3.2.

The two hot air blowers were adjusted to the sample height in order to ensure that the heat was evenly distributed throughout the sample. The temperature of each of these hot air blowers was controlled by a separate Eurotherm controller. By adjusting the flow rate of gases through the capillary and temperature with two hot air blowers, the chemical state of the catalyst was controlled and studied under different reaction conditions.

In order to analyze the composition of the reaction products online, GC (Agilent 7890B, United States) was connected to the outlet of the catalytic reactor. It was provided and operated by a group of Prof. Dr. Horn at the Technical University of Hamburg (TUHH) for this measurement and shown in Fig. 3.12.

Similar to the operando 2D XANES imaging measurement, the high-resolution X-ray camera was used in this experiment. However, as mentioned previously (see Sec. 3.1.3.1), the X-ray microscope was refurbished for this measurement and the scintillator was replaced with triple scintillators. Consequently, three objective lenses of the microscope in combination with the triple scintillators were tested before the measurement, and the resolution and magnification of recorded 2D images were assessed. As a result, the Lutetium Aluminium Garnet (LuAG:Ce) scintillator with a thickness of 35 µm in combination with a 4× objective lens recorded high-resolution

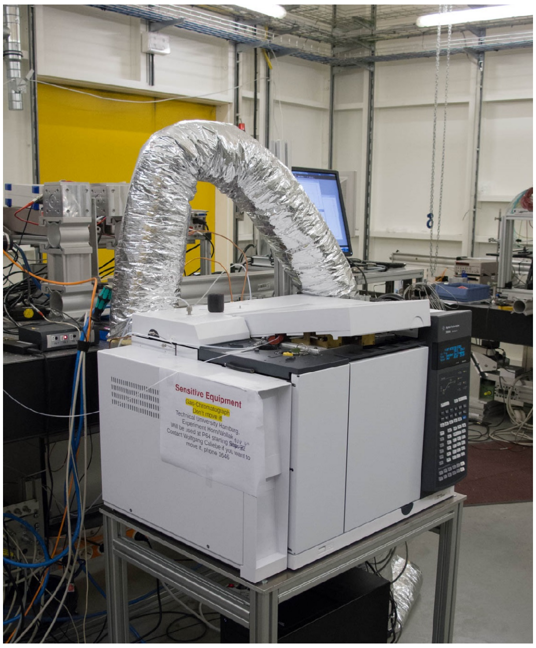

Figure 3.12: GC was used to separate and analyze the chemical components of the sample online in the XANES tomography imaging measurement of this work.

projection images compared to the other scintillators and objective lenses of the microscope. With this combination, the recorded image area was magnified by a factor of 10 with an effective pixel size of $p_{\mathrm{eff}} = 0.65\,\mu\mathrm{m}$ and a total FOV of $1.33\,\mathrm{mm} \times 1.33\,\mathrm{mm}$.

4 Data Analysis

Since the large volume of data was recorded in 2D XANES imaging of the CPO of methane to synthesis gas (see Chapter 5) and 3D XANES imaging of the ODH of ethane to ethylene (see Chapter 6) with the energy- and time-resolution, I have developed an optimized pipeline for evaluating data. Descriptions of the data acquisition methods, as well as the methods of sorting and processing the data in each measurement are provided in Sec. 4.1 and Sec. 4.2 of this chapter.

4.1 Full-Field 2D XANES Imaging[1]

In heterogeneous catalysis, many processes and materials undergo dynamic structural changes depending on their chemical environment. In order to monitor such dynamic changes, conventional spectroscopic characterization tools can be challenging, due to the high time resolution required. In this study, the custom sample environment was installed at the beamline P64 (see Fig. 3.9) and the fast QEXAFS monochromator at this beamline was coupled to a high-resolution X-ray camera (PCO.Edge 4.2 CLHS) to perform rapid spectroscopic 2D imaging of the chemical state of a Pt/Al_2O_3 catalyst during partial oxidation of methane to synthesis gas with chemical contrast over individual pixels. The experimental procedures and data analysis of this technique are based on Ref. [12] and are discussed in greater detail in the following.

4.1.1 Data Sorting

Here, the QEXAFS monochromator was operated independently from the rest of the setup and continuously oscillated around the Pt L_3 absorption edge at a frequency of 0.18 Hz. In this way, the time period to record a single up or down sweep of the QEXAFS monochromator over Pt L_3 absorption edge was 2.8 s. In this configuration, the high-resolution X-ray camera (see Fig. 3.4) was operated at a 50 Hz full-frame

---

[1] Parts of the text in this section were adapted and reprinted from [12].

rate, and a 2D transmission image was captured with it at the same time as the encoder value of the monochromator was recorded into the file [12].

According to Sec. 3.1.2.2, the angular position of the monochromator can be measured by an incremental encoder. Since Bragg's law is associated with angular position, the X-ray energy can be calculated as follows:

$$E = \hbar\nu = \frac{\hbar c}{\lambda} \tag{4.1}$$

$$n\lambda = 2d\sin\theta \tag{4.2}$$

$$E = \frac{\hbar c}{2d\sin\theta} \tag{4.3}$$

where $\hbar$, ν, c, and d are the Planck constant, frequency, the speed of the light, and the lattice spacing, respectively. By converting the recorded encoder value into energy with this equation, the energy corresponding to each image was calculated. The schematic of the recorded encoder's values of the monochromator is shown in Fig. 4.1.

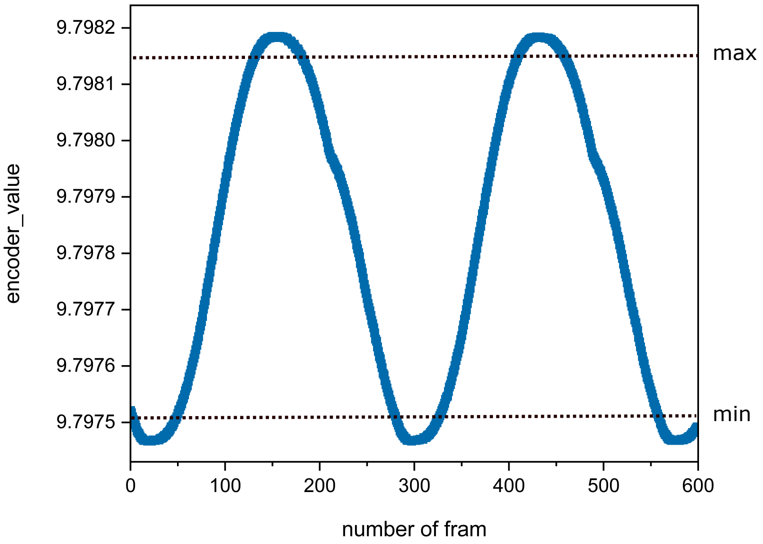

Figure 4.1: Profile of encoder values for the QEXAFS monochromator. In the data analysis, encoder values in the range between the maximum and minimum were taken into account.

The data was collected in chunks of 100 scan points. In this figure, the encoder values for the six chunks, and both maximum and minimum values are shown. In data processing, the maximum and minimum encoder values were defined in the Python script to limit the X-ray energy range. As 10 % of all images were measured at the highest and lowest energy values in comparison to the defined range, these images were removed and were not considered in the data analysis. Thus, a full stack of about 80 XANES transmission images around the absorption edge of the catalyst was recorded in a total time of 1.6 s [12].

4.1.2 Dark- and Flat-Field-Corrected 2D Absorption Image

A sequence of images was captured with the beam shutter closed in order to account for the constant signal background specific to the camera. In this case, about 500 frames were recorded at 50 Hz, i.e. about 10 s total exposure time, and then averaged to produce a representative dark-field image. This image has been subtracted from the all sorted flat-field and transmission images and all negative pixels were replaced with zero values. This process is known as dark-field correction.

At each temperature after thermally stabilizing the catalyst bed, the capillary was moved out of the X-ray beam, and the intensity of the incoming X-ray beam I_0(E, x, y) was taken into account. These so-called flat-field images were recorded with continuously oscillating monochromators and a total exposure time of 200 s at 50 Hz, corresponding to approximately 10000 single frames.

As the QEXAFS monochromator and high-resolution camera were operated independently, the encoder value of the monochromator and the measured 2D images have been recorded in separate files. Therefore, the measured images had to be re-sorted before any further processing was performed. A crucial part of reorganizing recorded data is the determination of an appropriate flat-field image as the incoming 2D intensity distribution of the X-ray beam changes as a function of energy. For this purpose, the flat-field images were separated into up or down oscillations according to the changing procedures in encoder values (increasing or decreasing). After that, images were sorted in 200 energy bins, each with a width of approximately 0.5 eV and containing more than 10 single flat-field images. By averaging all images of a single bin, a representative flat-field image with particular X-ray energy was obtained.

In order to determine the intensity of the transmitted X-ray beam $\mathrm{I}(E, x, y)$, the sample was moved back into the X-ray beam after recording the flat-field images.

After that, transmission images of the catalytic reactor bed were recorded with a continuously oscillating monochromator and a total exposure time of 600 s at 50 Hz, which is approximately 30 000 frames.

Due to the fast measurement, the noise level in single pixels was relatively high and the XANES spectrum extracted from each pixel was very noisy. So, in order to enhance the local XANES signal, the images had to be binned by a factor of 16 × 16 before any data processing. After that, the transmission images were further processed in accordance with Lambert-Beer law (see Eq. 2.10), which describes the absorption of X-rays by matter:

$$I(E,x,y) = I_0(E,x,y)\exp\left[-\int \mu(E,x,y,z)dz\right] \tag{4.4}$$

$$\int \mu(E,x,y,z)\,dz = -ln[\frac{I(E,x,y)}{I_0(E,x,y)}] \tag{4.5}$$

where $\int \mu(E,x,y,z)\,dz$ describes the projected attenuation of the X-ray in the beam direction as a function of energy and lateral position. In this way, these 2D absorption images of the catalytic bed were considered for further data processing.

4.1.3 Linear Combination Analysis

As XANES spectroscopy is a powerful technique used to study materials' electronic and structural properties, various data analysis techniques can be used in XANES spectroscopy to extract meaningful information from the spectra depending on data quality, the extent of prior knowledge of the studied system such as the availability of reference spectra and the information to be extracted. Some important techniques are principal component analysis (PCA), multivariate curve resolution-alternating least squares (MCR-ALS), machine learning (ML), FT, and linear combination analysis (LCA).

PCA can be applied to systems with a low understanding of the underlying chemical processes and without clearly defined reference states. There is often a prior guess regarding the number of species and their nature. However, it is challenging or impossible to obtain reference spectra comparable to the studied data. Chemometric processes such as the MCR-ALS [53] and the non-negative matrix factorization (NNMF) [54] are being used to deconvolve complex mixtures of XANES spectra and enable us to determine the individual component spectra and their concentrations in the mixture. If the purity of the internal references can be verified, e.g. through comparison of spectral features with literature, the obtained weight can be correlated to the concentration of each species.

If the data quality is poor and comparison with reference data is not possible, or when intermediate states cannot be viewed as linear combinations of reference state spectra, ML techniques such as neural networks and support vector machines may be required. However, a good understanding of the system allows the production of theoretical datasets for neural network training. ML is most commonly used to classify and analyze datasets from XANES, where no chemical transformation occurs, but only the size of nanoparticles changes [55] or to analyze EXAFS [56]. In large datasets, these methods are useful for identifying subtle differences and patterns. Also, the FT is a mathematical technique and can be applied to XANES data to transform data from the energy domain (eV) into the wavenumber domain (cm^{-1}). Through this method, it is possible to discover hidden structural and electronic information, allowing the identification of specific chemical bonds, coordination environments, and subtle variations in spectra [57].

Among these techniques, the LCA method was chosen to fit the measured XANES spectra based on the reference curves, since fits with reference spectra can systematically explain the observed spectra within the uncertainty of the noise. First of all, reference spectra were normalized by comparing the ratio between the pre-edge and post-edge of the spectra with the ratio between the pre-edge and post-edge in the theoretical platinum spectrum before the LCA. The normalized platinum oxidized and reduced reference spectra for this chemical reaction are shown in Fig. 5.6. Afterwards, the measured XANES spectra of each pixel were fitted to normalized reference spectra, see Fig. 5.7, as follows:

$$f(E) = \Sigma_{E_1}^{E_n}[af_{ox}(E) + bf_{red}(E) + c] \tag{4.6}$$

where $\mathrm{f_{ox}}$ and $\mathrm{f_{re}}$ represent the oxidized and reduced reference spectra as functions.

Here, a least-squares search was conducted in order to determine the amount of oxidized Pt, reduced Pt, and constant background (absorption by other elements) for every pixel of the 2D image by yielding the fit factors a, b, and c which sum of them should be 1. This LCA is implemented in Python using the minimize function of the SciPy package (SLSQP method), which can be used to provide quantitative information.

In order to make optimal use of the available photon flux, the XANES imaging data were acquired continuously. By this method, a total of more than 500 000 single transmission images were acquired, resulting in approximately 3800 sequences of XANES images and approximately 20 million single-pixel XANES spectra were fitted by LCA.

Since the signal-to-noise ratio of each pixel determines the quality of data fitting by LCA, this quality can be shown as the image in terms of an R-factor:

$$R = \frac{\Sigma_i[\mu(E_i) - \mu(E_{i,fit})]^2}{\Sigma_i[\mu(E_i)^2]} \tag{4.7}$$

where $\mu(E_\mathrm{i})$ and $\mu(E_\mathrm{i,\,fit})$ are the measured and fitted values of the absorption coefficient at the measured X-ray energy values (E_i). A representative example of the R factor for LCA of recorded images can be found in Fig. 5.7.

Results of this study are presented in Chapter 5.

4.2 Full-Field XANES Tomography

In this measurement, the 2D XANES imaging technique described previously has been developed into the operando full-field XANES tomography and the 3D imaging of the chemical state of a MoOx/Al_2O_3 catalyst during the ODH of ethane to ethylene was done with this technique by implementing a custom sample environment at beamline P64 (see Fig. 3.10).

It was planned to do 3D operando XANES tomography with energy- and time resolution by integrating a fast high-resolution X-ray camera into beamline P64 and synchronizing it to the QEXAFS monochromator available at this beamline. However, some electronic equipment required to read out the encoder of the QEXAFS monochromator was not operational during the beamtime such that the standard DCM was used instead of it in this beamtime. Unfortunately, this prevented running the energy scans in continuous mode as the inner loop scan motor and increased the total scanning time. For this reason, in order to still be able to record XANES tomograms, the energy scan was run as the outer scan loop and the X-ray energy had to be adjusted to distinct values around the Mo K-edge in this case. The overview of the step sizes in the defined energy range is presented in Table 4.1.

The measured energy points around the Mo K-edge spectrum are shown in Fig. 4.2.

Region	**Start energy** [eV]	**Stop energy** [eV]	**No. of steps**
pre-edge	19900	19950	5
rising edge	19950	19980	10
XANES	19980	20080	60
EXAFS	20080	20150	26

Table 4.1: Description of the energy ranges used for full-field tomography with different step sizes for different regions of the XAS spectrum.

These points were chosen such that fast variations in the Mo K-spectra can be nicely resolved while others don't need to.

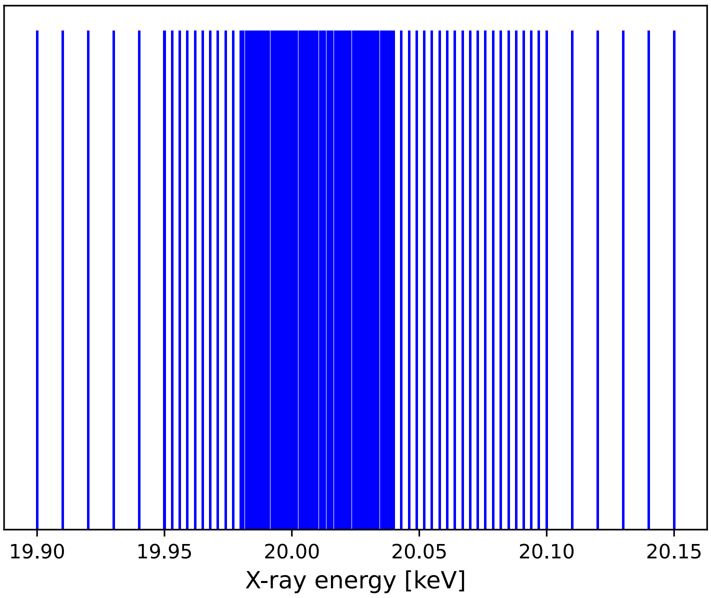

Figure 4.2: Recorded energies around the Mo K-edge spectrum.

At each energy value the high-resolution 2D X-ray camera was operating at 20 Hz full-frame rate and sequences of full-field projections of the catalytic bed were recorded across a rotational range of 180°. In this configuration, each 2D projection recorded in the 0.05 s and a single tomogram consisting of 1000 projections at one energy point was recorded in only 2 min total scan time including the time between two tomographic scans. These projection series were repeated at 105 energy points (see Fig. 4.2) in order to produce Mo K-edge XANES data at each sampling point. The total measurement time for the whole data set was about 3.5 h. It is important to note that this ODH of ethane to ethylene was a stationary reaction, and these 105 tomograms were recorded under the same conditions.

By reconstructing these sequences of projections as the function of the energy and time, XANES spectra can be obtained for each voxel (volumetric pixel) of a tomographic 3D dataset. This procedure provides a full 3D XANES dataset, which can be used to determine the local chemical oxidation state of the catalyst within the reactor bed. Detailed information regarding the experimental procedures and data analysis is provided in the following. It's crucial to emphasize that, given the substantial volume of datasets generated during this measurement, scripts were executed in parallel via the slurm ("simple linux utility for resource management") on cluster nodes, utilizing multiple cores concurrently.

4.2.1 Dark- and Flat-Field-Corrected 2D Absorption Image

Similar to the previous experiment (see Sec. 4.1.2), a sequence of images was acquired with the beam shutter closed before recording a single tomogram for each X-ray energy point. A representative dark-field image was created by averaging about 30 frames recorded at 20 Hz, i.e. about 1.5 s total exposure time, and is used to subtract from the imaging data.

At each X-ray energy point, a sequence of flat-field images, $I_0(E, x, y)$, was measured regularly by moving the sample completely out of the FOV of the detector. Based on the averaging of 20 frames recorded at 20 Hz, i. e., about one second of total exposure time, a representative flat-field image was generated. After recording this series of flat-field images, the capillary was moved into the X-ray beam and the sample stage was rotating over an angular range 0° to 180° in 1000 steps at this energy. Therefore, a single tomogram consisted of 1000 projections.

These procedures were repeated for recording the flat-field images and tomogram at each energy point, Table 4.1. In this way, full X-ray tomograms of the capillary and the embedded catalytic particles were recorded sequentially at 105 distinct X-ray energies around the Mo K-edge in a fly-scan mode. Considering the relatively high noise level in single pixels, the images were hardware-binned by a factor of 2 × 2 during the measurement. After that, these images were binned computationally during the data processing again by another factor of 2 × 2 to enhance the XANES signal. Hence, the effective pixel size in all images was 2.6 µm.

Before any data processing, all flat-field and projection images were dark-field corrected and pixels with negative values were replaced with zero. Afterwards, projection images were processed by using Lambert-Beer's law to obtain the attenuation coefficient in matter μ (see Eq. 4.5) and are used for the reconstruction of object.

4.2.2 Correct the Rotation Angle Offset

In order to rotate the capillary between 0° 180° in 1000 steps at each energy point, the rotation motor is moved to a certain angle and accelerated to a constant velocity. When the motor reached this velocity, the high-resolution detector received exactly 1000 trigger pulses which led to the recording of 1000 images. Afterwards, the motor decelerated and came to a stop. This procedure was repeated at 105 energy points (see Table 4.1).

Since the first trigger is not perfectly synchronized to a certain angle value, slight offsets existed in the rotation angle which should be corrected for each tomogram. This offset was corrected by comparing the first rotation angle of these 105 recorded tomograms, taking the minimum value of these angles as an offset, and subtracting it from all rotation angles. As an example, Fig. 4.3(a) and Fig. 4.3(b) illustrate the first rotation angles of the recorded tomograms before and after the correction of the offset.

4.2.3 Find the Rotation Center

The rotation center is an essential component of tomographic imaging and reconstruction. In tomographic data acquisition, the rotation angle is used to ensure that projection images acquired from various angles are positioned and oriented correctly with respect to the rotation axis and it facilitates an accurate reconstruction of the sample's internal structure. When the rotation center is incorrect, the reconstructed image may exhibit distortions, blurring, or misalignment.

The Tomopy Python library is widely used for the reconstruction and analysis of X-ray CT images [58]. This library offers a comprehensive set of tools and algorithms, including image processing, image reconstruction, and artifact correction. The "tomopy.write_center" function in this library was used to estimate the rotation center value in each tomogram. By supplying a stack of 2D projection images and their rotation angles at each tomogram into this function, the routine determined the position of the rotation axis in the measured projections of the recorded tomogram. Based on this rotation center, the recorded projections were aligned and reconstructed,

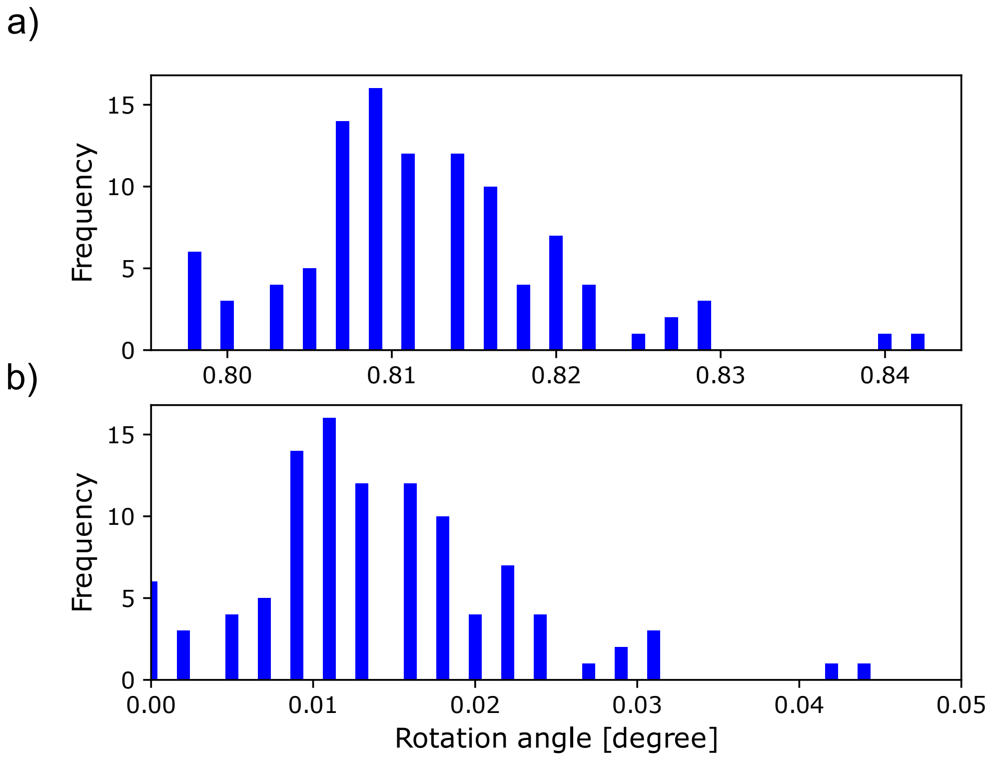

Figure 4.3: Illustration of the first rotation angles of the 105 recorded tomograms before (a) and after correction of offset (b).

as described in the following.

4.2.4 Alignment of Projections

In this step, projections from the same angle of rotation were aligned to each other at each energy point. This alignment was performed in order to compensate for fluctuations in the beam intensity and correct the misalignment before performing the tomographic reconstruction. Two alignment functions are available in the Tomopy Python library: "tomopy.prep.alignment.align_joint function" and "tomopy.prep.alignment.align_seq function".

While the first function considers all projection images as a single dataset and aligns together as a single process based on a common alignment strategy, the second function aligns each projection image independently based on its own alignment parameters. The alignment of projections with each of these two functions is based on one of the following algorithms: ART, fourier grid reconstruction algorithm (GRIDREC), maximum-likelihood expectation maximization (MLEM), SIRT, gradient descent method with a constant step size (GRAD) [59].

In this measurement, the first function by using the SIRT algorithm with 50 iterations at each energy point provided the best alignment of the recorded projections. In this way, the recorded 2D projections of the same rotation angle were aligned to each other perfectly by reducing fluctuating beam intensity and shifts between projection images.

4.2.5 Reconstruction

Reconstruction is a fundamental stage in tomographic imaging that facilitates the visualization and analysis of an object's internal structure by generating 3D representations of objects from recorded projections data. The ASTRA Toolbox is an open-source software package designed for image reconstruction in tomographic imaging modalities [60] that is used in this measurement. This toolbox offers a variety of reconstruction algorithms and tools, including fast analytical algorithms like the FBP, and SIRT for reconstructing high-quality images from projection data [61]. These algorithms are described in more detail in Sec. 2.4.4.

After the alignment step, the projections of each energy point were individually reconstructed using the FBP (FBP_CUDA (Compute Unified Device Architecture)) algorithm of the ASTRA Toolbox. This FBP reconstruction algorithm outperformed other algorithms and yielded the highest-quality result.

As the Astra Toolbox requires a definition of tomographic geometry for reconstruction, the rotation center of each tomogram, the size of the projection images, the pixel size, and the geometry of the beam were defined. In the first step of the reconstruction with this algorithm, projections are filtered in order to emphasize the low-frequency components and to eliminate the high-frequency components in the Fourier space. Afterwards, the filtered projections were then back-projected into real space to reconstruct the volume. As the CUDA algorithm is a parallel computing platform, it was used here to speed up the FBP by paralleling the filtering and back-projection steps.

4.2.6 XANES Spectra

The previous measurement (2D XANES imaging) allowed us to determine the oxidation state of the catalyst during the chemical reaction by analyzing the full

XANES spectrum. In this measurement, the previous step led to a reconstructed 3D volume for each individual energy point. The full XANES spectrum for each spatial voxel in the sample, with a voxel size of $2.6 \times 2.6 \times 2.6\,\mu\mathrm{m}^3$ is finally obtained. In this way, the spectrum can be used in order to determine the catalyst's oxidation state by the LCA method, as discussed below in more detail.

4.2.7 Linear Combination Analysis

Similar to the previously presented 2D XANES imaging (see Sec. 4.1.3), the LCA was used to evaluate the individual spectra that are now related to each voxel within the 3D volume. According to the measurement conditions, different reference spectra were considered for LCA method, as shown in Fig. 6.6 and Fig. 6.7.

After the normalization of reference spectra (similar way with the previous measurement), the XAS spectrum of each voxel was fitted to Mo oxidized and reduced reference spectra in the energy range of 19.94 keV to 20.15 keV by using Eq. 4.6. In this way, the relative concentrations of oxidized and reduced Mo material, as well as the constant contributions of other materials equivalent to the fitting coefficients a, b, and c were determined in each voxel. A representative example of the LCA is shown in Fig. 6.8.

4.2.8 Avizo

Obtaining meaningful data on dynamic systems requires visualization of the results of the previous step in order to gain a deeper understanding of reaction mechanisms and changes in the oxidation state of the catalyst. Visualizing the reconstructed volume through the use of various techniques, such as volume rendering, cross-sectional slices, and surface rendering, can provide valuable information regarding the object's structure and composition.

Thermo Fisher Scientific has developed a commercial software package known as Avizo to facilitate the visualization and analysis of three-dimensional data for scientific applications. Avizo's visualization tool plays a crucial role in understanding the spatial relationships, structures, and attributes present in complex 3D models. It includes many significant customization options, including rendering modes, lighting and shading, color mapping, transparency, and opacity, as well as animation and interactivity [62].

Internal structures of the retrieved chemical data in this measurement were visualized by using the volume rendering technique in Avizo. By utilizing color mapping techniques in Avizo and assigning different color scales to the amount of oxidized and reduced Mo particles which are obtained by LCA method, the chemical gradient along the catalyst bed was determined and the dynamic changes in chemical reactions were analyzed.

Results of this study are illustrated in Chapter 6.

5 Rapid 2D-XANES Full-Field Imaging

Due to the focus of this thesis on the development of a method for high spatial and temporal imaging of heterogeneous catalysts, a rapid 2D XANES imaging measurement technique was investigated. This chapter starts with a general introduction to this method in Sec. 5.1. Sec. 5.2 presents an overview of the CPO of methane reaction, which was studied using this technique. Details regarding the catalyst synthesis and reaction conditions are provided in Sec. 5.3. Afterwards, this chapter continues with the results of this chemical reaction under operando conditions in Sec. 5.4. Parts of the text and figures in this chapter were adapted and reprinted from Alizadehfanaloo, et al. [12].

5.1 Overview of this Experiment

Extending beyond conventional spectroscopic characterization with bulk XAS, a concept for monitoring dynamic changes with high spatial and time resolution in heterogeneous catalysis was investigated at beamline P64, PETRA III. In this method, a QEXAFS monochromator was synchronized with a 2D X-ray camera operating at 50 Hz full-frame rate, enabling the acquisition of entire XANES spectra 'on the fly' in a rapid and spatially resolved manner as well as providing new insights into the dynamic processes occurring within catalysts and other functional materials at work [12]. This rapid spectromicroscopy approach combines spatial and temporal resolution together with chemical contrast over individual pixels.

Considering that catalysts are often complex 3D objects, the proposed method provides more detailed information regarding the chemical and structural composition of the catalyst within the reactor. In principle, this spectromicroscopy technique can improve chemical processing efficiency and identify catalytic active sites during the process.

Here, the chemical gradients within a model Pt/Al_2O_3 catalyst during the CPO of methane to synthesis gas were investigated with this technique under operando conditions. By using this developed method, the entire catalytic microreactor was imaged rapidly and the spectroscopic data at each pixel along the Pt L_3 absorption edge was recovered [12]. This chemical reaction is described in the following.

5.2 Partial Oxidation of Methane to Synthesis Gas

Synthesis gas, a mixture of hydrogen gas (H_2) and carbon monoxide (CO), is a versatile intermediate product that plays a crucial role in a variety of industrial processes to produce fuels, chemicals, and other valuable products. Steam Reforming of Methane (SRM) is a big industrial process and the source of 95 % of all syngas. It involves a series of endothermic chemical reactions as follows:

1) Reforming of methane:

$$CH_4 + H_2O \rightarrow CO + 3H_2, \tag{5.1}$$

2) Water-gas shift reaction:

$$CO + H_2O \rightarrow CO_2 + H_2. \tag{5.2}$$

This SRM chemical process is conducted at high temperatures and nickel-based catalysts are commonly used in it. It is possible to separate the hydrogen component of syngas and use it for a variety of purposes, including the production of fuel cells.

Catalytic partial oxidation of methane to syngas is another chemical process for producing syngas. It is of interest to the hydrogen economy concept, as it offers a potentially energy-efficient route towards the generation of syngas as an alternative to large-scale and energy-intensive methane steam reformer facilities [63, 64]. This process has been studied over a wide range of catalysts in the literature and an overview of them can be found in a review published by Enger, et al. [64].

CPO over noble metal catalysts such as platinum, palladium, or rhodium has demonstrated an interesting oscillatory behavior, whereby several reaction pathways become active under different temperature conditions, including methane combustion, direct partial oxidation (DPO), and combustion reforming, among others [65–67].

Due to the dynamic nature of the reaction and possible transition between oxidized and reduced states as a function of temperature, CPO is an ideal model system and case study for rapid spectromicroscopy. It is an alternative method that is currently being investigated and has the potential to perform at milder conditions over platinum catalysts. However, it is not an established industrial process.

In this process, the reaction between methane and oxygen in order to form the syngas can occur in two different chemical paths, depending on the temperature of the system. It is possible that both of these mechanisms occur simultaneously. First, a small amount of combustion of methane can be expected in order to increase the temperature, which is a two-step process involving catalytic combustion and reforming of methane. In this mechanism, firstly the combustion of methane takes place at low temperatures and carbon dioxide (CO_2) and water (H_2O) are formed. After that, methane reacts with the CO_2 and H_2O and reforms into the CO and H_2 as summarized in the following [68]:

A: Catalytic Combustion and Reforming (CCR)

1) Combustion of methane:

$$CH_4 + 2O_2 \rightarrow CO_2 + 2H_2O, \qquad \Delta_r H^{\circ} = -801.7\,\mathrm{kJmol^{-1}}. \tag{5.3}$$

2) Reforming of methane:

$$\begin{aligned} CH_4 + H_2O &\rightarrow CO + 3H_2, & \triangle_r H^{\circ} &= 206.1\,\mathrm{kJmol^{-1}}. \\ CH_4 + CO_2 &\rightarrow 2CO + 2H_2, & \triangle_r H^{\circ} &= 247.5\,\mathrm{kJmol^{-1}}. \end{aligned} \tag{5.4}$$

Considering the exothermic nature of methane combustion and the endothermic nature of reforming, an ideal stoichiometry results in an overall exothermic reaction.

DPO of methane is another alternative pathway for the formation of syngas. It can take place at higher temperatures and is an exothermic process [69]:

B: Direct partial oxidation (DPO)

1) Partial oxidation of methane:

$$CH_4 + \frac{1}{2}O_2 \rightarrow CO + 2H_2, \qquad \triangle_r H^{\circ} = -35.5\,\mathrm{kJmol^{-1}}. \tag{5.5}$$

As the transition between these paths affects the oxidation state of Pt, where combustion may occur on an oxidized surface and reforming without oxygen leads to a reduced state, the presented imaging technique can be used to monitor these changes in the oxidation state of the catalyst and provide information regarding possible reactions paths. The following are the details of the experiment method and the results of studying this chemical reaction.

5.3 Experimetal Details

The following section provides further details regarding the experiment parameters, such as the catalyst, the gas composition, the flow rate, the temperature program, and the experimental method.

5.3.1 Catalyst Synthesis

The catalyst was prepared by incipient wetness impregnation, using γ-alumina support (Puralox SCFa-230, Sasol) with specific surface area approximately $230\,\mathrm{m^2\,g^{-1}}$ and hexachloroplatinic acid ($H_2PtCl_6.xH_2O$, Merck) as Pt precursor. The latter was dissolved in water and added dropwise to the support, resulting in a Pt/Al_2O_3 catalyst with 2.2 wt% Pt loading according to atomic absorption spectroscopy [70]. The resulting powder was dried overnight at 70 °C and calcined at 500 °C for 2 h in static air before further use. The catalyst was pressed and sieved. A fraction with grain sizes between 100–200 µm was used for this experiment [12].

5.3.2 Reaction Conditions

The operando 2D imaging setup described in Sec. 3.2.1 was used in this measurement. The catalyst material (2.2 wt% Pt/Al_2O_3) was filled as a sieved powder into a capillary with an outer diameter of 0.5 mm and fixed in position with glass wool. Catalyst bed length was approximately 6 mm and the experimental setup including the chemical reactor is shown in Fig. 3.9. The gas mixture of 3 % CH_4/1.5 %O_2/He was provided as reactants with a flow rate of $15\,\mathrm{mL\,min^{-1}}$.

In this measurement, the reactor bed was gradually heated up from room temperature with distinct steps and the temperature was measured with thermocouples attached to the nozzle of the air blowers. Since no reaction was expected until higher temperatures, the temperature was rapidly increased in bigger steps of 25 °C up to about T = 250 °C. Afterwards, the step size was reduced to 10 °C in order to precisely find the ignition of the chemical reaction [12]. In this way, several reaction zones with distinct changes in the oxidation state of Pt were observed: pre-ignition (temperature from 50 °C to 290 °C), the CPO ignition point (temperature around 290 °C), and several temperature steps above the ignition point (temperature from 290 °C to 370 °C).

5.3.3 2D XANES Imaging During CPO of Methane

After thermally stabilizing the catalyst bed at each temperature, the gas analysis was performed by MS and a sequence of energy-resolved transmission images was recorded which yielded full 2D XANES spectra. As the QEXAFS monochromator oscillated at a frequency of 0.18 Hz, information on the local chemical state as a function of time and the applied temperature was obtained for a single full up or down sweep over the Pt L_3 absorption edge in about 2.8 s (see Sec. 4.1) [12].

In this configuration, the recorded 2D images had a FOV of 1.33 mm by 1.33 mm, well matched to the horizontal and vertical beam size at P64. It should be noted that although the sample was illuminated continuously with high photon fluxes, radiation damage was not observed and the sample stability was not critical at this length scale. The images recorded during this measurement were analyzed using self-developed data processing methods, as described in Sec. 4.1.

5.4 CPO Results

Following are the results of the gas analysis during the reaction, as well as the analysis of the 2D images recorded during the reaction.

5.4.1 Mass Spectrometry Data

The kinetic of this chemical reaction was examined during the measurement by connecting the MS to the outlet of the catalyst bed.

This chemical reaction took around 5.5 h and the ignition started about 3.5 h after the beginning of the experiment at a temperature of around 290 °C (see Fig. 5.1 (a)). Within the pre-ignition region, the concentrations of CH_4 and O_2 as reactant gases were stable (see Fig. 5.1(b)). These results are consistent with previous studies about

a) temperature evolution

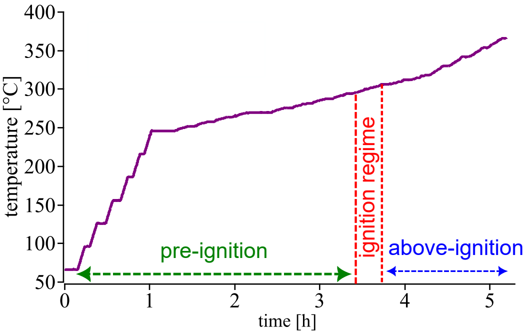

b) reaction educts

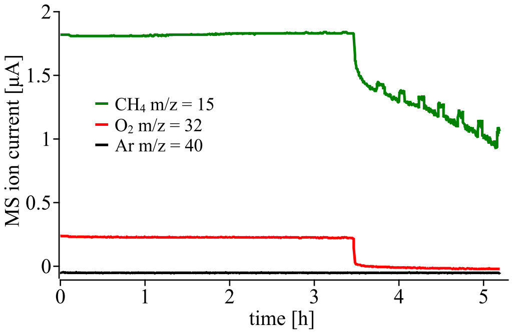

c) reaction products

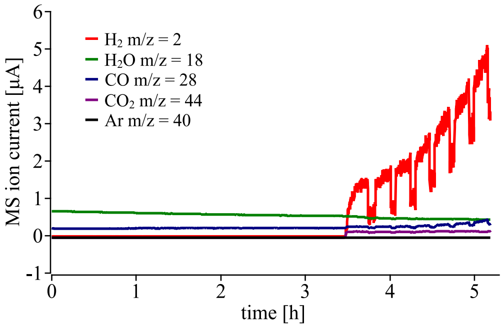

Figure 5.1: (a) Temperature profile of the catalyst bed during the CPO reaction; (b,c) Profiles of reactants and products measured by MS; Reprinted from Ref. [12].

this reaction that indicate relatively low activity for methane combustion when Pt alone is used [71].

Around the CPO ignition point, the abrupt consumption of CH_4 and O_2 gases and production of H_2, CO, and CO_2 gases were visible. Above this zone, the product profile (see Fig. 5.1 (c)) indicates the amount of CO and H_2 is increased by continuous consumption of the reactants. In fact, the full consumption of oxygen led to the reduction of the catalyst in this zone which this reduction is visible in the recorded images.

During the recording of flat-field images, the capillary was slightly moved out of the X-ray beam and away from the gas blowers. This movement resulted in a temperature drop and a lower conversion. Prior to ignition, no significant conversion was observed. Above the ignition region, the reaction profile displays seven distinct jumps in conversion, corresponding to the moments when the capillary was shifted out of the X-ray beam to collect flat-field images, resulting in slight changes in conversion [12].

5.4.2 2D XANES Imaging Data

Fig. 5.2 represents an exemplary dark- and flat-field corrected absorption image of the catalytic bed.

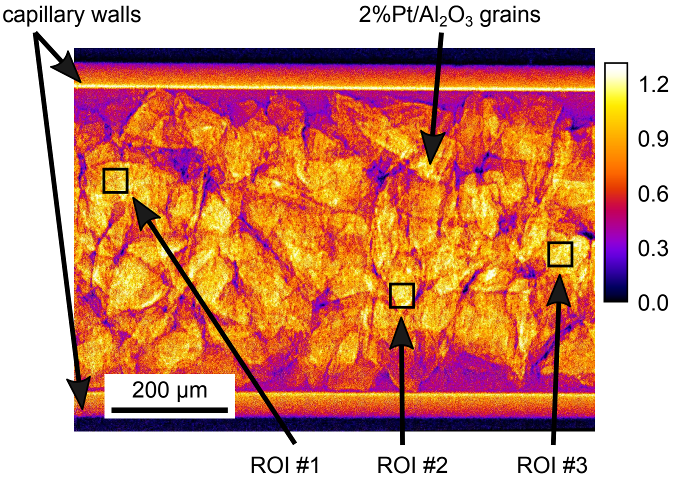

Figure 5.2: Dark- and flat-field-corrected 2D absorption image of the glass capillary containing the 2.2 wt% Pt/Al_2O_3 grains. This image was measured at an X-ray energy of 11.54 keV; Reprinted from Ref. [12].

As discussed in the previous chapter (see Sec. 4.1.2), the recorded images were binned by a factor of 16 × 16 due to the high level of noise in the single pixels. In this way, the pixel size was the 10.4 µm × 10.4 µm. After the binning, dark- and flat-field corrected absorption images of a catalytic reactor bed were calculated for all recorded 2D images at each temperature and were considered for further data processing. A representation of the absorption images of the catalytic bed at various X-ray energies during the single full-up sweep at T = 127 °C are shown in Fig. 5.3(a) - 5.3(d).

Since transmission images of the Pt/Al_2O_3 catalyst bed at different energies display the absorption for a particular energy, particles can be distinguished in terms of the transmitted beam intensity. In Fig. 5.3, at an energy below the absorption edge of Pt L_3 (E = 11.566 keV) the much smaller absorption is visible. Afterwards, the

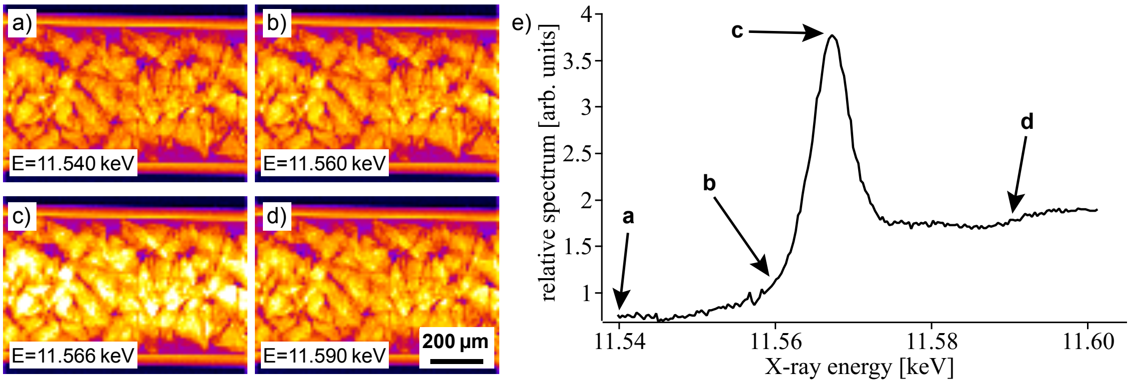

Figure 5.3: (a)-(d) Binned absorption images of the catalytic bed measured at different X-ray energies and at a temperature of T = 127 °C; (e) A representative XANES spectrum was obtained by averaging over the three ROIs, indicated in Fig. 5.2. Color bar is shown in Fig. 5.2; Reprinted from Ref. [12].

absorption increases significantly at the edge position and decreases again at the energy above the absorption edge. The whole image at the edge position (Fig. 5.3(c)) indicates greater absorption and more oxidized Pt particles.

In order to determine the dynamic changes of the catalyst from the XANES spectrum, XANES spectra were extracted by averaging the absorption signal over three regions of interest (ROI) from all images captured during a single oscillation of the QEXAFS monochromator. The positions of these ROIs are illustrated in Fig. 5.2 and an example of the obtained XANES spectrum from these ROIs at T = 127 °C is shown in Fig. 5.3(e). A spectrum represents the changes in the amount of absorption by particles at different energies.

The XANES spectra, extracted by averaging over the three ROIs, at different temperatures during the pre-ignition are shown in Fig. 5.4. At the beginning of the experiment (T = 66 °C), the XANES spectrum shows an intense absorption peak (white line), suggesting that Pt was fully oxidized. With increasing temperature from T = 66 °C to T = 282 °C, the white line gradually becomes less intense, indicating a slow homogeneous reduction of Pt particles before the actual start of the ignition. This behavior is in agreement with relatively low activity towards methane combustion over Pt/Al_2O_3 catalysts, since at the same time no appreciable methane consumption was observed by MS (see Fig. 5.1).

A comparison of XANES profiles obtained from different reaction zones is illustrated in Fig. 5.5. At the pre-ignition region (black line), XANES spectra indicated fully oxidized Pt located within the catalyst bed. Before the ignition, heating removed

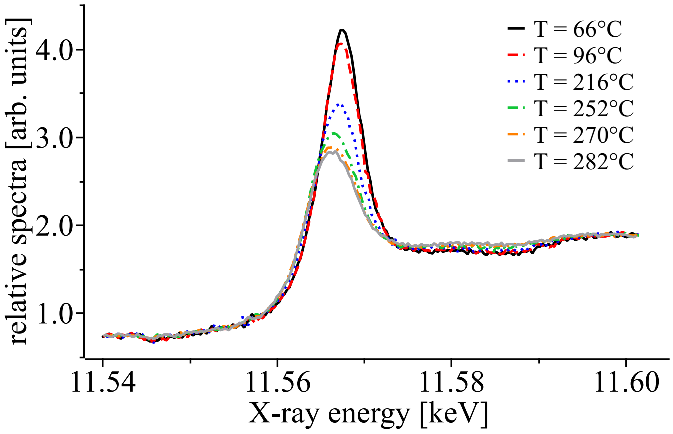

Figure 5.4: A comparison of XANES spectra measured at different temperatures during the pre-ignition phase; Reprinted from Ref. [12].

gradually oxygen species from the surface of the catalyst which fully oxidized particles reformed into partially oxidized particles, and the gradual disappearance of the white line (blue dashed-dotted line) was observed. By consumption of all oxygen at the very end of the chemical reaction, the complete reduction of Pt occurred (red dashed line).

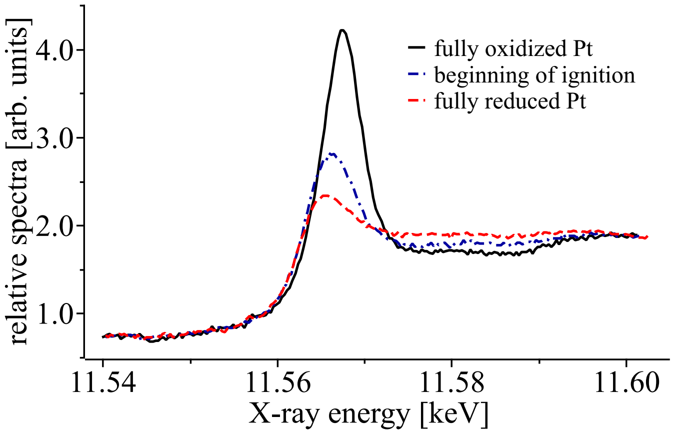

Figure 5.5: The comparison of XANES spectra measured at the beginning, during the ignition of the chemical reaction, and at the end of the chemical reaction; Reprinted from Ref. [12].

In order to determine the local Pt oxidation state of the reactor as a function of time, the LCA data fitting was performed at each temperature for each pixel of the sequence of recorded images considering the appropriate reference spectra (see Eq. 4.6). The fully oxidized (black line) and fully reduced (dashed red line) spectra shown in Fig. 5.5 were considered as reference spectra for LCA data fitting in the pre-ignition region. For visualizing the rapid chemical reduction of Pt within the reactor bed during the ignition zone and above it, the LCA data fitting was performed with consideration of the partial oxidized (at the beginning of the ignition phase, around 270 °C) and fully reduced (at the end of the chemical reaction, around 370 °C) Pt spectra, as illustrated in Fig. 5.6.

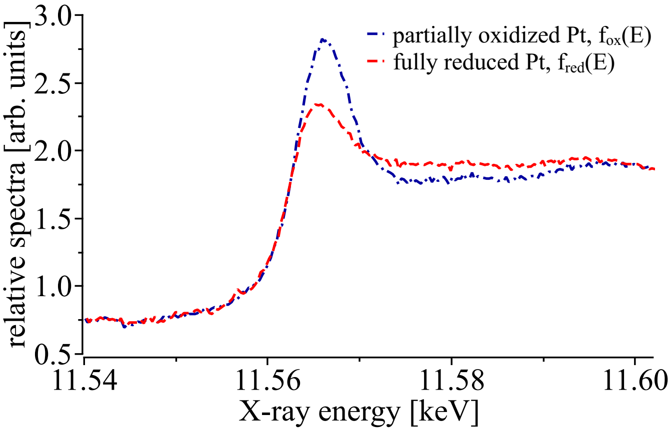

Figure 5.6: Reference spectra extracted from sequences of X-ray transmission images of the partially oxidized (dash-dotted blue line) and fully reduced (dashed red line) catalytic reactor bed; Reprinted from Ref. [12].

Fig. 5.7 illustrates the example of fitting LCA data with images of the fitting coefficients a, b, and c, which correspond to the amount of oxidized (Fig. 5.7(a)) and reduced Pt (Fig. 5.7(b)), as well as a constant offset that is unrelated to Pt (Fig. 5.7(c)). In principle, the background (c coefficient) plays a greater role than other factors, which is visible in the color bar. At this temperature (ignition zone), the distinct interface between oxidized and reduced Pt was visible by this technique.

In order to illustrate the quality of the LCA data fitting, two pixels were selected at the oxidized and reduced regions of the catalytic reactor (see Fig. 5.7(a) and Fig. 5.7(b)). XANES spectrum obtained from the pixel in the oxidized region is shown with a triangle, and the reduced region is shown with a diamond. In Fig. 5.7(d) - 5.7(e), the quality of fitting spectra of these pixels to the reference spectra are shown. Results demonstrate a high-quality fitting outcome.

Furthermore, the plot of the signal-to-noise ratio of each pixel (see Eq. 4.7) is shown in Fig. 5.7(f). This ratio varied from about $0.5 \cdot 10^{-3}$ to $3 \cdot 10^{-3}$ with the highest values in areas with low imaging contrast, meaning a lower Pt content.

In microscopy and image processing, fourier ring correlation (FRC) is a powerful method of assessing the resolution and spatial frequency information of images. FRC evaluates the similarity between two images of the same object by transforming them

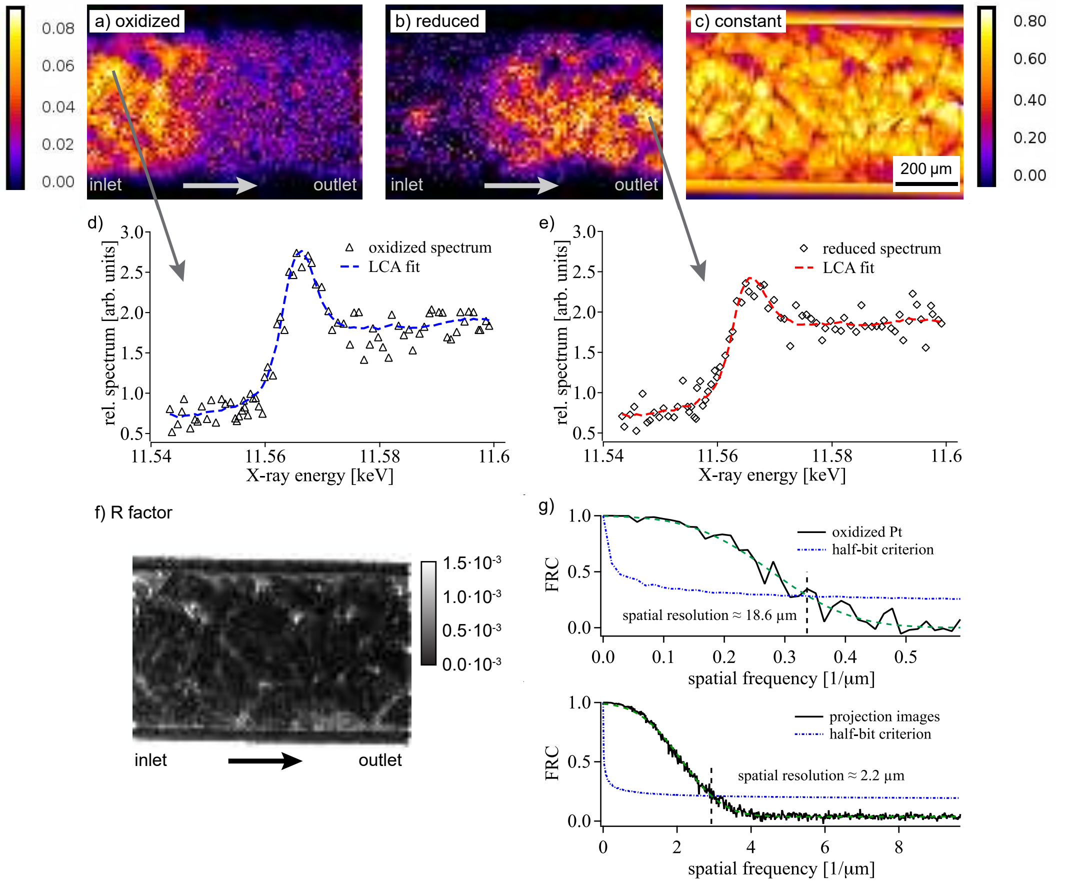

Figure 5.7: (a) Amount of oxidized Pt, (b) reduced Pt, and (c) the distribution of other materials measured at a temperature of approximately 290 °C. Since the glass capillary does not contain any Pt, the glass capillary can only be seen in (c). The scale bar corresponds to the a and b coefficients shown on the left side of the image a). The scale bar corresponding to the c coefficient is shown on the right side of the image c); (d, e) Single XANES profiles were extracted from areas as indicated in the upper images (a, b) and LCA data fitting of them; (f) R-factor map showing differences in fit quality depending on the amount of Pt in a pixel (scaled between 0 and $1.5 \cdot 10^{-3}$ to enhance visibility); (g) FRC analysis using two subsequent XANES images before ignition yields a spatial resolution of 18.6 µm. Raw transmission images have a spatial resolution of approximately 2.2 µm, as indicated in the lower FRC spectrum; Reprinted from Ref. [12].

into Fourier space and computing a correlation image from their fourier transformations [72]. As the concentric rings are defined at different spatial frequencies, the correlation coefficient between those rings is then calculated as a function of spatial frequency for each ring. In this way, it is possible to estimate the resolution of an image by examining the correlation curves [72, 73].

In this measurement, the spatial resolution was determined by this technique based on two subsequent images of the time series. Results indicated that the spatial resolution decreased for the raw imaging data (unbinned) from 2.2 µm (half-period) (lower FRC plot in Fig. 5.7(g)) to about 10 µm for the constant background image and slightly more than 20 µm for the images of the oxidized or reduced Pt distribution (upper FRC plot in Fig. 5.7(g)). As an extension of previous 2D operando XANES experiments [13,65], the results demonstrate the high potential of XANES microscopy for the visualization of catalytic chemical reactions under operando conditions.

The LCA data fitting for all recorded images at various temperatures was performed. In the following, the results of the LCA data fitting at different chemical reaction zones are illustrated. At each time scale, the upper image represents the 2D distribution of oxidized Pt, while the lower image depicts the reduced distribution of Pt.

Results of LCA data fitting at different temperatures at the beginning of the experiment are shown in Fig. 5.8.

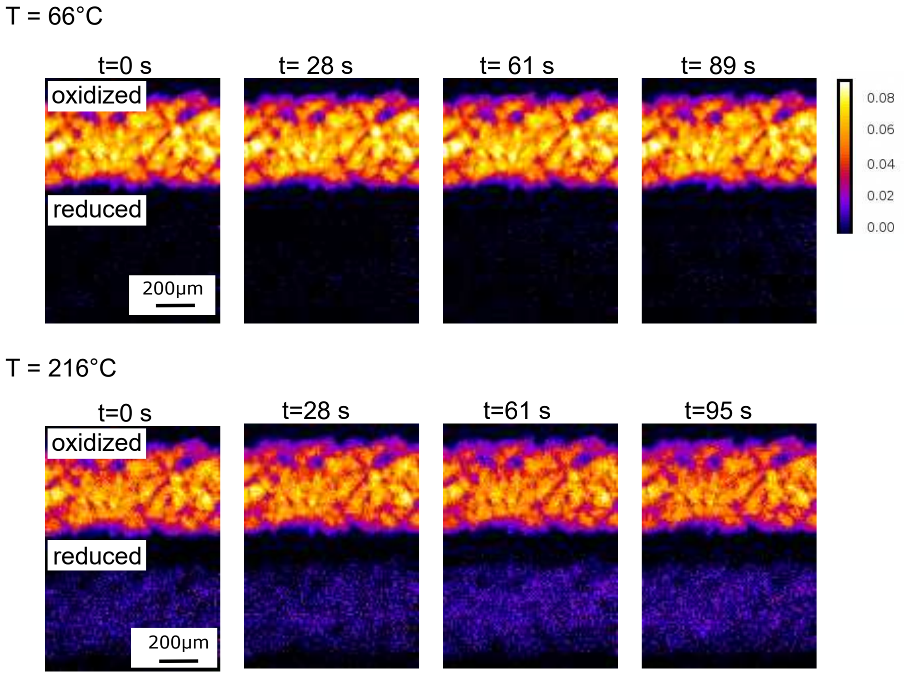

Figure 5.8: 2D distribution of oxidized Pt (upper images) and reduced Pt (lower images). Gas flowed from the left to the right of the catalyst bed. The first row illustrates results corresponding to T = 66 °C and the second row illustrates results corresponding to T = 216 °C. The t = 0 s at the first row (T = 66 °C) corresponds to the 0 min over the whole duration of the reaction. At the second row (T = 216 °C), t = 0 s corresponds to the 37 min over the entire reaction period.

At the temperature T = 66 °C, the results indicate that the catalyst bed was filled with the fully oxidized Pt catalyst and no reduced particles were visible. At the higher temperature in this region (T = 216 °C), the amount of oxidized Pt particles was decreased compared to the lower temperature (T = 66 °C). In fact, the gradual removal of oxygen species from the catalyst surface at the higher temperatures in this region led to a slow formation of reduced Pt particles as can be seen. This behavior corresponds to the gradual weakening of the white line in the XAS spectra during the pre-ignition phase (see Fig. 5.4).

The ignition started about 3.5 h after the beginning of the experiment which coincided with a sudden consumption of CH_4 and O_2 and the generation of H_2, CO, and CO_2, as indicated by MS (see Fig. 5.1). The overview of the LCA data fitting results during the ignition phase over time duration can be found in Fig. 5.9. The t = 0 s in this region corresponds to the 210 min over the whole duration of the reaction.

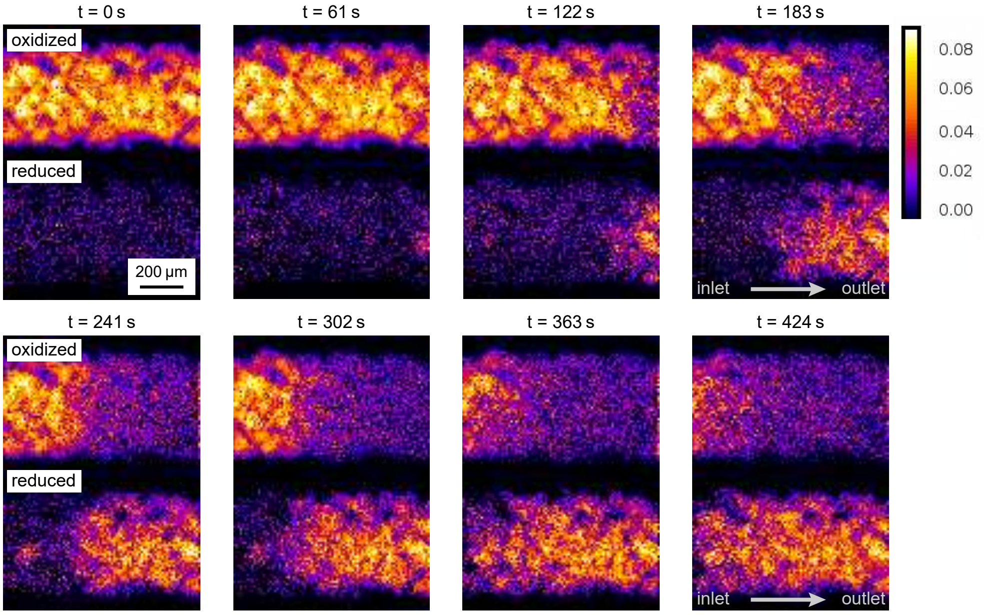

Figure 5.9: 2D distribution of oxidized Pt and reduced Pt during the ignition phase. The t = 0 s in this zone corresponds to the 210 min over the entire reaction period. The reduction of Pt begins at the outlet (right side) of the catalytic reactor and then moves rapidly toward the inlet [12].

Results indicate that during the ignition at t = 0 s the catalyst bed was filled with oxidized particles. Through the consumption of CH_4 and O_2 gases and production of H_2, CO, and CO_2 in this chemical region (see Fig. 5.1), the amount of oxidized species decreased as the amount of reduced species increased over time. At t = 61 s, a small amount of the reduced Pt catalyst was observed at the reactor's outlet, indicating that the reduction begins at the outlet. In this way, the relatively sharp interface between oxidized and reduced Pt forms was visible at t = 183 s. This interface then moved rapidly towards the inlet of the catalyst bed in about 7 min. Hence, by consumption of the whole amount of oxygen at this region (see MS, Fig. 5.1), the oxidation state of the catalyst bed changed to completely reduced and the catalyst bed was filled with the reduced particles after about t = 424 s.

The amount of oxidized and reduced Pt species along the capillary can be determined based on these LCA results. Fig. 5.10 is derived from Fig. 5.9 and illustrates the fraction of oxidized and reduced Pt-species along the catalyst bed during the ignition as a function of time. The t = 0 s in this region corresponds to the 210 min over the whole duration of the reaction.

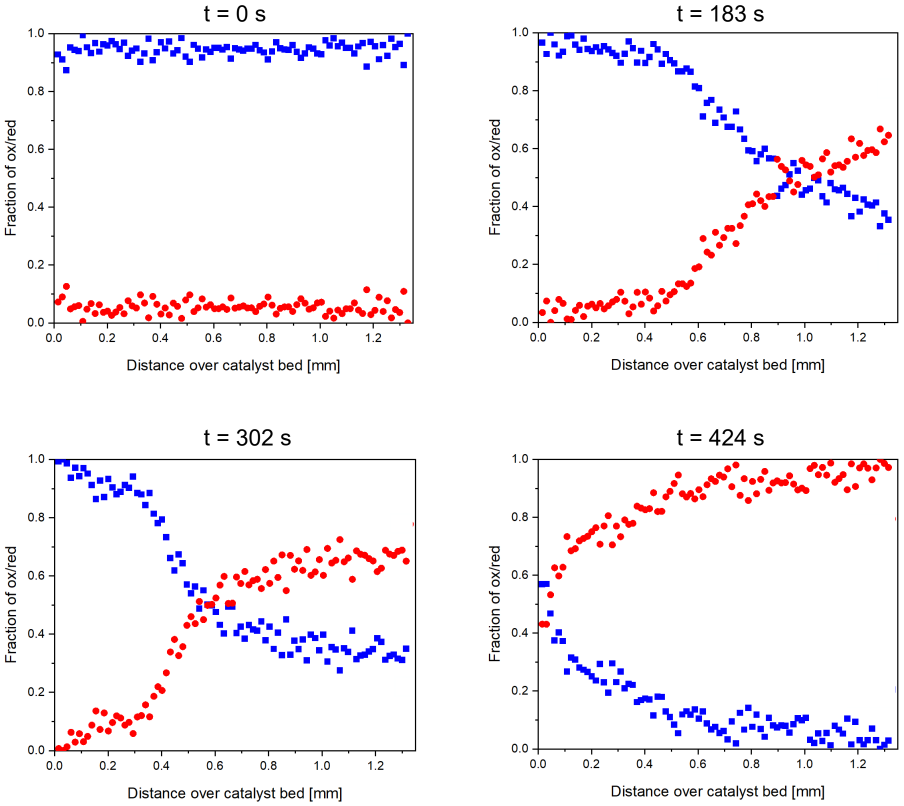

Figure 5.10: The distribution of oxidized and reduced Pt-species during the ignition phase. Blue squares represent the oxidized Pt and red bullets represent the reduced Pt. The t = 0 s in this zone corresponds to the 210 min over the entire reaction period.

At time t = 0 s, the amount of the reduced particles was close to zero as expected. At t = 183 s, the fraction of the reduced particles was increased by decreasing the amount of the oxidized particles at the end of the catalyst bed (between 0.9 mm to 1.3 mm length of the catalyst bed) which this fraction was around 10 % of the total fraction at position 0.5 mm of the catalyst bed. Afterwards, the fraction corresponding to reduced particles was increased to 35 % at t = 302 s and 80 % at t = 424 s at position 0.5 mm within the catalyst bed. In this way, at t = 424 s from the 0.5 mm to 1.3 mm of the catalyst bed was occupied by 95 % reduced particles and less amount of the oxidized particles.

As the results of LCA data fitting at different temperatures above the ignition regime were similar to each other, only the result of the temperature T = 325 °C is shown here (see Fig. 5.11). Due to the complete consumption of oxygen during the ignition phase and the production of syngas (see MS, Fig. 5.1), the Pt particles were completely reduced over the whole catalyst bed at temperatures above the ignition zone that were visible in the results of LCA.

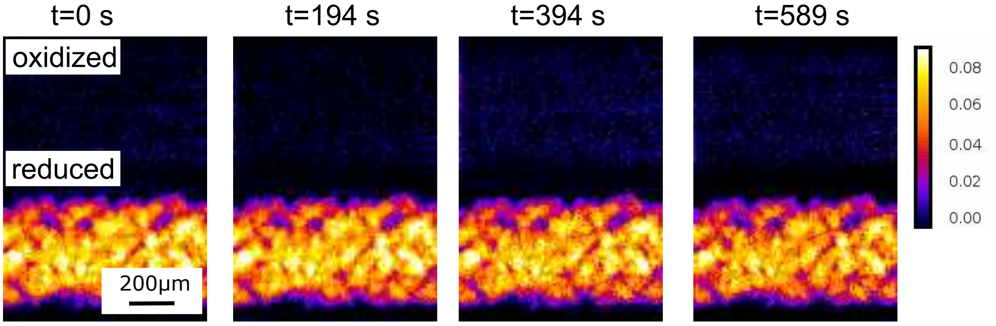

Figure 5.11: 2D distribution of oxidized Pt and reduced Pt above the ignition phase at T = 325 °C. At this temperature, t = 0 s corresponds to the 280 min over the entire reaction period. Pt particles are slowly being reduced.

5.5 Conclusion

This research presented a demonstration of rapid 2D-XANES imaging at beamline P64, PETRA III. The chemical state of a Pt/Al_2O_3 catalyst during CPO of methane to synthesis gas was investigated as the proof-of-concept of this method. In order to tune the photon transmittance through the reactor tubes to suitable values for XAS experiments, the catalyst weight loading was selected to 2.2 wt% Pt on Al_2O_3 and the catalyst was filled inside of the reactor with the outer diameter of the 0.5 mm. By using a pair of hot air blowers, the sample was heated from room temperature to 350 °C. In this measurement, the catalytic activity of the catalyst is recorded by an online gas analysis with MS during imaging, which allows full monitoring of the chemical state of the catalyst in operando conditions.

By synchronizing a fast, continuously oscillating, QEXAFS monochromator with a high-resolution X-ray camera full XANES movies could be recorded at a time resolution of 2.8 s. The spatial resolution on the other hand was limited by the incoming photon flux and the sensitivity of the detector to about 20 µm with chemical contrast. According to the XAS spectra obtained in this measurement, fully oxidized Pt catalysts were located inside the catalyst bed at low temperatures and were then partially oxidized when the temperature was raised. At the ignition regime by full consumption of the oxygen, this method resolved a spatial gradient between partially and fully reduced Pt inside the catalyst bed. This gradient moved from the outlet to the inlet of the catalyst bed on a minute timescale. Furthermore, results indicated that only reduced Pt catalysts were detected at temperatures above this ignition regime.

The obtained results in this study for CPO of methane over the Pt catalyst are consistent with previous XAS measurements [65]. A significant aspect of my research is the ability to record 2D images of a large section of the catalyst bed with high time resolution, as well as with energy-resolved XANES spectra. In contrast to previous X-ray spectro-microscopy studies, which either focused on rapid imaging at single energy or on relatively slow imaging across the XANES region [10, 51], I achieved combining all of the above in this research. With the ability to perform rapid spatially and energy-resolved measurements with this method and illustrate the gradient between oxidative and reductive processes in this simple case study, this spectroscopic imaging is able to provide a more accurate representation of the reaction progress and can extend to other complex chemical systems [12].

In the next step, the method was further developed into operando XANES tomography which is introduced in greater detail in the following.

6 XANES Full-Field Tomography

The 2D XANES imaging technique presented in Chapter 5 was extended to 3D by adding an additional rotational degree of freedom for sample alignment. This approach allows the recording of full X-ray tomograms over a range of X-ray energies, thereby providing full XANES spectra in single voxels of a sample volume. This complements the acquisition of the absorption coefficient projected along the X-ray beam direction.

This tomographic imaging technique was investigated using the ODH of ethane as an example, conducted under various chemical conditions. This chapter starts with a general introduction to this method in Sec. 6.1. The mechanism of the ODH of ethane to ethylene is presented in Sec. 6.2 and details on the catalyst synthesis and reaction conditions are described in Sec. 6.3. Finally, the results of this tomographic experiment with chemical sensitivity are summarized in Sec. 6.4.

6.1 Overview of this Experiment

In principle, the combination of X-ray microscopy with tomography offers unique opportunities for spatially resolved measurements. Here, the preceding measurement technique (see Chapter 5) was developed based on combining the spatially-resolved imaging with hard X-ray tomography, chemical contrast with coupled XANES data, and rapid acquisition of tomographic datasets at beamline P64. This concept is herein called operando XANES tomography (three spatial dimensions, time, and energy-resolution).

Usually, CT is a common technique for acquiring valuable information about catalysts under ex-situ conditions. To date, only a few in-situ studies are available in the literature, and there is an even smaller number of operando studies simultaneously measuring catalytic activity [74,75]. For a better understanding of the structural and chemical gradients in the catalyst, XANES tomography should be performed under in-situ and operando conditions. Hence, a suitable sample environment (aRCTIC, see Sec. 3.2.2) with complete control over the temperature, gas flow, and rotating the sample was used for this experiment. This setup enabled tomographic imaging of the catalyst under operando conditions [7].

In this case, the DCM was adjusted to distinct X-ray energy values around the absorption edge of the sample (see Sec. 4.2) and a full tomogram was recorded at each energy value. In this manner, each tomogram was acquired in the fly-scan mode within only 2 min and a full 3D XANES dataset comprising 105 energy values could be recorded in approximately 3.5 h utilizing the fast and high-resolution X-ray detector (see Sec. 3.1.3.1). This technique facilitated rapid tomographic XANES imaging of the catalytic microreactor and retrieval of spectroscopic information at each voxel along the Mo K absorption edge.

As a case study of this technique, a ”static” sample was selected, demonstrating minimal changes in chemical gradients, enabling the recording of an XANES tomogram over some hours. In this way, the chemical gradients within a model MoO_x/Al_2O_3 catalyst during the ODH of ethane to ethylene were investigated under ex-situ, oxidized, and operando conditions. Further details regarding this chemical reaction will be provided in the following section.

6.2 Oxidative Dehydrogenation of Ethane

Ethylene (C_2H_4) is an important compound in the field of petrochemicals and serves as a building block for the production of a wide range of important chemical products. The main process for producing ethylene is the steam cracking of hydrocarbons. The steam cracking of hydrocarbons consists of several steps as described below [76].

First of all, hydrocarbon feedstocks such as ethane, propane, butane, naphtha, or gas oils are selected, preheated, and then mixed with steam. Afterwards, the mixture is introduced into a high-temperature cracking reactor or furnace, where intense heat induces the splitting or cracking of hydrocarbon molecules into their smaller components [77]. By breaking the carbon-carbon bonds, smaller molecules such as ethylene, propylene, methane, hydrogen, and aromatics are formed and cracked products are rapidly cooled or quenched to prevent further reactions [78, 79]. To separate and purify desired products, such as ethylene, from cracked gas mixtures, various separation and purification processes are utilized.

Due to the highly endothermic nature of steam cracking, it is one of the most energy-intensive processes in the chemical industry. In this way, high temperatures necessary for operating this process are achieved through the combustion of fossil fuels, resulting in annual global emissions exceeding 300 million tons of CO_2 [77]. To mitigate the environmental impact of these reactions, it is crucial to devise strategies. This could entail replacing fossil feedstock inputs with renewable or recycled alternatives, capturing and utilizing CO_2 emissions generated during the process, or implementing more sustainable practices [77].

The direct catalytic dehydrogenation of alkanes is a potential alternative to thermal catalytic cracking used in steam crackers [76, 80]. During this procedure, a hydrocarbon, typically an alkane, is exposed to an oxidizing agent such as oxygen or air in the presence of a catalyst. Hydrogen atoms are removed from hydrocarbon molecules by the catalyst and forming unsaturated hydrocarbon products such as ethylene. Mixed metal oxides including vanadium, molybdenum, and chromium supported on oxides such as alumina, silica, and titania are typically used as catalysts in this process. Dehydrogenation offers the advantage of being a highly exothermic reaction, utilizing hydrogen as an acceptor and requiring less energy compared to the steam cracking of hydrocarbon molecules [81, 82].

In the petrochemical industry, ODH is commonly utilized for producing essential chemicals, such as ethylene (C_2H_4) from ethane (C_2H_6), propylene (C_3H_6) from propane (C_3H_8), and butadiene (C_4H_6) from butenes (C_4H_8). Successful industrial implementation of the ODH process requires a careful analysis of catalysts, reaction conditions, and economic considerations to ensure the efficient and cost-effective production of the desired unsaturated hydrocarbons. In this manner, a laboratory study of the ODH process yields valuable insights. These insights include the optimization of process parameters, the synthesis and testing of novel catalyst formulations for advancements in catalyst design applicable to industrial-scale applications and the development of kinetic models to identify key parameters before transitioning to large-scale industrial implementation.

The ODH of ethane to ethylene, as depicted in Eq. 6.1, offers an attractive one-step production route for ethylene at temperatures lower than the current industrial standard [83]. Therefore, it has been selected as a case study in the XANES Tomography imaging setup.

$$C_2H_6 + \frac{1}{2}O_2 \rightarrow C_2H_4 + H_2O, \qquad \triangle_r H^{\circ} = -104.88\,\mathrm{kJmol^{-1}}. \tag{6.1}$$

Supported MoO_x/Al_2O_3 catalysts are attractive systems for this application, however, this reaction displays strong gradients in the oxidation state and catalytic activity along the bed during periodic reduction and reoxidation processes. This characteristic renders the system an ideal test case for rapid XANES tomography, as changes in the oxidation state can be readily observed at the Mo K absorption edge. The following section outlines the experimental method and presents the results obtained from the investigation of this chemical reaction.

6.3 Experimental Details

The following section provides specific details related to the experimental parameters, encompassing aspects such as the catalyst synthesis, gas composition, flow rate, and the experimental method.

6.3.1 Catalyst Synthesis[1]

The catalyst was prepared by using the incipient wetness impregnation technique [84]. Alumina spheres with a diameter of 1 mm and a surface area of approximately $160\,m^2\,g^{-1}$ were supplied as the support catalysts (Sasol) and Ammonium Heptamolybdate Tetrahydrate ((AHM, $(NH_4)_6\ Mo_7\ O_{24} \cdot 4\ H_2O$, 99.0 %), Merck) was provided as the molybdenum precursor. Before impregnation with the Mo precursor solution, the alumina spheres were crushed and sieved to the desired particle size [79, 85].

The specified amount of AHM was dissolved in deionized water, maintaining a pH level of 5.2. In 15 - 20 steps, the support particles were impregnated with the precursor solution. Between each step, the solvent was evaporated in a rotary evaporator (40 °C, 100 mbar, 5 h). Afterwards, the catalyst was dried at 120 °C overnight and the MoO_3/Al_2O_3 powder catalysts with different particle shapes have been prepared. The catalyst calcination process took place in the reactor in synthetic airflow at a temperature within the range of 540 - 560 °C for a duration of 3 h. This step preceded the initiation of measurements.

---

[1] This part of the text was adapted and reprinted from [79].

6.3.2 Reaction Conditions

The imaging setup including the aRCTIC sample environment described in Sec. 3.2.2 was utilized in this measurement (see Fig. 3.10). The catalyst powder of MoO_3/Al_2O_3 with a 20.0 wt% MoO_3 loading and a particle size of 50 µm to 100 µm was filled into a capillary with an outer diameter of 1 mm. The particles were fixed in position with quartz wool (QW) and the length of the catalyst bed was approximately 8.5 mm. The reactor was glued with epoxy glue into the gas inlet and outlet channels on the aRCTIC setup (see Fig. 6.1).

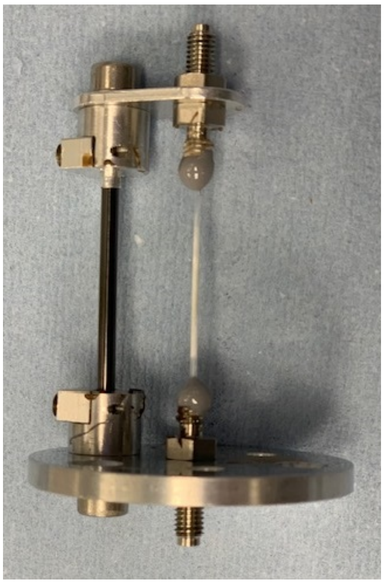

Figure 6.1: Filled quartz capillary with the catalyst powder of MoO_3/Al_2O_3 was glued on the sample holder. The capillary inlet was located at the top of the setup.

The sample was investigated under three different conditions: i) ex-situ, ii) fully oxidized, and iii) operando conditions.

In the ex-situ condition, the Mo catalyst was analyzed at room temperature under a flow of O_2/N_2 gases. In this case, the catalytic particles are white in color. In the oxidized condition in the presence of a flow of O_2/N_2 gases, the catalyst was heated up from room temperature up to 490 °C in the step of 50 °C and the temperature was measured with thermocouples attached to the nozzle of the air blowers. At 490 °C, the catalyst color turned to yellow. Under the operando condition for ODH of ethane, a gas mixture of ethane, oxygen, and as diluent a mixture of He in N_2 was provided as reactants. The information regarding the species, compositions, and flow rate of gases under various conditions is provided in Table 6.1.

Condition	**Species**	**Gas Composition**	**Flow rate** [mL min^{-1}]
ex-situ	O_2, N_2	20/80	0.5
oxidized	O_2, N_2	20/80	0.5
operando	C_2H_6, O_2, N_2	11.5/11.5/77	0.26

Table 6.1: Gases utilized under various conditions during the ODH of ethane reaction.

Fig. 6.2 illustrates the synthesized material under both ex-situ (a) and operando (b) conditions. The color gradient observed along the vertical axis of the catalyst bed in Fig. 6.2 (b) signifies the changing chemical state of the catalyst, transitioning from gray (oxidized at the inlet) to black (reduced at the outlet).

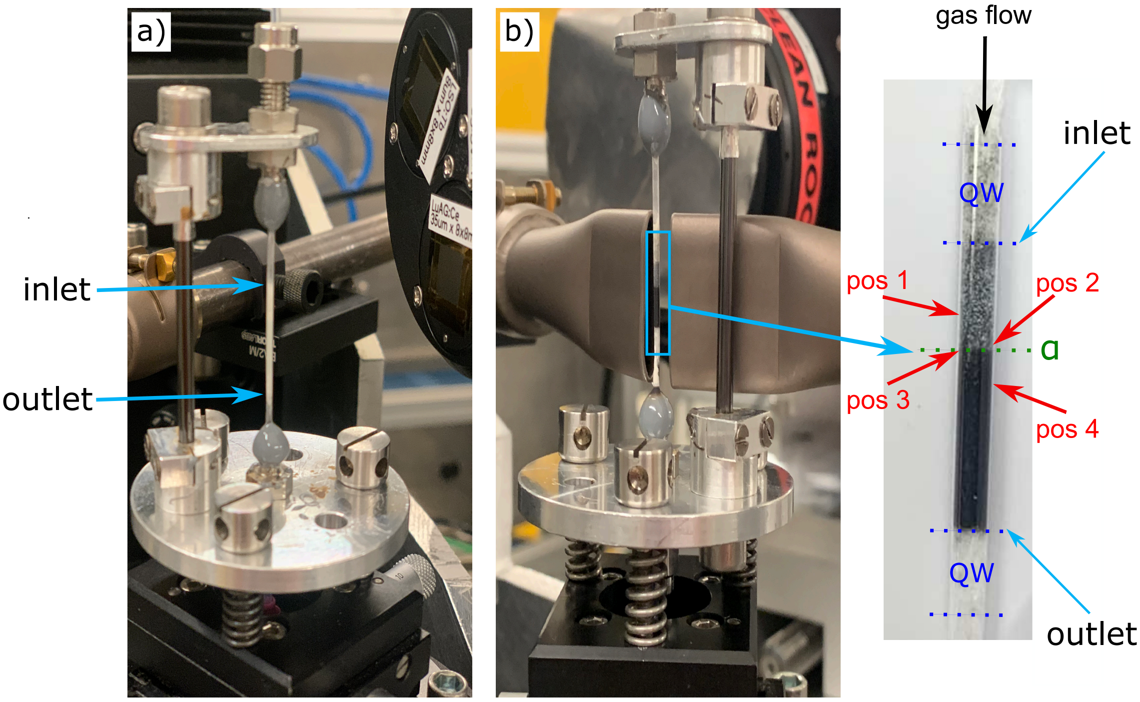

Figure 6.2: The 20.0 wt% MoO_3 supported on γ-Al_2O_3 was fixed in position with quartz wool inside the reactor. (a) At room temperature under the ex-situ condition, the Mo catalysts had a white color, indicating the presence of the orthorhombic α-MoO_3 [85, 86]; (b) During the operando condition, the color gradient inside the catalyst bed was visible from top (gray color) to bottom (black color) along the flow direction. The α (green dotted line) indicates the inflection point where the oxidation state of the catalyst changed. At specified positions along the catalyst bed, full XANES tomograms were recorded. The pos 2 and pos 3 were selected close to the α.

The chemical reactants and products of the reaction under different conditions were analyzed online by GC connected to the gas outlet of the catalytic reactor.

It is important to note that, to protect the detector from the high temperature surrounding the sample under oxidized and operando conditions, a piece of aluminum foil was placed in front of the X-ray camera. Also, the setup was checked for leaks to ensure gas tightness before beginning the experiments.

6.3.3 Tomography XANES Imaging During ODH of Ethane

The full X-ray tomogram of the capillary was measured by recording a set of 1000 projections in about 2 min over an angular range of 180° at each energy point (see Fig. 4.2). In total, 105 tomograms were captured at different energies around the Mo K absorption edge in about 3.5 h. The experimental procedure for recording each full XANES tomogram and the energy range of the recorded tomogams are described in more detail in Sec. 4.2.

At ex-situ and oxidized conditions, the full 3D XANES dataset was recorded in the middle of the catalyst bed. As a color gradient from gray to black along the vertical axis of the catalyst bed under the operando condition was observed (see Fig. 6.2 (b)), four full 3D XANES data sets at different positions along the catalyst bed were recorded. These positions are shown in Fig. 6.2. The pos 1 and pos 4 refer to the beginning and end of the catalyst bed, where the Mo catalyst was partially oxidized and fully reduced, respectively. The pos 2 and pos 3 were selected close to the inflection point (α, the transition region between the oxidized and reduced areas) in the middle of the catalyst bed in order to investigate the changes in the oxidation state of the catalyst. The reason for the apparent color gradient from gray to black along the vertical axis of the catalyst bed will be discussed in the following.

In this configuration, the image area captured by the X-ray camera had a size of 1.33 mm × 1.33 mm (see Sec. 3.2.2). It is important to note that this chemical reaction was brought to a steady state during the recording of full 3D XANES tomograms at different heights along the catalyst bed under the operando condition as confirmed by analysis of the gas phase products by GC. This ensures that tomograms were recorded under stable conditions and remained relatively constant throughout the measurement of each projection series. To attain a comprehensive 3D representation of the catalyst bed and examine variations in the Mo oxidation state, the recorded projections under each condition were processed using self-developed data processing methods outlined in Sec. 4.2.

6.4 ODH Results

Results of the data processing for recorded full 3D XANES datasets are presented in the following.

6.4.1 Tomography XANES Imaging Data

As explained in the Chapter. 4 (see Sec. 4.2.1), computational binning of images by a factor of 2 × 2 was employed during data processing. This was done due to the high level of noise observed in individual pixels. Afterwards, dark- and flat-field corrected absorption images were calculated by applying the Lambert-Beer law to all recorded projections (see Sec. 4.1.2). A representative example of it is shown in Fig. 6.3. This projection was recorded at an X-ray energy of 20.0 keV in a rotation angle of 5.38°.

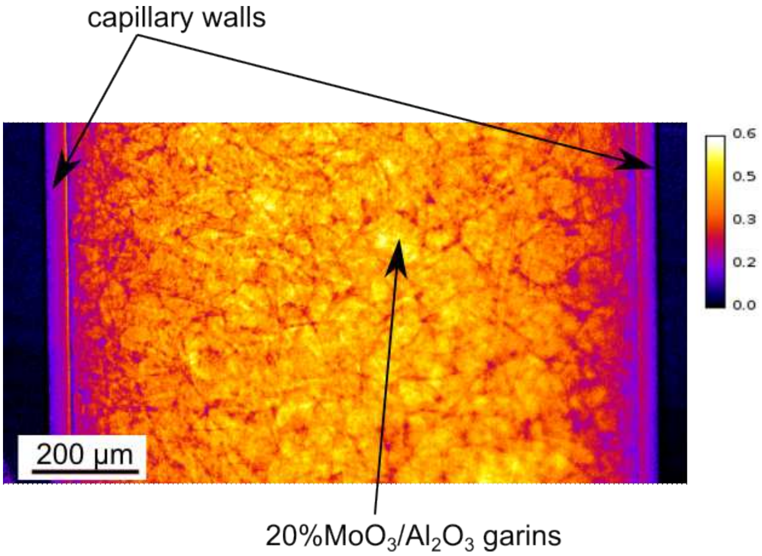

Figure 6.3: Dark- and flat-field-corrected 2D absorption image of the glass capillary containing the 20.0 wt% MoO_3/Al_2O_3 catalyst at an X-ray energy of 20.0 keV under ex-situ condition.

After the alignment of the projections (see Sec. 4.2.4), the data were reconstructed (see Sec. 4.2.5). An example of a reconstructed slice is shown in Fig. 6.4.

As the reconstructed 3D volume is represented as a grid of voxels (volumetric pixels), where each voxel corresponds to a small volume element within the reconstructed object, the XANES spectrum of each voxel provides the chemical state of the Mo catalyst at each voxel. In this way, by sorting each slice from each reconstructed

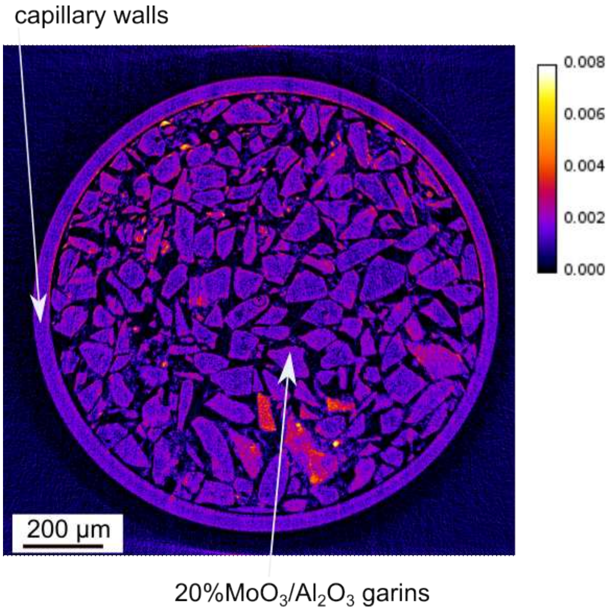

Figure 6.4: Single slice of the reconstructed 3D volume measured at an X-ray energy of 20.0 keV under ex-situ condition.

tomogram, where each tomogram was measured as a function of energy, the XANES spectrum was obtained for every voxel within each slice (see Sec. 4.2.6).

As an example of it, a sequence of a specific slice measured as a function of X-ray energies under ex-situ condition is shown in Fig. 6.5(a) - 6.5(f). Results indicate that at energies below the Mo K absorption edge ($E = 20\,\text{keV}$), the absorption was very low. Afterwards, the absorption increased along the edge and then decreased again above the edge as the X-ray energy increased. This behavior corresponds to the Mo XAS spectra as illustrated in Fig. 2.8. At the edge position, the bright spots are indicative of greater absorption and more oxidized Mo particles. To extract information about the chemical state of Mo particles in this slice, three ROIs were selected and their positions are shown in Fig. 6.5(g). By averaging signals from these ROIs, the XANES spectrum corresponding to this slice was derived and is illustrated in Fig. 6.5(h).

To determine the oxidation state from the XAS spectra, the LCA data fitting process (see Sec. 4.2.7) was performed for each voxel within every slice. In this measurement, two datasets, illustrated in Figs. 6.6 - 6.7, served as reference spectra for the data fitting process. The selection of the appropriate reference spectrum for data fitting was based on the chemical conditions of the measurement.

In the first dataset, orthorhombic MoO_3 and monoclinic MoO_2 corresponding to Mo(VI) and Mo(IV) were utilized as reference spectra for the data fitting of the

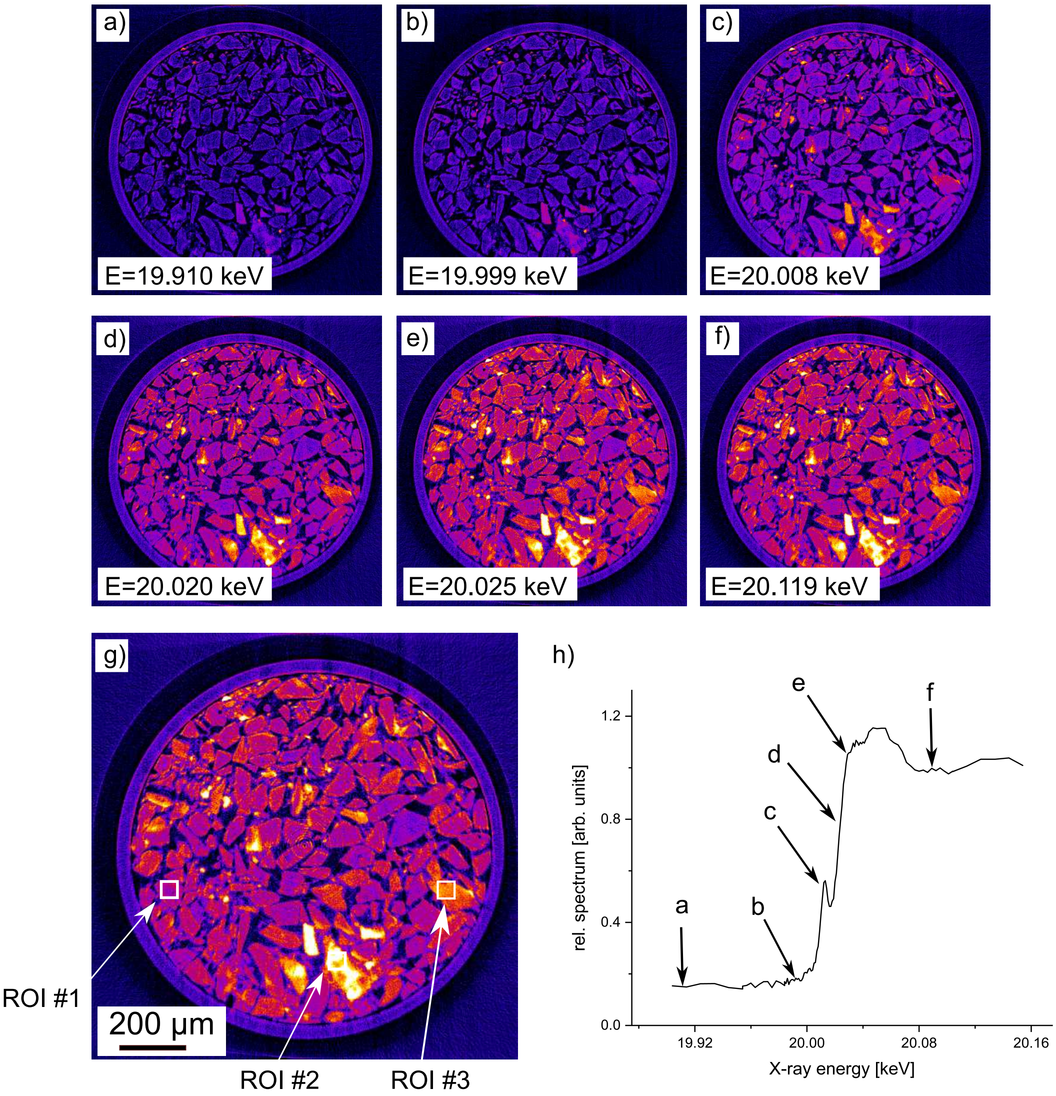

Figure 6.5: (a)-(f) A specific slice of the reconstructed tomograms as function of energy under ex-situ condition; (g) These three ROIs were selected for extracting a XANES spectrum; (h) The XANES spectrum, derived from averaging over these three ROIs, indicates that Mo was fully oxidized.

recorded full 3D XANES datasets under both ex-situ and oxidized conditions. These spectra were considered from the results of measurement by Wollak, et al. [85]. The normalized reference spectra are shown in Fig. 6.6.

In the second dataset, two regions near the inlet and outlet of the catalyst bed under operando condition were selected. The extracted spectra from these regions were considered as the oxidized and reduced reference spectra in the LCA data fitting process of the recorded full 3D XANES datasets under operando condition. The normalized reference spectra are shown in Fig. 6.7.

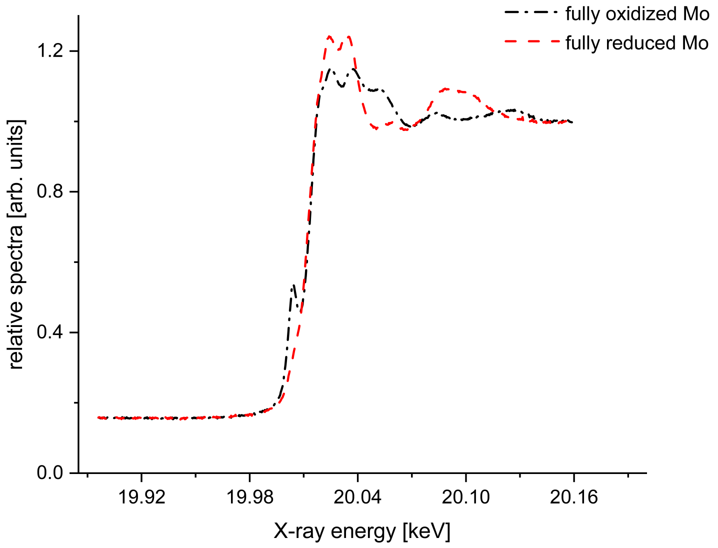

Figure 6.6: Reference spectra of orthorhombic MoO_3 and monoclinic MoO_2 corresponding to Mo (VI) and Mo (IV) are shown in black and red, respectively. These were utilized for the LCA data fitting process of recorded full 3D XANES datasets under ex-situ and oxidized conditions.

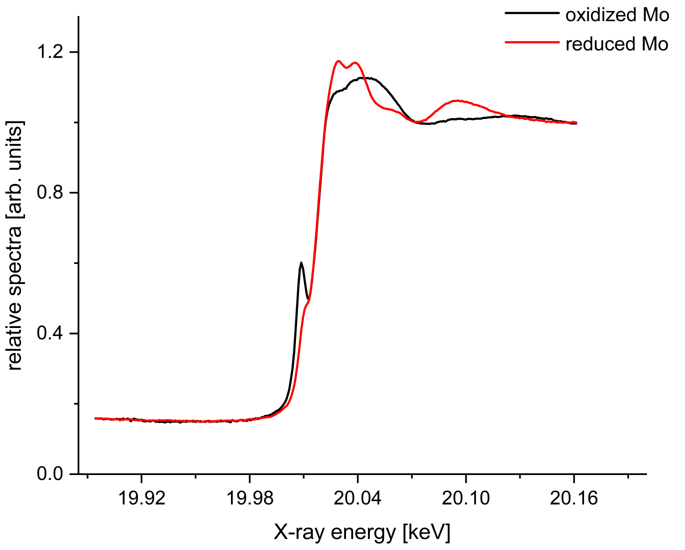

Figure 6.7: Reference spectra corresponding to MoO_3 and MoO_2 under the working condition are depicted by black and red lines, respectively. These were utilized for the LCA data fitting process of recorded full 3D XANES datasets under operando conditions.

The spectra were obtained under operando condition as reference spectra (see Fig. 6.7) are different from the orthorhombic MoO_3 and monoclinic MoO_2 spectra (see Fig. 6.6). This discrepancy arises because the reference samples are highly crystalline MoO_3 and MoO_2, while the sample under the operando condition consists of mixed oxides with other transition metals.

By employing Eq. 4.6 and utilizing appropriate reference spectra corresponding to the measurement condition, LCA data fitting was performed for each voxel in the recorded full 3D XANES datasets under various chemical conditions, providing information about the local Mo oxidation state. As an example, Fig. 6.8 displays the LCA data fitting for the specific slice of the reconstructed 3D volume shown in Fig. 6.5 under ex-situ conditions.

Here, the first datasets of reference spectra (see Fig. 6.7) were employed for data fitting. The fitting coefficients a and b (see Eq. 4.6) correspond to the amount of the oxidized and reduced Mo, respectively, as illustrated in Fig. 6.8(a) - 6.8(b). The constant offset in the absorption spectrum, which is not related to Mo, is taken into account by the parameter c as shown in Fig. 6.8(c). Under this chemical condition, only the oxidized Mo particles were visible (see Fig. 6.8(a)).

I measured the projected absorption coefficient on the detector, which can be derived from the Lambert-Beer-Law equation (see Eq. 2.10) as the following:

$$\ln \frac{I_0}{I} = \mu \Delta z \tag{6.2}$$

Since μ is in units of $[\frac{1}{voxel\ size}]$, the $\mu\ \Delta z$ results in a dimensionless value. As I measured $\mu\ \Delta z$ in the reconstruction process and applied LCA data fitting to each voxel in the reconstructed 3D volume, the resulting values from the fitting process are dimensionless.

The XANES spectra from two individual voxels of this slice are illustrated in Fig. 6.8(d) - 6.8(e) with the triangle symbol and their respective LCA fitting spectra are represented by the dashed line. The quality of the data fitting was evaluated similarly to the previous measurement by calculating the signal-to-noise ratio in each voxel (using Eq. 4.7), as shown in Fig. 6.8(f). This plot illustrated that the R-factor varied between 0.0 and 1.2 with the highest values in areas of air and low imaging contrast, i.e., in areas with less Mo. In the presence of Mo content within the capillary, the R-factor exhibited a range between 0.0 and 0.09.

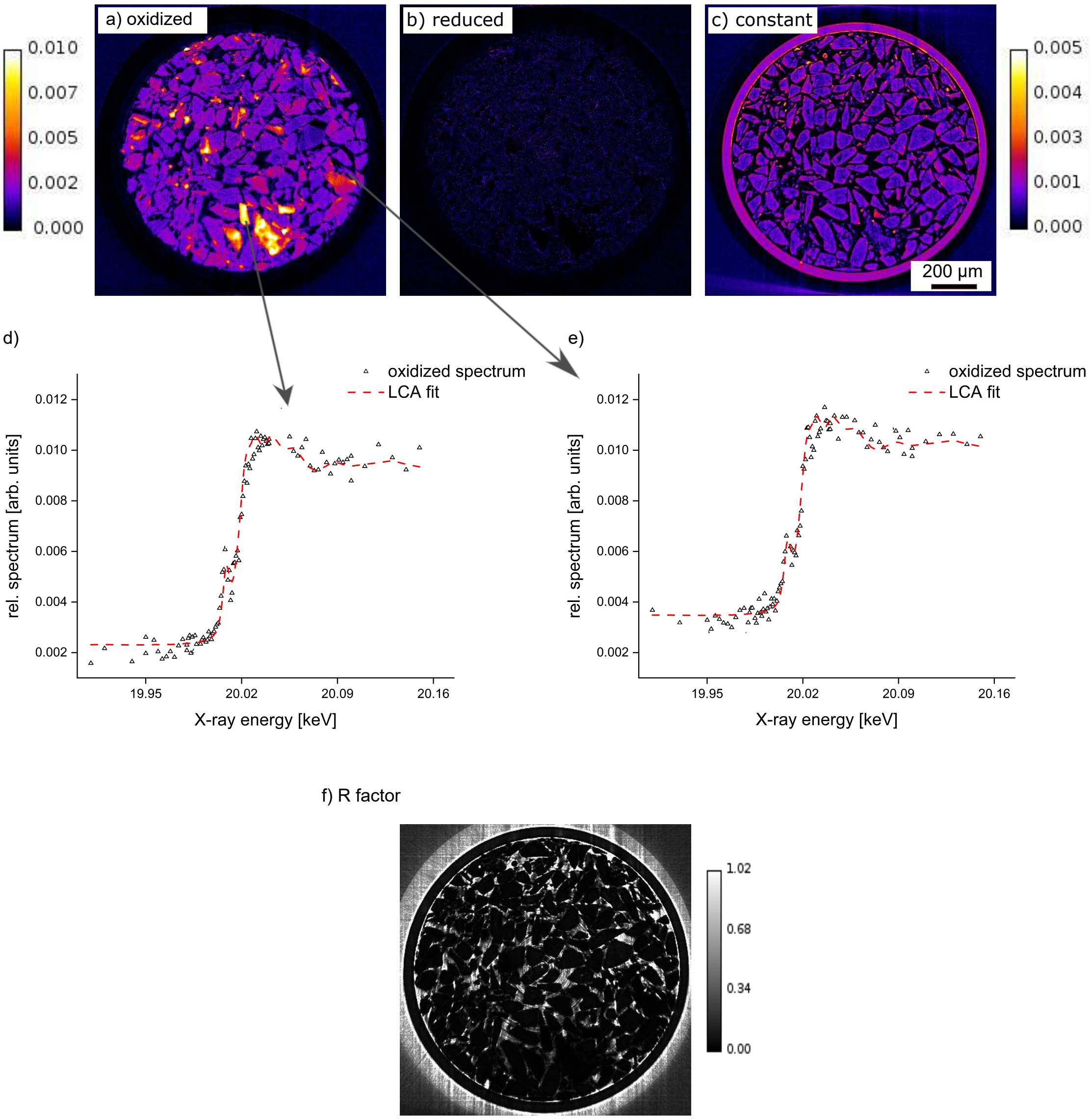

Figure 6.8: (a) Amount of oxidized Mo; (b) Amount of reduced Mo; (c) Distribution of other materials measured under the ex-situ condition. Since the glass capillary did not contain any Mo, it is only visible in this image; (d, e) Single XANES profiles were extracted from two voxels of the image and LCA data fitting of them; (f) The R-factor map showed differences in fit quality according to the amount of Mo in each voxel.

The spatial resolution in this measurement was determined using FRC. By analyzing two oxidized or reduced Mo images, obtained through LCA data fitting of the reconstructed images, the spatial resolution was obtained approximately 4.9 µm which is depicted in Fig. 6.9(a). Additionally, through the examination of two reconstructed projections from distinct energy scans at 19.900 keV and 19.910 keV and calculating spatial resolution through FRC (see Fig. 6.9(b)), the result indicates the overall high quality of the normal tomogram.

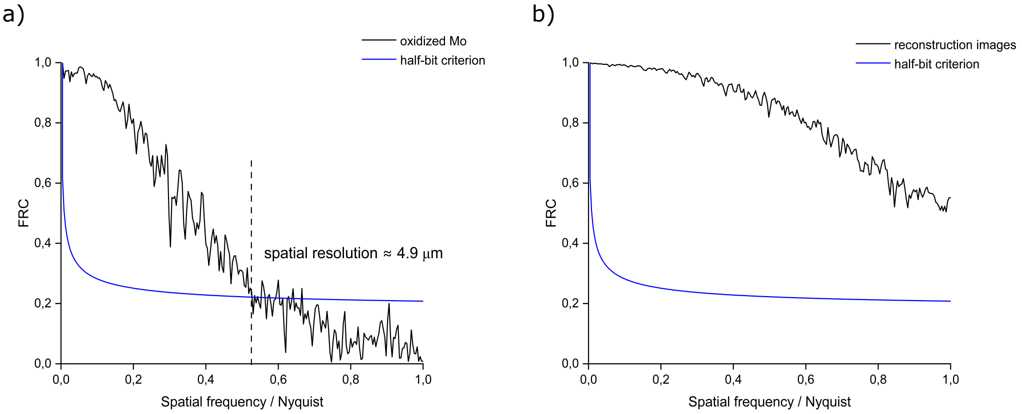

Figure 6.9: FRC analysis and the half-bit criterion with the estimated spatial resolution in the oxidized Mo distribution under operando condition (a) and reconstructed images (b).

Indeed, the upgrade of the scintillators in the high-resolution X-ray detector for this measurement (see Sec. 3.1.3.1) resulted in a significant improvement in spatial resolution in this measurement compared to the previous experiment.

Detailed results of the analyzed recorded full 3D XANES datasets under various conditions during the ODH of ethane are presented in the following.

6.4.2 Ex-situ Condition

The full 3D XANES tomogram was recorded in the middle of the catalyst bed under ex-situ condition. Representation of the reconstructed 3D volume at a specific energy (E = 20.0 keV) is shown in Fig. 6.10.

As this volume consisted of 212 slices and the height of each voxel was 2.6 µm, the 551.2 µm of a total length of the catalyst bed was examined in this measurement. The oxidation state of Mo for each voxel in every slice of the reconstructed data was established by employing LCA data fitting and utilizing the first datasets of the reference spectra (see Fig. 6.6). Results of LCA data fitting for several slices at different heights of the catalyst bed (see Fig. 6.10) are shown in Fig. 6.11. Similar to the previous measurement, the results of LCA for each slice are illustrated in two images, with the upper and lower images representing the amounts of oxidized and reduced Mo, respectively. Observations of Mo species exclusively only in the first row of different slices indicated that the catalyst bed had been completely oxidized under

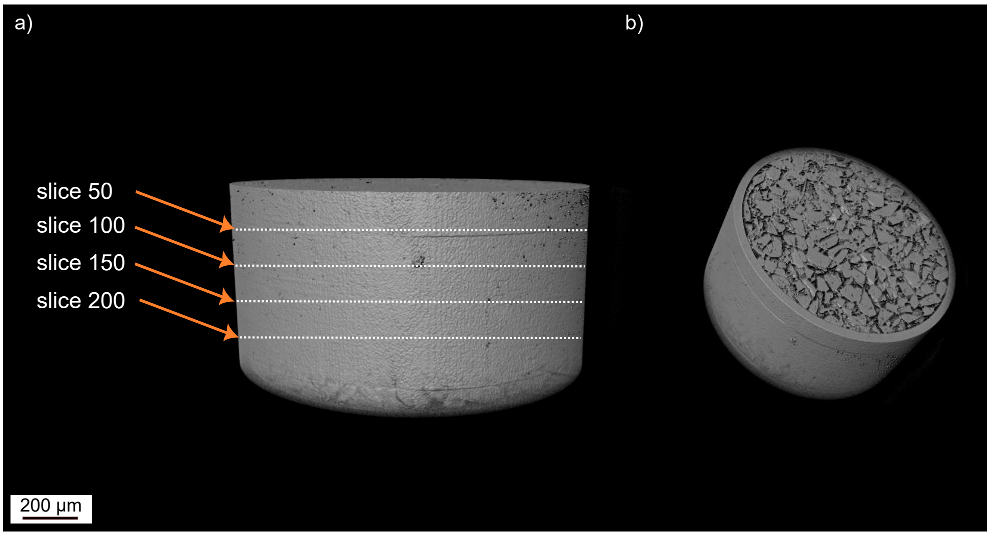

Figure 6.10: (a) Tomographic reconstruction of the Mo catalyst embedded in the capillary. Data were measured at the X-ray energy of 20.0 keV under ex-situ condition; (b) 3D rendering of the reconstructed 3D volume.

this chemical condition with no observed reduced Mo particles in the second row.

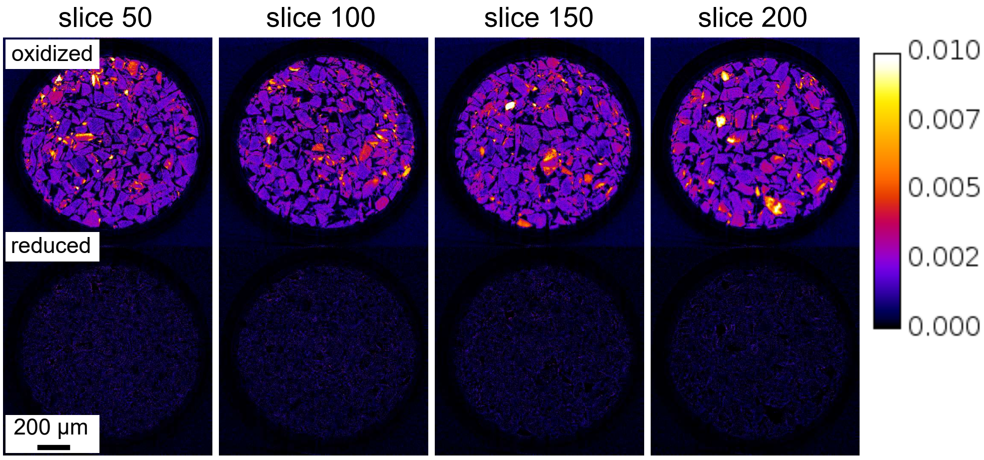

Figure 6.11: Ex-situ condition: Distribution of oxidized Mo (upper images) and reduced Mo (lower images) at several heights along the catalyst bed. These heights are shown in the reconstructed 3D volume in Fig. 6.10.

To enhance the visual representation of the distributions of oxidized (a coefficient, Eq. 4.6) and reduced (b coefficient, Eq. 4.6) Mo particles obtained from LCA data fitting, 3D volume renderings for each coefficient were generated for the entire reconstructed volume using Avizo (see Sec. 4.2.8). The volume rendering of the amount of oxidized particles (red-yellow) is shown in Fig. 6.12.

Due to the complete oxidation of the catalyst bed under this chemical condition, the

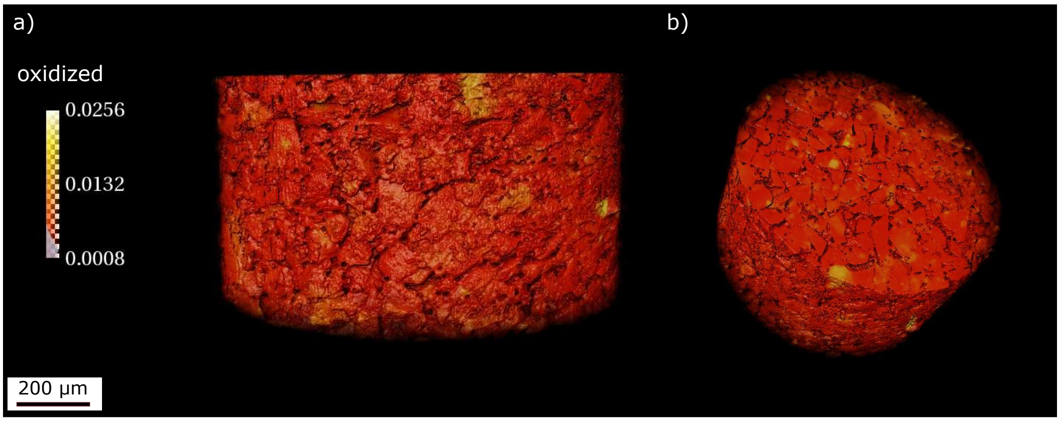

Figure 6.12: Ex-situ condition: (a) The volume rendering of oxidized Mo catalysts as determined by LCA data fitting; (b) 3D rendering of oxidized Mo. The red to yellow color bar indicates the % content of the oxidized particle.

3D rendering of reduced Mo was not visible here.

6.4.3 Oxidized Condition

After thermally stabilizing the catalyst bed under oxidized condition, the catalyst changed its color to yellow. Afterwards, the complete XANES tomogram was recorded in the middle of the catalyst bed. In this measurement, the reconstructed volume consisted of 150 slices, covering a total length of 390 µm within the catalyst bed.

LCA data fitting was performed for the reconstructed volume by considering the first datasets of reference spectra (see Fig. 6.6). Results of several slices at different heights of the catalyst bed are shown in Fig. 6.13. Since only oxidized Mo particles were visible, it indicates that the catalyst bed was fully oxidized under this chemical condition.

Fig. 6.14 illustrates the volume rendering of the amount of oxidized particles for the whole reconstructed volume.

6.4.4 Operando Condition

Under this chemical condition, a color gradient from gray to black (see Fig. 6.15) is observed along the axial position of the catalyst bed in the direction of the gas flow. To emphasize the manifestation of this color gradient, four full 3D XANES tomograms were recorded around the Mo K absorption edge at various heights

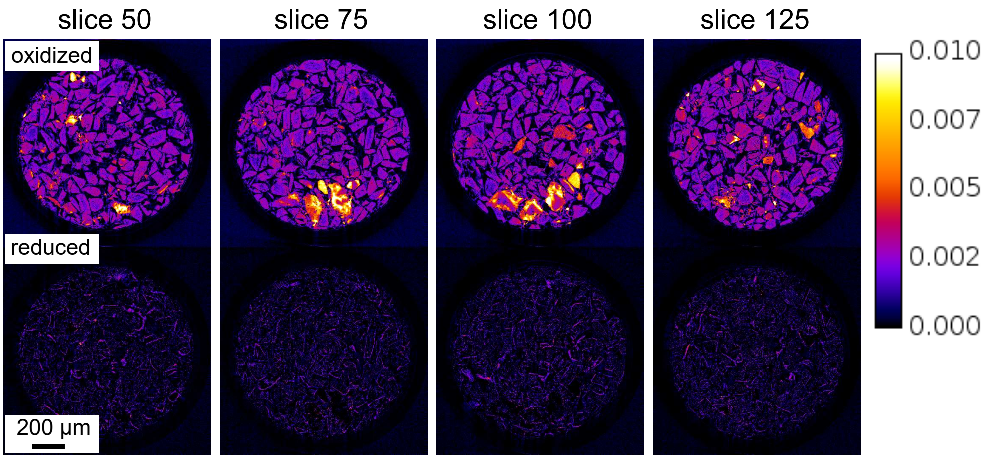

Figure 6.13: Oxidized condition: Distribution of oxidized Mo (upper images) and reduced Mo (lower images) at several heights along the catalyst bed.

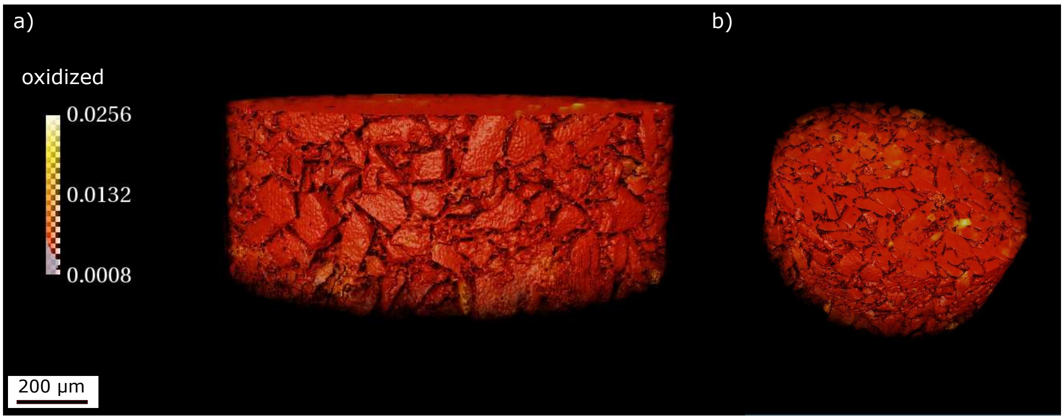

Figure 6.14: Oxidized condition: (a) The volume rendering of oxidized Mo catalysts as determined by LCA data fitting; (b) 3D rendering of oxidized Mo. The red to yellow color bar indicates the % content of the oxidized particle.

(positions) along the catalyst bed: i) close to the inlet (pos 1, black region), ii) middle (pos 2, orange region), iii) middle (pos 3, green region), and iv) close to the outlet (pos 4, red region), as depicted in Fig. 6.15.

According to Fig. 6.15, the recorded tomogram at pos 2 overlaps with the recorded tomogram at pos 3 by approximately 455 µm, and the recorded tomogram at pos 3 overlaps with the recorded tomogram at pos 4 by approximately 145.6 µm. The gap between the recorded full 3D XANES dataset at pos 1 and pos 2 was approximately 196.8 µm. The details of each recorded tomogram, including the number of slices and the measured length of the catalyst bed, are available in the table below.

LCA data fitting was conducted for these four recorded full 3D XANES tomograms

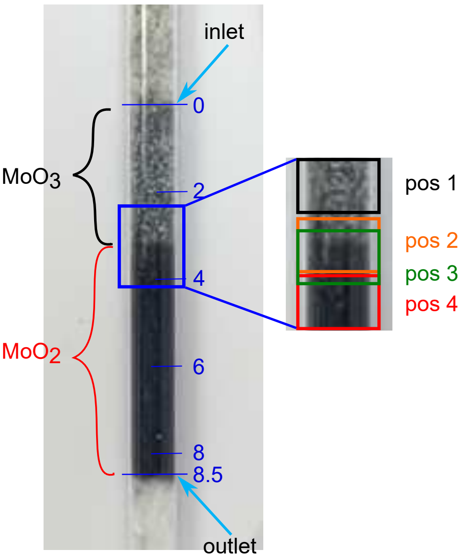

Figure 6.15: The length of the catalyst bed was 8.5 mm. Under operando condition, four full 3D XANES tomograms were recorded along the total length of the catalyst bed. The recorded regions are depicted along the catalyst bed with labels pos 1, pos 2, pos 3, and pos 4. The details about the measured length in each region are provided in Table. 6.2.

Position	**Number of slice**	**Measured length** [µm]
pos 1	221	574.6
pos 2	245	637
pos 3	245	637
pos 4	250	650

Table 6.2: The information regarding the total measured length of the catalyst bed in each recorded tomogram.

under this chemical condition, utilizing both datasets shown in Figs. 6.6 - 6.7 as reference spectra. Fig. 6.16 illustrates the LCA results for slices at various heights in each recorded position, using reference spectra in Fig. 6.7.

In pos 1, close to the beginning of the catalyst bed, the color of the MoO_3 catalyst was gray (see Fig. 6.15). At this position (see the first row in Fig. 6.16), a higher concentration of oxidized Mo and a lower concentration of reduced Mo are visible. The MoO_3 is the transition metal oxide catalyst that facilitates the exchange of oxygen atoms between its lattice and oxygen present in the surrounding gas phase [87]. In fact, this lattice oxygen, nucleophilic oxygen, participates in the ODH reaction by removing hydrogen from ethane molecules and yielding ethylene. The optical properties of Mo oxides undergo significant changes depending on the concentration

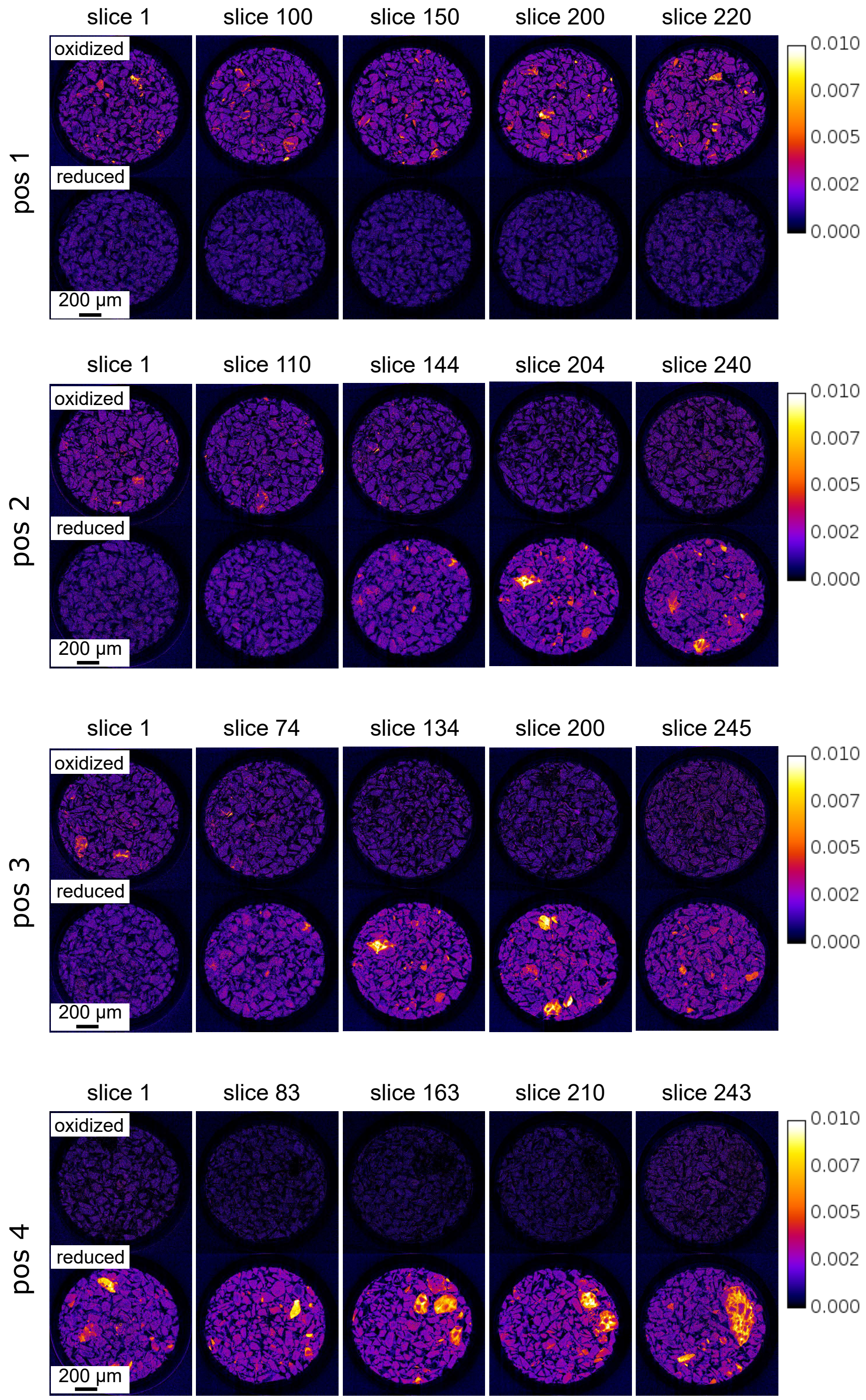

Figure 6.16: Operando condition: Distribution of oxidized Mo (upper images) and reduced Mo (lower images) at various heights in each recorded tomogram along the catalyst bed. This fitting was performed using the reference spectra in Fig. 6.7.

of oxygen vacancies which is influenced by thermodynamic factors, particularly the oxygen partial pressure [88]. During operation conditions, the concentration of these vacancies increases as the oxygen partial pressure decreases in comparison to the oxidized condition. In this way, the catalyst's color changes rapidly from yellow color under oxidized condition to a darker color (gray color at the inlet) during operando conditions due to a presence of partially oxidized MoO_3 with a minimal quantity of reduced MoO_2 at this position [79, 89].

In pos 2, close to the transition region from the gray color region (partially oxidized region) to the black color region (reduced region), the results indicate that in the upper slices (slices 1 and 110), the catalyst bed was predominantly filled with partially oxidized Mo catalyst, with smaller amounts of reduced catalyst (see the second row in Fig. 6.16). Suddenly, a greater amount of reduced catalyst was observed in the middle slice (slice 144) of this position. Specifically, from slice 144 to the last slice (slice 240) at this position, a significant increase in the amount of reduced Mo catalyst was evident, attributed to a decrease in the amount of partially oxidized Mo.

In pos 3, near the transition region, the results indicate a similar pattern to pos 2. From the first slice up to slice 74, a smaller amount of reduced Mo particles becomes visible (see the third row in Fig. 6.16). Suddenly, a partial reduction of Mo particles is observed from slice 74 to slice 245 at this position. As the oxygen partial pressure declines from the inlet of the catalyst bed into its outlet, the reduction of the Mo particles started from slice 74 at the position and from slice 144 at pos 2. Below a certain oxygen partial pressure, the catalyst's structure became unable to offset or compensate for the presence of oxygen vacancies [79]. In this way, structural changes are induced rapidly with the reduction of the MoO_3 into the MoO_2 in the direction of the gas flow and the catalyst became darker.

In pos 4, near the outlet of the catalyst bed, LCA data fitting results indicate a lower amount of oxidized Mo, as expected, and a significant quantity of reduced Mo particles (see the last row in Fig. 6.16). Due to the very low oxygen vacancy concentration at the end of the catalyst bed compared to the beginning and the middle of the catalyst bed, the large amount of Mo particles located in this position were reduced to MoO_2 particles [79]. This characteristic signifies variations in the oxidation state of the Mo catalyst in response to the concentration of oxygen vacancies within the catalyst bed under operando conditions which this imaging technique facilitated the identification of them.

As previously mentioned, the recorded full 3D XANES tomograms in pos 2 and pos

3 overlapped with each other. The LCA data fitting of corresponding slices from these positions is identical (see Table 6.3) and are visible in Fig. 6.16.

	pos 2	**pos 3**
slice	144	74
slice	204	134

Table 6.3: Similar slices at pos 2 and pos 3.

To enhance the visualization of the amount of oxidized and reduced particles obtained from the LCA data fitting for these recorded four tomograms, the volume rendering was performed using Avizo and is shown in Fig. 6.17.

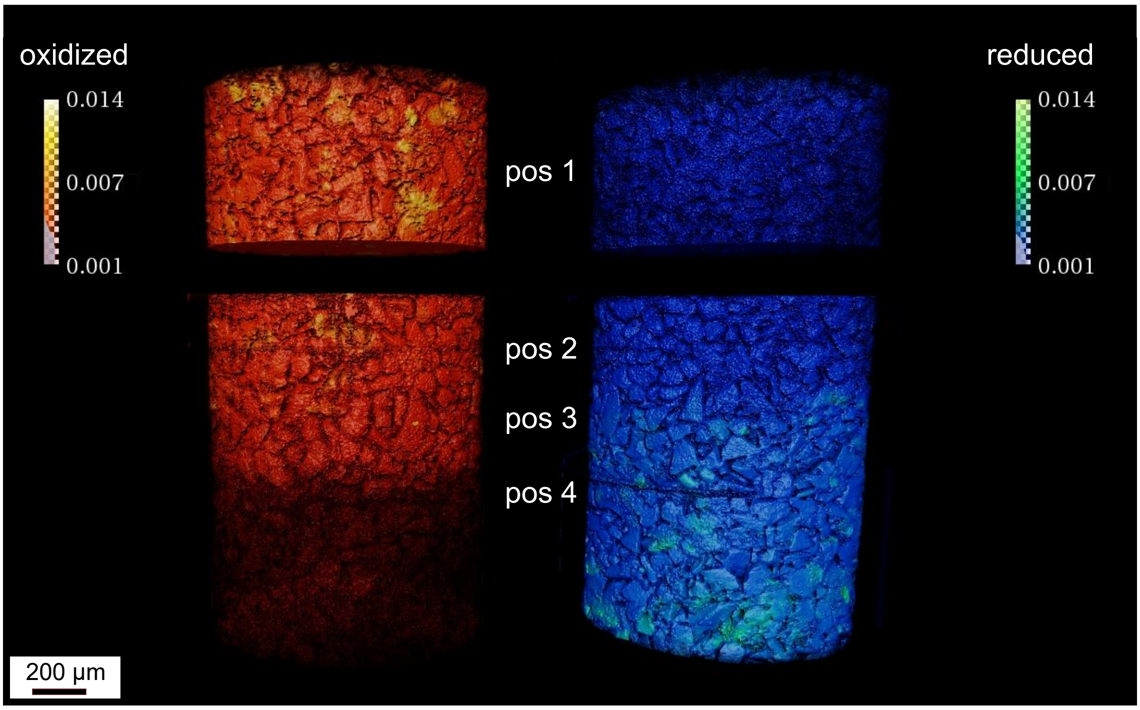

Figure 6.17: Operando condition: The volume rendering of the amount of oxidized and reduced Mo particles along the catalyst bed. The red to yellow color bar indicates the % content of the oxidized particles. The blue to green color bar indicates the % content of the reduced particles. It is derived from LCA data fitting of all slices, considering the reference spectra presented in Fig. 6.7. The approximate region of each recorded position is illustrated here.

The 3D rendering of the amount of oxidized material along the total measured length of the catalyst bed (recorded four positions) is presented on the left side of Fig. 6.17 in the red-yellow color. On the right side of Fig. 6.17, the 3D rendering of the amount of reduced material along the total measured length of the catalyst bed is displayed in the blue-green color. The gap between recorded tomograms in pos 1 and pos 2 is visible in this figure.

In this figure, a high concentration of MoO_3 is visible at pos 1 in comparison to the other positions. Moving from the pos 1 towards the outlet of the catalyst bed, the amount of oxidized particles decreases. In contrast to the concentration of oxidized particles along the catalyst bed, the amount of reduced particles increases from the inlet into the outlet due to a gradual reduction of the Mo particles. Indeed, at pos 4 fully reduced MoO_2 particles and a smaller amount of oxidized MoO_3 particles are visible. The inflection point, indicating the transition from the partial oxidized region to the reduced region, is clearly evident.

To understand the fluctuations in the quantities of oxidized and reduced particles throughout the entire length of the measured catalyst bed, the average values of them for each slice in every recorded position were calculated from the selected region (see Fig. 6.18(a)) in each slice. In Fig. 6.18(b), these values were then plotted as a function of the measured length of the catalyst bed which was 2.1 mm. At a height of approximately 1.1 mm, a distinct transition point between the reduced and oxidized regions becomes evident.

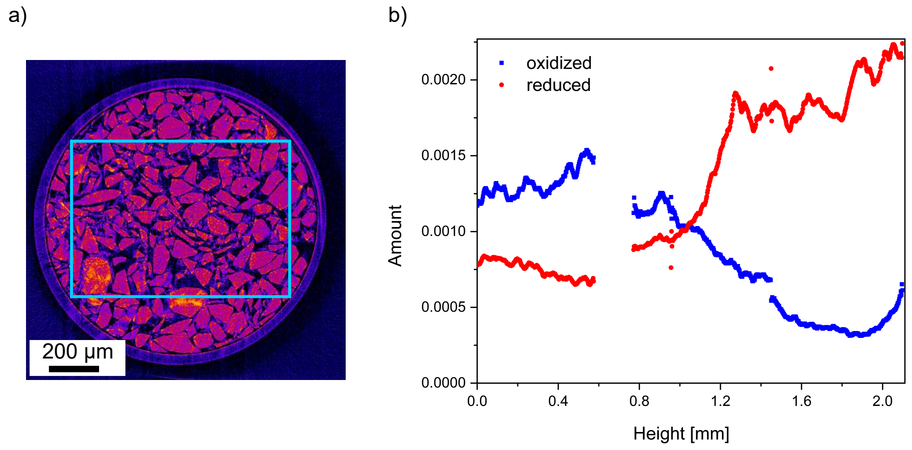

Figure 6.18: Distribution of the amount of oxidized and reduced Mo along the measured length of the catalyst bed. (a) Distributions are taken by averaging in amount of the oxidized and reduced particles from the blue region in all slices; (b) Blue squares represent the oxidized Mo and red bullets represent the reduced Mo particles at each height.

In order to gain insight into the shape of XANES spectra at different heights (slices) of pos 3, three ROIs were selected in marked reconstructed slices (see Figs. 6.19(a)

- 6.19(d)) and XANES spectra were obtained by averaging over these ROIs. The normalized XANES spectra of these slices are shown in Fig. 6.19(e).

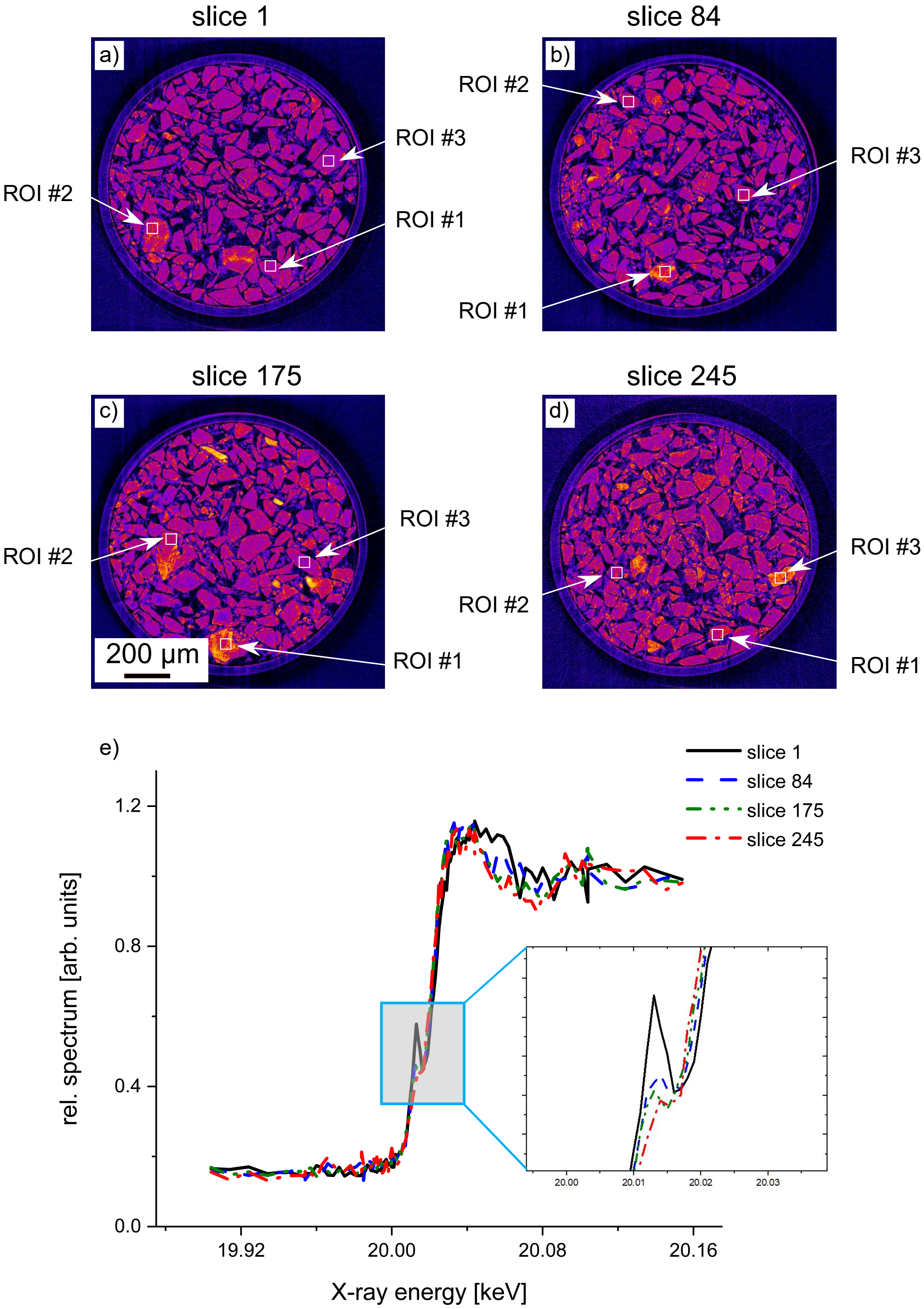

Figure 6.19: Operando condition: (a)-(d) Reconstructed slices at the X-ray energy = 20.02 keV with marked ROIs at pos 3; (e) Normalized XANES spectra derived from these ROIs for different slices (heights) along the catalyst bed at this measured position.

The XANES spectrum extracted from slice 1 exhibits the same features and edge position as the MoO_3 oxidation state in Fig. 6.7. This spectrum indicated that Mo was in the oxidized chemical state at this point. On the other hand, the pre-edge and white line shapes of the XANES spectrum measured at slice 245 are similar to the MoO_2 oxidation state, indicating the presence of reduced Mo at this height of the catalyst bed. The XANES spectra of slices 84 and 175 reveal a gradual decrease in the pre-edge in comparison to the XANES spectrum of slice 1. This observation confirms that by moving from the upper heights (inlet) into the lower heights (outlet) and decreasing the concentration of oxygen, the oxidation state of Mo particles was gradually homogeneously reduced from the oxidized form to the reduced form. Around the inflection point, the XANES spectra (spectra slices 84 and 175) are linear combinations of the oxidized and reduced spectra.

The LCA data fitting for the recorded full 3D XANES datasets was conducted using the reference spectra shown in Fig. 6.6 as well. The 3D rendering of the amount of oxidized and reduced particles along the entire measured length of the catalyst bed is illustrated in Fig. 6.20.

It can be seen in this figure that the amount of oxidized particles decreases from pos 1 to pos 4, in which less amount of MoO_3 particles are visible at pos 4, particles are darker in comparison with other positions. Moreover, the reduced MoO_2 particles are observable solely at positions 3 and 4.

As shown in Fig. 6.17, where reference spectra of the sample were used in LCA data fitting (see Fig. 6.7), oxidized MoO_3 particles were not visible at position close to the outlet of the catalyst bed (pos 4) and less amount of the reduced MoO_2 particles were observed near the inlet (pos 1) and specific amounts of the reduced particles near the transition region (pos 2). These results are different from the volume rendering shown in Fig. 6.20 demonstrating the presence of oxidized MoO_3 particles at pos 4, whereas there are no reduced MoO_2 particles at pos 1 and pos 2.

When utilizing the reference spectra presented in Fig. 6.6 for LCA data fitting, the results indicate everything seems ideal completely oxidized and reduced (see Fig. 6.20). In contrast, applying the reference spectra obtained from the inlet and outlet of the catalyst bed under operando condition (see Fig. 6.7) in LCA data fitting, reveals everywhere is the mixture of the two Mo species and probably some intermediate species (see Fig. 6.17). The range of different concentrations of these species is represented by the beginning and end of the reactor. In fact, this dataset reflects dynamic changes from the start to the end points. Compared to the first

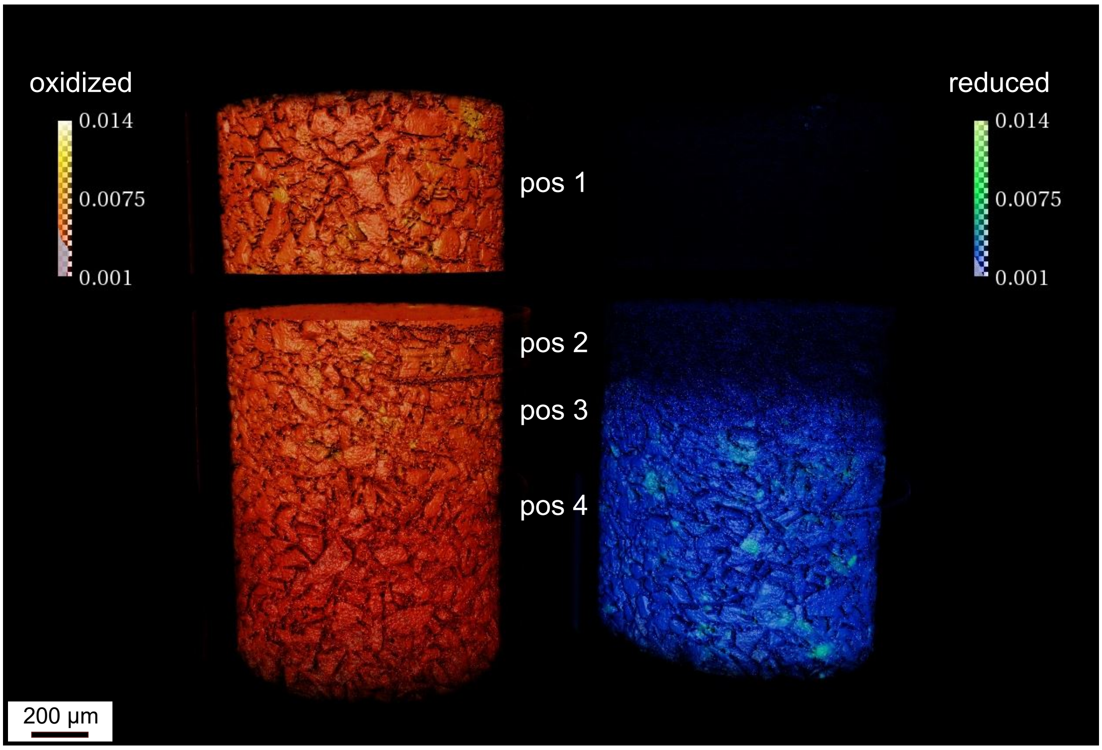

Figure 6.20: Operando condition: The volume rendering of the amount of oxidized and reduced Mo particles along the catalyst bed. The red to yellow color bar indicates the % content of the oxidized particles. The blue to green color bar indicates the % content of the reduced particles. It is derived from LCA data fitting of all slices, considering the reference spectra presented in Fig. 6.6. The approximate region of each recorded position is illustrated here.

dataset of reference spectra (see Fig. 6.6), they provide a more detailed view of the distribution of Mo species along the reactor. However, they do not indicate the level of quantifiability in the results.

6.5 Conclusion

This research presented the combination of the operando XAS with microtomography as a powerful characterization tool for simultaneously spatially- and energy-resolved 3D imaging at beamline P64, PETRA III. By utilizing the aRCTIC sample environment in this technique, the 3D imaging of the chemical state of Mo supported on Al_2O_3 species was performed during the ODH of ethane to ethylene. This reaction system exhibits ideal properties for investigating development methods, such as the convenient manipulation of gas phase species, rapid catalyst synthesis, sustained catalyst performance within a short time frame, and long-term stability of the catalyst. To tune the photon transmission through the reactor, 20 wt% Mo on Al_2O_3 was placed inside the reactor with an outer diameter of 1 mm.

This chemical reaction was studied under three chemical conditions (ex-situ, oxidized, and operando). In the oxidized condition, the sample was heated to a temperature of 490 °C, utilizing two freely positionable hot air blowers and under operando condition, the temperature of the sample was around 490 °C. The GC was utilized for real-time monitoring of the catalyst's catalytic activity during the imaging process.

By utilizing the high-resolution X-ray camera with data acquisition of 20 Hz, a full 3D XANES dataset was captured at 105 distinct energies around the Mo K absorption edge in approximately 3.5 h. According to the LCA data fitting of the reconstructed tomogram under ex-situ and oxidized conditions, the oxidized molybdenum catalyst was filled inside the catalyst bed due to the presence of the full amount of oxygen. Under operando conditions, through the oxygen conversion in the direction of the gas flow, a color gradient was observed along the axial position of the catalyst bed in which the catalyst appeared gray at the inlet of the catalyst bed and was followed by a black region at the outlet. In fact, this operando XANES tomography facilitated the detection of local structural gradients at a micrometer spatial resolution, ranging from oxidized Mo at the beginning to reduced Mo at the end of the microreactor during this chemical reaction. These results are consistent with previous measurements of ODH of ethane over a Mo catalyst [84, 85, 90].

Additionally, it's essential to emphasize that conventional X-ray tomography measurements in the past were limited to the ex-situ condition or at a single energy, are incapable of generating the results demonstrated here. Also, a rapid spatial and energy-resolved tomography under working conditions is necessary for the representation of the reaction progress or reaction steps in a complex sequence of events. In this way, this operando XANES tomography method integrates all these aspects and provides a technique for verifying the presence of a reaction, investigating the catalyst's chemical state, and identifying chemical gradients as a function of the position of the catalyst bed simultaneously under operando conditions.

7 Conclusions & outlook

This research was focused on X-ray absorption near edge structure (XANES) microscopy and the measurement concepts for learning about the chemical composition of materials, especially heterogeneous catalysis under in-situ/operando conditions. This was accomplished first in 2D and then in 3D with spatial-, temporal-, and energy resolution.

In the first measurement (see Chapter 5), a rapid full-field 2D-XANES imaging was implemented at the beamline P64 at PETRA III by using the quick-extended X-ray absorption fine structure (QEXAFS) monochromator in combination with a high-resolution X-ray detector. This method was validated by studying the known chemical reaction of catalytic partial oxidation of methane to syngas over Pt catalyst. With this technique, full XANES movies were recorded with a time resolution of 2.8 s. During the ignition, a distinct gradient between partially and fully reduced Pt particles appeared, which moved rapidly from the outlet to the inlet of the catalyst bed on a second timescale.

Since the X-ray detector has a low photon sensitivity, images were binned by a factor of 16 which limited the spatial resolution to slightly better than 20 µm. The primary issue with this experiment was the necessity to alter the experimental chemical conditions to obtain images.

The previous methodology was then extended into XANES full-field tomography imaging (see Chapter 6) for the subsequent experiment. For this purpose, the Rotating Capillary for Tomographic In situ/ Operando Catalysis, short aRCTIC, setup for rotating the reactor was utilized. During the rotation of the capillary containing the catalytic material over 180° and the recording of flat field images of the reactor, the distribution of heat was uniform throughout the sample. Additionally, by upgrading the scintillator of the detector for this measurement, images were binned only by a factor of 4, and the spatial resolution was limited to 5 µm. Consequently, the accuracy of the measurement was substantially improved.

The double-crystal fixed-exit monochromator (DCM) was used in this measurement and the energy scan was run as the outer scan loop. In this way, the X-ray energy was adjusted to distinct values around the absorption edge of the catalyst. In order to test this developed technique, the oxidative dehydrogenation of ethane to ethylene over Mo catalyst was chosen and a full 3D XANES dataset containing the 105 energy points around the Mo K-edge was recorded in about 3.5 h.

Under operando conditions, through the conversion of oxygen, a chemical gradient was observed along the axial position of the catalyst bed in the flow direction. As a result, the catalyst bed was divided into different zones and full 3D XANES tomograms were recorded in multiple regions along the catalytic reactor bed. X-ray absorption spectroscopy (XAS) spectra obtained from the reconstructed and sorted data demonstrated the presence of different oxidation states of the molybdenum catalyst.

At the beginning of the catalyst bed, the partial oxidized Mo was observed in the presence of oxygen. During the rapid decline of oxygen partial pressure along the catalyst bed, oxygen vacancies in the catalyst structure cannot be refilled. In this way, the XAS spectra indicated the phase transformation from the oxidized form at the beginning to the reduced form at the end of the catalyst bed [79,85]. Additionally, the linear combination analysis of the spectra near the ignition point, where the full gas phase oxygen was converted, indicated that the recorded spectra at this region were a mixture of the oxidized and reduced Mo spectra.

Overall, these methodologies enable us to do 2D and 3D XANES imaging with spatial-, energy- and time resolution under operando conditions. Unlike prior studies that focused on rapid imaging at a single energy or relatively slow imaging at multiple energies across the XANES region, these approach combine all of them [12]. These approaches are flexible and are applicable to alternative XAS or QEXAFS beamlines, along with an appropriate sample environment for gas-phase analytics, facilitating concurrent catalytic studies [12].

In this research, full-field 3D XANES tomography was studied using a DCM. It is possible to repeat this measurement with a QEXAFS monochromator in order to speed up the recording time of the full 3D XANES dataset [12]. Modern QEXAFS technology enables quicker scanning of X-ray energy on the millisecond time scale and even below. Due to this, if the signal levels are sufficient and faster 2D X-ray cameras are utilized, time resolution in 2D and 3D XANES imaging measurements can be enhanced [12].

Another direction to improve the quality of these kinds of measurements involves the utilization of pixel detectors. These detectors have considerably higher photon-counting capabilities and when combined with magnified imaging, they can increase the spatial and temporal resolutions to micrometer and millisecond scales [12].

As XANES tomography produces a large volume of data records, data analysis is very time-consuming. Automated data analysis with machine learning (ML) can quickly analyze large volumes of datasets and reduce the analysis time by parallelized data processing [91]. ML provides real-time analysis of XANES data and extracts valuable information regarding the oxidation state of the catalytic material during measurement, which facilitates quality control and prompt decision-making during measurement. Consequently, it would be of great benefit to incorporate all the above-mentioned upgrades, especially automated data analysis with ML into the 2D and 3D XANES imaging to enhance the performance and accuracy.

It is important to note that the reactions and catalysts employed in this study were only test systems. However, these methods can be applied to a range of systems, including heterogeneously catalyzed and industrially relevant reaction systems under operating conditions, which can be conducted within a capillary at such length scales. Studying the reaction mechanisms within a laboratory frame enhances comprehension of process kinetics and facilitates the optimization of chemical reactions, thereby minimizing risks. Since kinetics is an intrinsic phenomenon, understanding it enables successful scaling up of processes to larger reactors. In this way, we can play a role in contributing to the development of a more efficient chemical industry.

The significant advantage of operando measurements is their capability to investigate structure/activity relationships. This holds great importance in catalysis as these are functional materials and the structure and function are closely related. Hence, these measurements enabling the investigation of the relationship between a material's structure and its activity are highly valuable.

The full-field imaging technique is applicable to large systems, covering millimeter-length scales. This method facilitates the study of larger objects than simple model systems. Especially, employing full-field tomography to examine the structure of large objects with relatively high resolution provides valuable insights into their structural characteristics over large length scales. Another significant advancement of this method is the speed of the measurement. We can study processes that occur rapidly, such as responses to different gas environments. This kind of measurement enables the study of kinetics, obtaining both structural and activity data concurrently.

Overall, full-field imaging enables examination beyond model samples and provides the potential for high time resolution (under appropriate conditions). These capabilities are particularly pertinent for larger-scale reactors or technical systems.

Appendix

List of beamtimes

Experimental data collected at PETRA III from 2018 and archived on the central ASAP3 storage system by DESY IT. Beamtimes are identified with an eight- digit beamtime ID and have a responsible principal investigator (PI). Following is information regarding the beamtimes ID and the co-proposers for each measurement conducted during my Ph.D.:

Beamtime ID 11005251

- PI: Alizadehfanaloo
- Beamline: P64
- Co-proposers: Alizadehfanaloo (DESY), Dr. Garrevoet (DESY), Dr. Murzin (DESY), Dr. Becher (KIT), Dr. Doronkin (KIT), Dr. Sheppard (KIT), Dr. Schropp (DESY), Prof. Dr. Grunwaldt (KIT), Prof. Dr. Schroer (DESY, UHH).

Beamtime ID 11007035

- PI: Dr. Wollak
- Beamline: P64
- Co-proposers: Dr. Wollak (TUHH), Alizadehfanaloo (DESY), Dr. Sheppard (KIT), Prof. Dr. Grunwaldt (KIT), Prof. Dr. Schroer (DESY, UHH), Prof. Dr. Horn (TUHH).

Beamtime ID 11009452

- PI: Dr. Wollak
- Beamline: P65
- Co-proposers: Dr. Wollak (TUHH), Alizadehfanaloo (DESY), Dr. Sheppard (KIT), Dr. Doronkin (KIT), Prof. Dr. Grunwaldt (KIT), Prof. Dr. Horn

(TUHH).

Beamtime ID 11009453

- PI: Dr. Wollak
- Beamline: P64
- Co-proposers: Dr. Wollak (TUHH), Alizadehfanaloo (DESY), Dr. Sheppard (KIT), Dr. Doronkin (KIT), Prof. Dr. Grunwaldt (KIT), Prof. Dr. Horn (TUHH).

Beamtime ID 11009843

- PI: Alizadehfanaloo
- Beamline: P64
- Co-proposers: Alizadehfanaloo (DESY), Dr. Wollak (TUHH), Dr. Murzin (DESY), Das (KIT), Dr. Sheppard (KIT), Dr. Schropp (DESY), Prof. Dr. Horn (TUHH), Prof. Dr. Schroer (DESY, UHH).

The data for this thesis are derived from measurements that I conducted as the PI.

Bibliography

[1] C. Schroer, I. Agapov, R. Roehlsberger, R. Wanzenberg, R. Brinkmann *et al.*, "PETRA IV: upgrade of PETRA III to the Ultimate 3D X-ray microscope," *Conceptual Design Report (CDR). Hamburg: Deutsches Elektronen-Synchrotron DESY*, 2019.

[2] J.-D. Grunwaldt, J. B. Wagner, and R. E. Dunin-Borkowski, "Imaging catalysts at work: a hierarchical approach from the macro-to the meso-and nano-scale," *ChemCatChem*, vol. 5, no. 1, pp. 62–80, 2013.

[3] S. R. Bare and T. Ressler, "Characterization of catalysts in reactive atmospheres by x-ray absorption spectroscopy," *Advances in catalysis*, vol. 52, pp. 339–465, 2009.

[4] M. A. Bañares, "Operando methodology: combination of in situ spectroscopy and simultaneous activity measurements under catalytic reaction conditions," *Catalysis today*, vol. 100, no. 1-2, pp. 71–77, 2005.

[5] S. Hannemann, J.-D. Grunwaldt, N. van Vegten, A. Baiker, P. Boye *et al.*, "Distinct spatial changes of the catalyst structure inside a fixed-bed microreactor during the partial oxidation of methane over Rh/Al2O3," *Catalysis Today*, vol. 126, no. 1-2, pp. 54–63, 2007.

[6] O. Korup, S. Mavlyankariev, M. Geske, C. F. Goldsmith, and R. Horn, "Measurement and analysis of spatial reactor profiles in high temperature catalysis research," *Chemical Engineering and Processing: Process Intensification*, vol. 50, no. 10, pp. 998–1009, 2011.

[7] J. Becher, D. F. Sanchez, D. E. Doronkin, D. Zengel, D. M. Meira *et al.*, "Chemical gradients in automotive Cu-SSZ-13 catalysts for NOx removal revealed by operando x-ray spectrotomography," *Nature Catalysis*, vol. 4, no. 1, pp. 46–53, 2021.

[8] J.-D. Grunwaldt and C. G. Schroer, "Hard and soft x-ray microscopy and tomography in catalysis: bridging the different time and length scales," *Chemical*

Society Reviews, vol. 39, no. 12, pp. 4741–4753, 2010.

[9] J.-D. Grunwaldt and A. Baiker, “In situ spectroscopic investigation of heterogeneous catalysts and reaction media at high pressure,” *Physical Chemistry Chemical Physics*, vol. 7, no. 20, pp. 3526–3539, 2005.

[10] J.-D. Grunwaldt, B. Kimmerle, A. Baiker, P. Boye, C. G. Schroer *et al.*, “Catalysts at work: From integral to spatially resolved X-ray absorption spectroscopy,” *Catalysis Today*, vol. 145, no. 3-4, pp. 267–278, 2009.

[11] J. A. Van Bokhoven and C. Lamberti, *X-ray absorption and X-ray emission spectroscopy: theory and applications.* John Wiley & Sons, 2016, vol. 1.

[12] S. Alizadehfanaloo, J. Garrevoet, M. Seyrich, V. Murzin, J. Becher *et al.*, “Tracking dynamic structural changes in catalysis by rapid 2D-XANES microscopy,” *Journal of synchrotron radiation*, vol. 28, no. 5, pp. 1518–1527, 2021.

[13] J. Becher, S. Weber, D. Ferreira Sanchez, D. E. Doronkin, J. Garrevoet *et al.*, “Sample Environment for Operando Hard X-ray Tomography—An Enabling Technology for Multimodal Characterization in Heterogeneous Catalysis,” *Catalysts*, vol. 11, no. 4, p. 459, 2021.

[14] A. Schropp, “Experimental coherent x-ray diffractive imaging: Capabilities and limitations of the technique,” 2008.

[15] R. Hölzle, *Streumethoden zur Untersuchung kondensierter Materie: Vorlesungsmaunskripte des 27. IFF-Ferienkurses vom 4. bis 15. März 1996 im Forschungszentrum Jülich.* Publikationen vor 2000, 1996, no. FZJ-2021-01807.

[16] J. A. Clarke, *The science and technology of undulators and wigglers.* OUP Oxford, 2004, vol. 4.

[17] J. Als-Nielsen and D. McMorrow, *Elements of modern X-ray physics.* John Wiley & Sons, 2011.

[18] J. J. Sakurai and J. Napolitano, *Modern quantum mechanics.* Cambridge University Press, 2020.

[19] C. MacDonald, “An introduction to x-ray physics, optics, and applications,” in *An Introduction to X-Ray Physics, Optics, and Applications.* Princeton University Press, 2017.

[20] C. Jacobsen, *X-ray Microscopy.* Cambridge University Press, 2019.

[21] S. Raman, D. Paul, J. Hammond, and K. Bomben, “Auger electron spectroscopy

and its application to nanotechnology," *Microscopy today*, vol. 19, no. 2, pp. 12–15, 2011.

[22] L. Baumgarten, "X-ray absorption spectroscopy," *Scattering Methods for Condensed Matter Research: Towards Novel Applications at Future Sources. Forschungszentrum Jülich GmbH, JCNS, PGI, ICS, IAS Jülich*, 2012.

[23] J. J. Sakurai and E. D. Commins, "Modern quantum mechanics, revised edition," 1995.

[24] J. Kowalska and S. DeBeer, "The role of x-ray spectroscopy in understanding the geometric and electronic structure of nitrogenase," *Biochimica et Biophysica Acta (BBA)-Molecular Cell Research*, vol. 1853, no. 6, pp. 1406–1415, 2015.

[25] S. Calvin, *XAFS for Everyone.* CRC press, 2013.

[26] D. C. Koningsberger and R. Prins, "X-ray absorption: principles, applications, techniques of EXAFS, SEXAFS and XANES," 1987.

[27] T. A. Dessie, W.-H. Huang, D. B. Adam, Y. A. Awoke, C.-H. Wang *et al.*, "Efficient H2 Evolution Coupled with Anodic Oxidation of Iodide over Defective Carbon-Supported Single-Atom Mo-N4 Electrocatalyst," *Nano Letters*, vol. 22, no. 18, pp. 7311–7317, 2022.

[28] F. Hippert, E. Geissler, J. L. Hodeau, E. Lelièvre-Berna, and J.-R. Regnard, *Neutron and X-ray Spectroscopy.* Springer Science & Business Media, 2006.

[29] M. Newville, "Fundamentals of xafs, consortium for advanced radiation sources," *University of Chicago, Chicago, IL*, 2004.

[30] B. Ravel and M. Newville, "ATHENA, ARTEMIS, HEPHAESTUS: data analysis for X-ray absorption spectroscopy using IFEFFIT," *Journal of synchrotron radiation*, vol. 12, no. 4, pp. 537–541, 2005.

[31] C. Schroer, J. Meyer, M. Kuhlmann, B. Benner, T. Günzler *et al.*, "Nanotomography based on hard x-ray microscopy with refractive lenses," *Applied Physics Letters*, vol. 81, no. 8, pp. 1527–1529, 2002.

[32] C. G. Schroer, P. Boye, J. M. Feldkamp, J. Patommel, A. Schropp *et al.*, "Coherent x-ray diffraction imaging with nanofocused illumination," *Physical review letters*, vol. 101, no. 9, p. 090801, 2008.

[33] F. Wittwer, J. Hagemann, D. Brückner, S. Flenner, and C. G. Schroer, "Phase retrieval framework for direct reconstruction of the projected refractive index

applied to ptychography and holography," *Optica*, vol. 9, no. 3, pp. 295–302, 2022.

[34] A. C. Kak and M. Slaney, *Principles of computerized tomographic imaging.* SIAM, 2001.

[35] C. E. Shannon, "A mathematical theory of communication," *The Bell system technical journal*, vol. 27, no. 3, pp. 379–423, 1948.

[36] P. Gilbert, "Iterative methods for the three-dimensional reconstruction of an object from projections," *Journal of theoretical biology*, vol. 36, no. 1, pp. 105–117, 1972.

[37] W. Schwieger, A. G. Machoke, T. Weissenberger, A. Inayat, T. Selvam *et al.*, "Hierarchy concepts: classification and preparation strategies for zeolite containing materials with hierarchical porosity," *Chemical society reviews*, vol. 45, no. 12, pp. 3353–3376, 2016.

[38] S. R. Bare, S. D. Kelly, B. Ravel, N. Greenlay, L. King *et al.*, "Characterizing industrial catalysts using in situ XAFS under identical conditions," *Physical Chemistry Chemical Physics*, vol. 12, no. 27, pp. 7702–7711, 2010.

[39] C. G. Schroer, M. Kuhlmann, T. F. Günzler, B. Lengeler, M. Richwin *et al.*, "Mapping the chemical states of an element inside a sample using tomographic x-ray absorption spectroscopy," *Applied physics letters*, vol. 82, no. 19, pp. 3360–3362, 2003.

[40] W. A. Caliebe, V. Murzin, A. Kalinko, and M. Görlitz, "High-flux XAFS-beamline P64 at PETRA III," in *AIP conference proceedings*, vol. 2054, no. 1. AIP Publishing LLC, 2019, p. 060031.

[41] E. Lohrmann and P. Soeding, "About fast particles and bright light. 50 years deutsches electronen-synchrotron desy; von schnellen teilchen und hellem licht. 50 jahre deutsches elektronen-synchrotron desy," 2009.

[42] E. Weckert, "The potential of future light sources to explore the structure and function of matter," *IUCrJ*, vol. 2, no. 2, pp. 230–245, 2015.

[43] I. Agapov, S. Antipov, R. Bartolini, R. Brinkmann, Y. Chae *et al.*, "PETRA IV storage ring design," *Proc. IPAC*, vol. 22, pp. 1431–1434, 2022.

[44] C. G. Schroer, I. Agapov, W. Brefeld, R. Brinkmann, Y.-C. Chae *et al.*, "PETRA IV: the ultralow-emittance source project at DESY," *Journal of synchrotron radiation*, vol. 25, no. 5, pp. 1277–1290, 2018.

[45] Https://photon-science.desy.de/facilities/petra_iii/beamlines/p64_advanced_xafs/index_eng.html.

[46] B. Bornmann, J. Kläs, O. Müller, D. Lützenkirchen-Hecht, and R. Frahm, "The quick EXAFS setup at beamline P64 at PETRA III for up to 200 spectra per second," in *AIP Conference Proceedings*, vol. 2054, no. 1. AIP Publishing LLC, 2019, p. 040008.

[47] P. Kristiansen, J. Horbach, R. Döhrmann, and J. Heuer, "Vibration measurements of high-heat-load monochromators for DESY PETRA III extension," *Journal of synchrotron radiation*, vol. 22, no. 4, pp. 879–885, 2015.

[48] H. Schulte-Schrepping, M. Degenhardt, H. Peters, U. Hahn, J. Heuer *et al.*, "Status of PETRA III photon beamline frontends and optical systems," in *Journal of Physics: Conference Series*, vol. 425, no. 4. IOP Publishing, 2013, p. 042005.

[49] O. Müller, D. Lützenkirchen-Hecht, and R. Frahm, "Quick scanning monochromator for millisecond in situ and in operando x-ray absorption spectroscopy," *Review of Scientific Instruments*, vol. 86, no. 9, p. 093905, 2015.

[50] O. Müller, M. Nachtegaal, J. Just, D. Lützenkirchen-Hecht, and R. Frahm, "Quick-EXAFS setup at the SuperXAS beamline for in situ X-ray absorption spectroscopy with 10 ms time resolution," *Journal of synchrotron radiation*, vol. 23, no. 1, pp. 260–266, 2016.

[51] O. Müller, "Hard X-ray Synchrotron Beamline Instrumentation for Millisecond Quick Extended X-ray Absorption Spectroscopy," Ph.D. dissertation, Dissertation, Wuppertal, Universität Wuppertal, 2016, 2016.

[52] J. Becher, "Advancing Spatial Resolved X-ray Based Techniques in Catalysis," Ph.D. dissertation, Karlsruher Institut für Technologie (KIT), 2020.

[53] A. De Juan, J. Jaumot, and R. Tauler, "Multivariate Curve Resolution (MCR). Solving the mixture analysis problem," *Analytical Methods*, vol. 6, no. 14, pp. 4964–4976, 2014.

[54] E. Borodina, F. Meirer, I. Lezcano-González, M. Mokhtar, A. Asiri *et al.*, "Influence of the reaction temperature on the nature of the active and deactivating species during methanol to olefins conversion over H-SSZ-13," *ACS catalysis*, vol. 5, no. 2, pp. 992–1003, 2015.

[55] J. Timoshenko, A. Shivhare, R. W. Scott, D. Lu, and A. I. Frenkel, "Solving local structure around dopants in metal nanoparticles with ab initio modeling

of x-ray absorption near edge structure," *Physical Chemistry Chemical Physics*, vol. 18, no. 29, pp. 19 621–19 630, 2016.

[56] G. Qian, J. Zhang, S.-Q. Chu, J. Li, K. Zhang *et al.*, "Understanding the mesoscale degradation in nickel-rich cathode materials through machine-learning-revealed strain–redox decoupling," *ACS Energy Letters*, vol. 6, no. 2, pp. 687–693, 2021.

[57] Y. Zhou, D. E. Doronkin, M. Chen, S. Wei, and J.-D. Grunwaldt, "Interplay of Pt and crystal facets of TiO2: CO oxidation activity and operando XAS/DRIFTS studies," *ACS Catalysis*, vol. 6, no. 11, pp. 7799–7809, 2016.

[58] https://tomopy.readthedocs.io/_/downloads/en/1.6.0/pdf/.

[59] D. Gürsoy, Y. P. Hong, K. He, K. Hujsak, S. Yoo *et al.*, "Rapid alignment of nanotomography data using joint iterative reconstruction and reprojection," *Scientific reports*, vol. 7, no. 1, p. 11818, 2017.

[60] W. Van Aarle, W. J. Palenstijn, J. Cant, E. Janssens, F. Bleichrodt *et al.*, "Fast and flexible X-ray tomography using the ASTRA toolbox," *Optics express*, vol. 24, no. 22, pp. 25 129–25 147, 2016.

[61] W. Van Aarle, W. J. Palenstijn, J. De Beenhouwer, T. Altantzis, S. Bals *et al.*, "The ASTRA Toolbox: A platform for advanced algorithm development in electron tomography," *Ultramicroscopy*, vol. 157, pp. 35–47, 2015.

[62] T. F. Scientific, "User's guide avizo software 2019," *Konrad-Zuse-Zentrum fur Informationstechnik: Berlin (ZIB), Germany*, 2019.

[63] R. M. Navarro, M. Pena, and J. Fierro, "Hydrogen production reactions from carbon feedstocks: fossil fuels and biomass," *Chemical reviews*, vol. 107, no. 10, pp. 3952–3991, 2007.

[64] B. C. Enger, R. Lødeng, and A. Holmen, "A review of catalytic partial oxidation of methane to synthesis gas with emphasis on reaction mechanisms over transition metal catalysts," *Applied Catalysis A: General*, vol. 346, no. 1-2, pp. 1–27, 2008.

[65] J.-D. Grunwaldt, S. Hannemann, C. G. Schroer, and A. Baiker, "2D-mapping of the catalyst structure inside a catalytic microreactor at work: Partial oxidation of methane over Rh/Al2O3," *The Journal of Physical Chemistry B*, vol. 110, no. 17, pp. 8674–8680, 2006.

[66] B. Kimmerle, J.-D. Grunwaldt, A. Baiker, P. Glatzel, P. Boye *et al.*, "Visualizing a catalyst at work during the ignition of the catalytic partial oxidation of

methane," *The Journal of Physical Chemistry C*, vol. 113, no. 8, pp. 3037–3040, 2009.

[67] J. Stotzel, R. Frahm, B. Kimmerle, M. Nachtegaal, and J.-D. Grunwaldt, "Oscillatory behavior during the catalytic partial oxidation of methane: following dynamic structural changes of palladium using the QEXAFS technique," *The Journal of Physical Chemistry C*, vol. 116, no. 1, pp. 599–609, 2012.

[68] S. Bharadwaj and L. D. Schmidt, "Catalytic partial oxidation of natural gas to syngas," *Fuel processing technology*, vol. 42, no. 2-3, pp. 109–127, 1995.

[69] A. P. York, T. Xiao, and M. L. Green, "Brief overview of the partial oxidation of methane to synthesis gas," *Topics in Catalysis*, vol. 22, pp. 345–358, 2003.

[70] D. E. Doronkin, A. B. Kuriganova, I. N. Leontyev, S. Baier, H. Lichtenberg *et al.*, "Electrochemically synthesized Pt/Al2O3 oxidation catalysts," *Catalysis Letters*, vol. 146, pp. 452–463, 2016.

[71] E. Becker, P.-A. Carlsson, H. Grönbeck, and M. Skoglundh, "Methane oxidation over alumina supported platinum investigated by time-resolved in situ XANES spectroscopy," *Journal of Catalysis*, vol. 252, no. 1, pp. 11–17, 2007.

[72] N. Banterle, K. H. Bui, E. A. Lemke, and M. Beck, "Fourier ring correlation as a resolution criterion for super-resolution microscopy," *Journal of structural biology*, vol. 183, no. 3, pp. 363–367, 2013.

[73] M. Van Heel and M. Schatz, "Fourier shell correlation threshold criteria," *Journal of structural biology*, vol. 151, no. 3, pp. 250–262, 2005.

[74] F. M. de Groot, E. de Smit, M. M. van Schooneveld, L. R. Aramburo, and B. M. Weckhuysen, "In-situ scanning transmission X-ray microscopy of catalytic solids and related nanomaterials," *ChemPhysChem*, vol. 11, no. 5, pp. 951–962, 2010.

[75] I. D. Gonzalez-Jimenez, K. Cats, T. Davidian, M. Ruitenbeek, F. Meirer *et al.*, "Hard X-ray Nanotomography of Catalytic Solids at Work," *Angewandte Chemie*, vol. 124, no. 48, pp. 12 152–12 156, 2012.

[76] C. A. Gärtner, A. C. van Veen, and J. A. Lercher, "Oxidative dehydrogenation of ethane: common principles and mechanistic aspects," *ChemCatChem*, vol. 5, no. 11, pp. 3196–3217, 2013.

[77] I. Amghizar, J. N. Dedeyne, D. J. Brown, G. B. Marin, and K. M. Van Geem, "Sustainable innovations in steam cracking: CO 2 neutral olefin production," *Reaction Chemistry & Engineering*, vol. 5, no. 2, pp. 239–257, 2020.

[78] T. Ren, M. Patel, and K. Blok, “Olefins from conventional and heavy feedstocks: Energy use in steam cracking and alternative processes,” *Energy*, vol. 31, no. 4, pp. 425–451, 2006.

[79] B. Wollak, “Operando structure-activity profiling in fixed-bed reactors using synchrotron-based X-Ray techniques,” Ph.D. dissertation, Technische Universität Hamburg, 2023.

[80] D. Espinoza, B. Wollak, T. L. Sheppard, A.-C. Dippel, M. Sturm *et al.*, “Catalytic profile reactor for multimodal operando measurements during periodic operation,” *ChemCatChem*, vol. 14, no. 24, p. e202200337, 2022.

[81] E. Lox, “BH Engler in G. Ertl, H. Knözinger, J. Weitkamp (eds.): Handbook of heterogeneous catalysis, vol. 4,” 1997.

[82] G. Ertl, H. Knözinger, J. Weitkamp *et al.*, *Handbook of heterogeneous catalysis*. VCH Weinheim, 1997, vol. 2.

[83] P. Kube, B. Frank, S. Wrabetz, J. Kröhnert, M. Hävecker *et al.*, “Functional analysis of catalysts for lower alkane oxidation,” *ChemCatChem*, vol. 9, no. 4, pp. 573–585, 2017.

[84] M. Geske, O. Korup, and R. Horn, “Resolving kinetics and dynamics of a catalytic reaction inside a fixed bed reactor by combined kinetic and spectroscopic profiling,” *Catalysis Science & Technology*, vol. 3, no. 1, pp. 169–175, 2013.

[85] B. Wollak, D. Doronkin, D. Espinoza, T. Sheppard, O. Korup *et al.*, “Exploring catalyst dynamics in a fixed bed reactor by correlative operando spatially-resolved structure-activity profiling,” *Journal of Catalysis*, vol. 408, pp. 372–387, 2022.

[86] L. Seguin, M. Figlarz, R. Cavagnat, and J.-C. Lassègues, “Infrared and raman spectra of MoO3 molybdenum trioxides and MoO3· xH2O molybdenum trioxide hydrates,” *Spectrochimica Acta Part A: Molecular and Biomolecular Spectroscopy*, vol. 51, no. 8, pp. 1323–1344, 1995.

[87] E. Gulbransen, K. Andrew, and F. Brassart, “Oxidation of molybdenum 550 to 1700 C,” *Journal of the Electrochemical Society*, vol. 110, no. 9, p. 952, 1963.

[88] P. L. Gai, E. D. Boyes, S. Helveg, P. L. Hansen, S. Giorgio *et al.*, “Atomic-resolution environmental transmission electron microscopy for probing gas–solid reactions in heterogeneous catalysis,” *MRS bulletin*, vol. 32, no. 12, pp. 1044–1050, 2007.

[89] V. R. Porter, W. B. White, and R. Roy, “Optical spectra of the intermediate oxides of titanium, vanadium, molybdenum, and tungsten,” *Journal of Solid State Chemistry*, vol. 4, no. 2, pp. 250–254, 1972.

[90] B. Wollak, D. Espinoza, A.-C. Dippel, M. Sturm, F. Vrljic *et al.*, “Catalytic reactor for operando spatially resolved structure–activity profiling using high-energy x-ray diffraction,” *Journal of synchrotron radiation*, vol. 30, no. 3, 2023.

[91] J. Timoshenko and A. I. Frenkel, ““inverting” x-ray absorption spectra of catalysts by machine learning in search for activity descriptors,” *Acs Catalysis*, vol. 9, no. 11, pp. 10 192–10 211, 2019.

List of Publications

Wollak, B., Doronkin, D., Espinoza, D., Sheppard, T., Korup, O., Schmidt, M., Alizadefanaloo, S., Rosowski, F., Schroer, C-G., Grunwaldt, J.-D., and Horn, R. " Exploring catalyst dynamics in a fixed bed reactor by correlative operando spatially-resolved structure-activity profiling". In: Journal of Catalyst, 408 (2022), 372-387. Doi: 10.1016/j.jcat.2021.08.029.

Alizadehfanaloo, S., Garrevoet, J., Seyrich, M., Murzin, V., Becher, J., Doronkin, D., Sheppard, T.-L., Grunwaldt, J.-D., Schroer, C.-G., and Schropp, A. "Tracking dynamic structural changes in catalysis by rapid 2D-XANES microscopy". In: Journal of Synchrotron Radiation, 28 (2021), 1518-1527. Doi: 10.1107/S1600577521007074.

In Preparation:

Alizadehfanaloo, S., Wollak, B., Das, S., Murzin, V., Sheppard, T.-L., Schroer, C.-G., and Schropp, A."Operando XAS Tomography for rapid 3D characterization of Mo-catalysts for oxidative dehydrogenation of ethane".

Acknowledgements

First of all, I would like to thank my supervisor Prof. Dr. Christian G. Schroer for giving me the opportunity to pursue my Ph.D. in the FS-PETRA group at DESY. The scope of this thesis, he assisted me in finding new approaches to overcome difficulties, and I would not have been able to complete this thesis without his support and advice. Additionally, his unfailingly friendly and approachable disposition, combined with his mentorship and encouragement, has significantly influenced my intellectual and personal growth.

This project would not have been possible without the assistance of numerous people and working groups. Therefore, I would like to express my sincere appreciation.

I am very grateful to my co-supervisor Dr. Andreas Schropp for the cooperation during these years. He was very helpful in planning, applying for, and executing the experiments, as well as in many other aspects of the project. Throughout our work together, he has always provided support in defining the direction of this work, as well as many clarifying discussions about the results and advice. In our discussions, I gained insight into the X-ray imaging techniques from his intuition.

Furthermore, I would like to express my gratitude to Dr. Thomas Sheppard, who assisted me with advice and many clarifying discussions in this study with many clarifying discussions and advice, especially in the chemistry field. He always provided the best ideas for the visualization and the analysis of data. Sincerely, this research would not have been possible without the use of his sample environment and his support.

I would also like to thank the committee members Prof. Dr. Daniela Pfannkuche, Prof. Dr. Dorota Koziej, Dr. Thomas Sheppard, and Dr. Thomas Keller for agreeing to form my examination committee.

Special thanks go to Dr. Martin Seyrich for his patience in answering my questions about data analysis in the early stages of my project and proofreading my thesis. He always provided great support for me and shared his knowledge about programming.

I would like to thank Samaneh Ehteram and Johannes Dora for having a great time and for the opportunity to discuss various aspects of research in our office.

I would like to thank Dr. Dmitry Doronkin from KIT for the catalyst synthesis in the first measurement. He provided me great support in answering my chemistry questions. I extend my gratitude to Dr. Johannes Becher from KIT for the excellent support provided during the initial measurement, and I express my appreciation to Ms. Srashtasrita Das from KIT for her valuable support during the second measurement.

I would like to thank Prof. Dr. Horn from TUHH for his cooperation during this research. He supported me by providing the equipment's of his laboratory during my beamtimes. It was a pleasure collaborating with Dr. Birte Wollak from TUHH during beamtimes at PETRA III. Especially, she played a key role in designing the chemical reaction procedure for the second experiment. I express my gratitude to Ms. Laarmann, a chemical-technical assistant at TUHH, for catalyst synthesis in the second measurement.

In particular, I would like to take this opportunity to thank the engineering team, Ralph Döhrmann, Stephan Botta, and Patrik Wiljes for developing parts of the microscopy setup and providing support during the beamtimes at PETRA III.

I want to express my gratitude to the beamline scientists Dr. Wolfgang Caliebe, Dr. Jan Garrevoet, and Dr. Vadim Murzin. Their invaluable support during the beamtimes at P64 was crucial, and without their assistance, this research would not have been possible.

Additionally, I would like to express my gratitude to my colleagues for their always helpful and approachable nature especially Thea Engler. I appreciated the opportunity to work with all the members of the group, both past and present, who were responsible for a pleasant working environment.

Many thanks to my husband Dr. Milad Behrooz for his patience, his support and many discussions regarding the data analysis. I am very grateful for my daughter Niki's patience, support, and for staying in the kindergarten for long hours while this thesis was being written. Without their tremendous understanding and encouragement in past few years, it would have been impossible for me to complete my doctoral work.

Additionally, I would also like to thank my family for their inexhaustible trust and mental support during the whole of my life.

Last but not least, I would like to thank all those who have contributed to this work in some way and who unfortunately went unnoticed here.

Eidesstattliche Versicherung

Hiermit versichere ich an Eides statt, die vorliegende Dissertationsschrift selbst verfasst und keine anderen als die angegebenen Hilfsmittel und Quellen benutzt zu haben.

Alizadehfanaloo

Hamburg, 20.03.2024

Saba Alizadehfanaloo